The University of Manitoba

Deformation Mechanisms in the Single and Two Phase Structures of Iron

by

David Tseng

A Dissertation

Submitted to the Faculty of Graduate Studies

In Partial Fulfillment of the Requirement

For the Degree of

Doctor of Philosophy

Department of Mechanical Engineering

Winnipeg, Manitoba

March 1982

DEFORMATION MECHANISMS IN THE SINGLE AND TWO PHASE STRUCTURES OF IRON

BY

DAVID TSENG

A thesis submitted to the Faculty of Graduate Studies of the University of Manitoba in partial fulfillment of the requirements of the degree of

DOCTOR OF PHILOSOPHY

ABSTRACT

The deformation mechanisms in single phase and two-phase structures of iron are studied in this dissertation.

In single phase α-iron, there are two temperature regions (I and III) in which the flow stress is dependent on temperature and strain rate, i.e., the deformation is thermally activated. Region I and III are connected by an athermal region II. It has been shown that region III can extend into region II at large strains.

In region I, the flow stress is composed of a thermal component (or effective stress) and an athermal component (or internal stress). The effective stress is required to overcome the short-range obstacles with the assistance of thermal fluctuations in the crystal. It has become evident that the high Peierls stress (the short-range barriers in region I) arises from the three-fold symmetry of the screw dislocation core in b.c.c. metals. Before a screw dislocation can glide, its core must be transformed into glissile form. The characteristic flow behavior of high purity Battelle iron can only be explained in terms of the above model. The temperature sensitivity of the effective stress of Battelle iron consists of two approximately linear portions of different slopes connected by a transition region centered at 220 K. It has been observed that impurity atoms can interfere with the sessile-glissile transformation of screw dislocations and give rise to softening between 180 and 300 K and hardening at other temperatures. At 300 K and above, the Peierls barriers become transparent to screw dislocations because there are enough thermal fluctuations in the crystal to assist the

overcoming of these barriers. Therefore, in region II, the applied stress is equal to the internal stress in region I. It is proposed that the internal stress is mainly due to the formation of attractive junctions.

In region III, the flow stress becomes sensitive to temperature again. The high temperature flow of iron is characterized by a steady-state flow at large strains. It is assumed that the subboundary network controls the steady-state flow. The glide of dislocations in the subgrain produces the only significant strain. This leads to the strain rate being proportional to the fourth power of stress.

In part II, the back stress hardening of a dual-phase steel (DPS) has been investigated using the Bauschinger effect technique. The DPS was prepared by intercritically annealing a Nb - V HSLA steel. The strain partitioning between ferrite and martensite depends on the relative strength of the two phases. It has been verified by quantitative microscopy that the high carbon martensite islands at low volume fraction do not participate in deformation while the low carbon martensite at high volume fractions deforms as extensively as the ferrite grains. The permanent softening, commonly observed in particle hardened alloys, is not found in this DPS. The contribution to work hardening by kinematic hardening increases with increasing volume fraction of martensite.

ACKNOWLEDGMENTS

I am especially indebted to my academic advisor, Professor Kris Tangri, whose professional guidance and methodology in scientific research have played a major influence on my scholastic development.

I am grateful to Professor F. H. Vitovec for his hospitality during my stay at the University of Alberta (1979-1980). Part of the work reported here (Part II) was done at his laboratory.

I am particularly grateful to Dr. Roger Dutton, Head of Materials Science Branch, WNRE, for making critical comments on the thesis.

Lastly, I would also like to offer my deepest appreciation to my wife for her understanding and constant encouragement at times when I needed it most.

Table of Contents

page

ABSTRACT i

ACKNOWLEDGMENTS iii

LIST OF FIGURES vi

LIST OF SYMBOLS x

CHAPTER

1 INTRODUCTION 1

PART I THERMALLY ACTIVATED DEFORMATION OF B.C.C. IRON 7

2 LITERATURE REVIEW 8

2.1 Plastic Flow of B.C.C. Metals at Low temperatures 8

2.1.1 Slip System in B.C.C. Metals 9

2.1.2 The Rate-Controlling Short-Range Obstacles at Low Temperatures 14

2.1.3 The Solution Hardening Model 16

2.1.4 The Peierls Models 18

2.1.5 Solution Softening in Dilute Iron Base Alloys 23

2.2 Plastic Flow at Intermediate and High Temperatures 27

2.2.1 Intersection Mechanism 29

2.2.2 Diffusion Controlled Processes 31

2.3 Thermodynamics of Plastic Flow 36

3 EXPERIMENTAL PROCEDURES 41

3.1 Specimen Preparation 41

3.2 The Cryostat and High Temperature Apparatus 44
3.3 Testing Procedure 46
4 RESULTS AND DISCUSSIONS 48
4.1 Plastic Flow of α Iron Between 0-300K
(Region I) 48
4.1.1 Ferrovac E Iron 50
4.1.2 Comparison of Ferrovac E Experimental
Results with Theoretical Predictions 58
4.1.3 High Purity Battelle Iron 66
4.1.4 Intrinsic versus Extrinsic Mechanisms 73
4.2 Plastic Flow at Intermediate and High
Temperatures 86
4.2.1 Region III - The Thermally Activated
Flow of Ferrovac E Iron 88
4.2.2 Deformation Mechanism in Region III 100
4.3 Summary and Conclusions 108
PART II DEFORMATION OF TWO-PHASE SYSTEM 110
5 DUAL-PHASE STEEL 111
5.1 Experimental procedures 116
5.2 Results 117
5.3 Discussion 140
5.4 Summary and Conclusions 148
REFERENCES 150
APPENDIX 157

LIST OF FIGURES

Figure		page
1-1	Schematic diagram of the temperature dependence of flow stress in metals.	2
2-1	Hard sphere model of {110} and {112} planes in b.c.c. crystals. The dotted circles represent atoms on the top or bottom planes.	11
2-2	Fleischer's force-distance curve.	16
2-3	Dissociation into {110} and {112} planes.	19
2-4	Attractive junction reaction.	29
2-5	Force distance diagram.	37
3-1	Cryostat	45
3-2	Differential-temperature and strain rate cycling tests.	47
4-1	Optical micrographs. (a) recrystallized Ferrovac E Iron, (b) without pre-strain at room temperature, twinning is a competitive mode of deformation, (c) with 3.5 % pre-strain, elongated grains in the neck region after deformation at 10K.	51
4-2	($\Delta\tau^*/\Delta T$) determined from temperature change tests.	53
4-3	Variation of effective shear stress with temperature in Ferrovac E iron.	54
4-4	Comparison of experimental and theoretical $V^* - \tau^*$ curves.	56

4-5 Variation of activation enthalpy with temperature of Ferrovac E iron. 57

4-6 Comparison of τ^* - T curve of Ferrovac E iron with theoretical predictions. 62

4-7 Dislocation-solute interactions. 63

4-8 Temperature sensitivity of the effective stress for Battelle iron. 67

4-9 Effective stress as a function of temperature for Battelle iron. 69

4-10 Strain rate sensitivity of flow stress. 70

4-11 Activation volume as a function of effective stress. . . . 72

4-12 Effect of impurity on τ^* - T curve predicted by Wuthrich and Frank. 81

4-13 Activation enthalpies for Ferrovac E and Battelle iron 84

4-14 Yield stress of Ferrovac E iron in region II and III. . . 87

4-15 Yield and steady-state flow stresses at three different strain rates in region III. 89

4-16 Yield stress versus strain rate plots. 90

4-17 Steady-state flow stress versus strain rate plots. . . . 91

4-18 Activation volume versus stress plots in region III. . . 93

4-19 $\dot{\varepsilon}$ - T plot for constant yield stress. 95

4-20 $\dot{\varepsilon}$ - T plot for constant steady-state flow stress. . . . 96

4-21 Activation energies at constant yield and steady-state flow stresses. 97

4-22 μ - T plot after Denver[77]. 99

4-23 Attractive junction and unzipping of a junction. 103

4-24 Comparison of equation (6-21) with steady-state creep data for b.c.c. metals. 106

5-1 Phase diagram of iron-carbon system. 114

5-2 Two-phase microstructures resulting from intercritical anneal at various temperatures. 118

5-3 Hardness variation during isochronal anneal of dual-phase and fully martensitic steels. 119

5-4 (a) σ- ε curves, (b) $\log\sigma$ - $\log\dot{\varepsilon}$ plots. 122

5-5 Work hardening rate as a function of plastic strain. . .124

5-6 Normalized work hardening rate. 125

5-7 Flow stress versus volume fraction of martensite. 127

5-8 Stress-strain curves for tension-compression cycle. . . .129

5-9 The decay of the stress difference as a function of reverse strain. 130

5-10 ($\sigma_F - \sigma_R$) measured at $\varepsilon_R = 0.5\%$ as a function of ε_F . .132

5-11 Average Bauschinger strain as a function of forward strain. 133

5-12 Microhardness of martensite and ferrite versus annealing temperature. 135

5-13 The strains of ferrite and martensite in a fractured tensile specimen containing 43% martensite. 137

5-14 Fractographs for specimens with IAT = 760 and 865 C. . . .139

5-15 Kinematical $\sigma - \xi$ curves and ideal kinematical hardening curves. 141

5-16 Stress-strain curves and ideal kinematical hardening curves (KI). 142

5-17 Two-element Masing model. 146

LIST OF SYMBOLS

a	lattice paramater of b.c.c. iron
A	Zener factor
A_f	area swept after a successful event.
$\underline{b}$	Burgers vector.
C	elastic constant.
d	grain size.
D	diffusion coefficient.
E	dislocation self-energy per unit length.
$\underline{f}$	Burgers vector of a partial dislocation.
f_m	volume fraction of martensite
F	force on a dislocation.
k	Boltzmann's constant.
K	Kelvin temperature.
ℓ	dislocation length.
L	distance between neighboring impurity atoms.
L_s	subgrain size.
M	dislocation source density.
n	strain or stress exponent.
Q	activation energy. Subscript SD indicates self-diffusion energy.
T	temperature. Subscript c indicates critical or transition temperature and m indicates melting point.
V^*	activation volume.

w width of a subboundary wall.

α angle between a glide dislocation and the intersection line of two slip planes.

γ stacking fault energy.

δ angle between the Burgers vector and the tangent to a dislocation line.

ε strain

$\dot{\varepsilon}$ strain rate. Subscript s indicates steady-state strain rate.

σ axial stress.

τ shear stress, $\sigma = 2\tau$. Superscript * indicates effective stress. Subscript μ indicates internal stress.

ρ dislocation density.

μ shear modulus.

ν Poisson ratio or vibration frequency.

θ angle

Θ work-hardening rate.

ΔG gibbs free energy.

ΔH enthalpy

ΔS entropy

CHAPTER 1

INTRODUCTION AND OBJECTIVES

The plastic flow behavior of metallic crystals, in particular, the more common metals and their alloys, has been investigated quite extensively in the past. Many dislocation mechanisms have been proposed to explain the flow behavior of a given crystal system in different temperature ranges. However, if we compile and classify all the existing data according to crystal structures, we can find some similarities as well as dissimilarities. In the case of similarity in flow behavior in a given temperature regime, it is quite natural to speculate that a common deformation mechanism operates and a general theory or an equation of state can be established. This is particularly useful from the engineering point of view. The important similarities between f.c.c. and b.c.c. metals are : (1) there exists two prominent temperature regions (I and III in Fig. 1-1) wherein the flow stress is temperature and strain-rate sensitive, in other words, the deformation is thermally activated. The two thermally activated regions are connected, in some cases, by an athermal region (II in Fig. 1-1) in which the yield stress is believed to depend on temperature only through the shear modulus. (2) Both f.c.c. and b.c.c. structures have many intersecting slip planes. In general, the Burgers vectors of glide dislocations in the cubic system are not perpendicular to that of the forest dislocations. Therefore the elastic interaction between glide and forest dislocations is quite strong as compared to those in some hcp metals in which slip is confined on basal planes.[1] In regions I and III, single crystals of

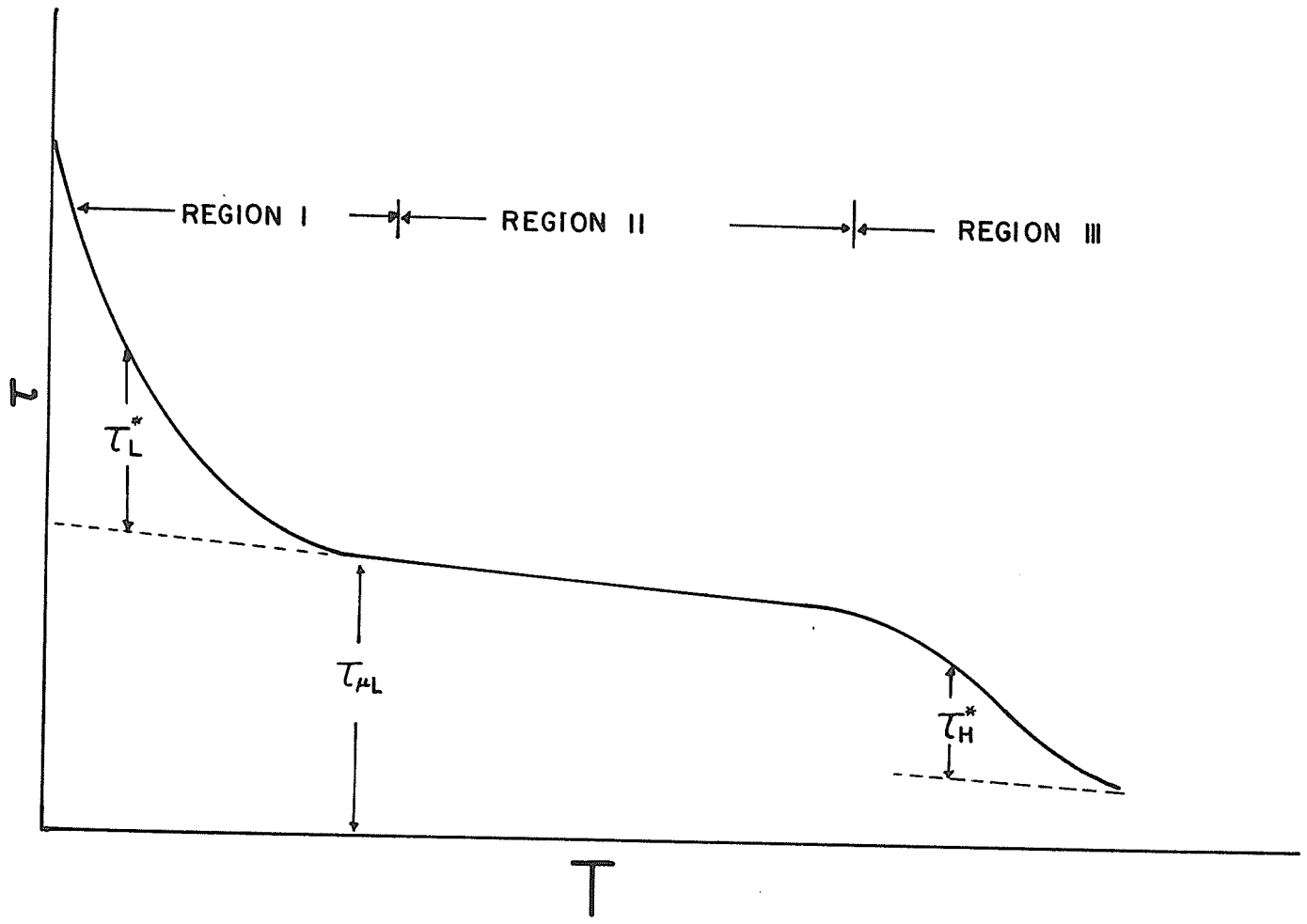

Fig. 1-1 Schematic diagram of the temperature dependence of flow stress in metals.

exhibit three stages of work-hardening, and after a certain amount of deformation, both metals develop similar dislocation substructures.[2] It has been shown quantitatively by Saada[3], Carrington, et al.[4], and Baird and Gale[5] that the interaction between glide and forest dislocations determines, to a large extent, the work-hardening characteristics in these metals. These facts suffice to suggest a further investigation so that a unified dislocation mechanism for plastic flow may be established.

The obstacles encountered by a glide dislocation can in general be divided into short-range and long-range in nature. The short-range obstacles are known to be rate-controlling at low temperatures (<0.2Tm). The flow stress, τ , is then composed of two parts[6]

$$\tau = \tau^* + \tau_\mu \tag{1-1}$$

where τ^* is the effective stress (also called the thermal stress) required to overcome the short range obstacles along with the help of the thermal fluctuations in the crystal lattice, and thus, is temperature dependent. τ_μ is the stress required for the athermal overcoming of the long-range internal stress field. The transition from region I to region II is accomplished by the more frequent thermal fluctuation available in the crystal with increasing temperature. Thus, $\tau = \tau_\mu$ in region II and the work of deformation is done entirely by the applied stress. The internal stress in the temperature region I and II has been attributed to the long-range elastic interaction between a glide dislocation and the dislocations lying on the parallel and intersecting slip planes[7]. Such elastic

interactions can be either attractive or repulsive. However, Saada[3] argued that, in an attractive interaction, a reduction in crystal energy occurs due to the formation of a junction dislocation. Therefore, the attractive interaction is a stronger obstacle to dislocation glide. Sastry and Tangri[11] have further assumed that attractive junctions are the major sources of internal stress in region I and II. The transition from region II to III implies that in region III glide dislocations must either overcome directly the obstacles which cause internal stress in region II or by-pass such obstacles. Plastic flow in region III is known to be thermally activated. Direct overcoming of the elastic interactions requires considerable energy which is supplied by the external forces. By-passing the obstacles, such as cross-slip and climb, is more plausible because less energy is required. There is considerable experimental evidence[8] that plastic flow in region III is controlled by diffusional processes. However, the details of the processes involved are not yet clearly understood.

The dissimilarities in plastic flow between b.c.c. and f.c.c. metals lie mainly at low temperatures (region I in Fig. 1-1). The striking differences are as follows : (1) The flow stress of b.c.c. metals in region I is extremely sensitive to temperature and strain-rate. The temperature sensitivity of flow stress is of the order of 1 MN/m^2deg at the centre temperature of region I in b.c.c. metals[13] as compared to 0.1 MN/m^2deg for f.c.c. metals.[11] (2) Unlike in f.c.c. metals, yield stress of b.c.c. metals is orientation dependent and, in many cases, the Schmid law is not obeyed. (3) There are at least

two sets of slip planes {110} and {112} in b.c.c. metals as compared to one in f.c.c. metals. (4) The stacking fault energies of b.c.c. metals are generally high. Therefore, widely dissociated dislocations are not observed. This can affect the cross-slip and climb behavior of dislocations. (5) The flow stress of b.c.c. metals is very sensitive to impurity content. The impurity atoms, both at interstitial and substitutional sites, can cause hardening and in some temperature and concentration ranges, softening.

It is now becoming more evident that the differences in flow behavior between f.c.c. and b.c.c. metals arise from the distinct core structure of screw dislocations in b.c.c. metals. It was suggested by Hirsch[33] that the screw dislocation core in b.c.c. metals could be extended in a non-planar sessile configuration. The low-energy sessile form must be converted into high-energy glissile form before movement of the dislocation can occur. It has been shown[15] that this mechanism can account quantitatively for the observed lattice friction stress of the correct nature in b.c.c metals. Therefore, it is a logical path to follow that the theories dealing with the low-temperature flow behavior of b.c.c. metals should start with this basic core model of screw dislocations.

The objectives of the major part (part I) of the present research are to study the plastic flow behavior of α-iron in the temperature range 0-0.7 Tm and may be summarized as follows :

(1) to study the nature of the short-range obstacles which give rise to the sharp temperature dependence of the flow stress in iron at low temperatures (region I);

(2) to study the impurity-dislocation interaction and the mechanisms of solution hardening and sofftening;

(3) to investigate the rate-controlling short-range obstacles at high temperatures (region III);

(4) to study the sources of the internal stresses in the three temperature regions and to project a self-consistent picture of all the dislocation mechanisms operating in the three temperature regions.

This study will be limited to the region on the deformation mechanism map having a strain-rate range of typically 10^{-6} - 10^{-2} $sec.^{-1}$

The study of the mechanical properties of pure iron provides the background knowledge for the understanding of the behavior of more complex iron base alloys. In part II, the deformation behavior of a two-phase structure with particular reference to dual-phase steels, will be considered.

A dual phase steel is a mixture of ferrite and martensite. It is generally recognized that this new generation of steel would be of great technological importance in the future. The work-hardening characteristic of a series of dual-phase steels will be investigated using the Bauschinger effect technique.

PART I

THERMALLY ACTIVATED DEFORMATION OF B.C.C. IRON

CHAPTER 2

Literature Review

2.1 PLASTIC FLOW OF B.C.C. METALS AT LOW TEMPERATURES

It has been mentioned earlier that there are striking differences in the plastic flow behavior between f.c.c. and b.c.c. metals at low temperatures (region I in Fig. 1-1). This is the reason that most of the recent research activity in b.c.c. metals is centered around the low temperature region. The characteristic flow behavior of b.c.c. metals can be attributed, in general, to (1) the complexity of the slip systems in b.c.c. metals and (2) the nature of the short-range obstacles which resist the motion of dislocations.

2.1.1 SLIP SYSTEMS IN B.C.C. METALS

Most of the b.c.c. metals except tungsten are anisotropic in their elastic properties. The degree of anisotropy is measured by the Zener factor

$$A = \frac{2C_{44}}{C_{11} - C_{12}}$$

where C_{ij} are the elastic constants. The values of A are listed in Table 1-1.

Table 1-1 Zener factors for b.c.c. metals[14]

Metal	Nb	Mo	V	Cr	W	Ta	Fe	K	Na	Li	β-brass
A	0.51	0.76	0.79	0.86	1.00	1.56	2.36	6.35	8.15	9.4	8.4

This anisotropy can influence the energy of a dislocation and its mobility. From theoretical considerations, Reid[15] has shown that, for $A < 1$, the edge dislocation on {110} planes with a <100> Burgers vectors have the highest mobility. Thus for these metals the possiblity of <100> slip has to be considered. However there is no experimental evidence to conclusively support such a slip. The slip-line analysis of Taylor and Elam[16] shows that slip always occurs in the <111> closed-packed direction and on the zone planes of this direction (pencil glide). Christian[17] has pointed out that, in cases where several slip systems operate, slip-line analysis does not necessarily reveal the true atomic slip planes. It is possible to use

transmission electron microscopy (TEM) to determine the Burgers vectors and the planes in which dislocations lie. Based on the TEM and recent field ion microscopy work, now it is usual to regard that {110} and {112} are the possible atomic slip planes, but {123} slip still remains controversial. Recently, some a<100> and a<110> dislocations have also been observed.[18] However, these dislocations can usually be attributed to reactions, such as formation of attractive junctions between a/2<111> dislocations. There is no experimental evidence that a<100> and a<110> type dislocations contribute to slip. Therefore, the following analysis will be based on the assumption that dislocations in α-iron slip on {110} and {112} planes in the <111> direction. The appearance of these planes based on the hard-sphere model are shown in the Fig. 2-1. The stacking sequence of {110} is ABABAB. Within the framework of the hard-sphere model, a perfect dislocation with Burgers vector b = a/2 [111] on (110) planes can split up into three partial dislocations with Burgers vectors $\underline{b}_1$ $\underline{b}_2$ and $\underline{b}_3$ according to the reaction[19]

$$a/2\ [\bar{1}\ \bar{1}\ 1] \dashrightarrow a/8\ [\bar{1}\ \bar{1}\ 0] + a/4\ [\bar{1}\ \bar{1}\ 2] + a/8\ [\bar{1}\ \bar{1}\ 0] \qquad (2\text{-}2)$$

Vitek[20] has demonstrated that the Burgers vector $\underline{f}$ of a partial dislocation on (110) plane can be generated according to

$$\underline{f} = x \cdot a/2\ [\bar{1}\ \bar{1}\ 0] + y \cdot a/2\ [0\ 0\ 1], \quad 0 < x < 1, \quad 0 < y < 1. \qquad (2\text{-}3)$$

Here $\underline{f}$ is the relative shift of the adjacent atomic planes and thus defines a generalized stacking fault.

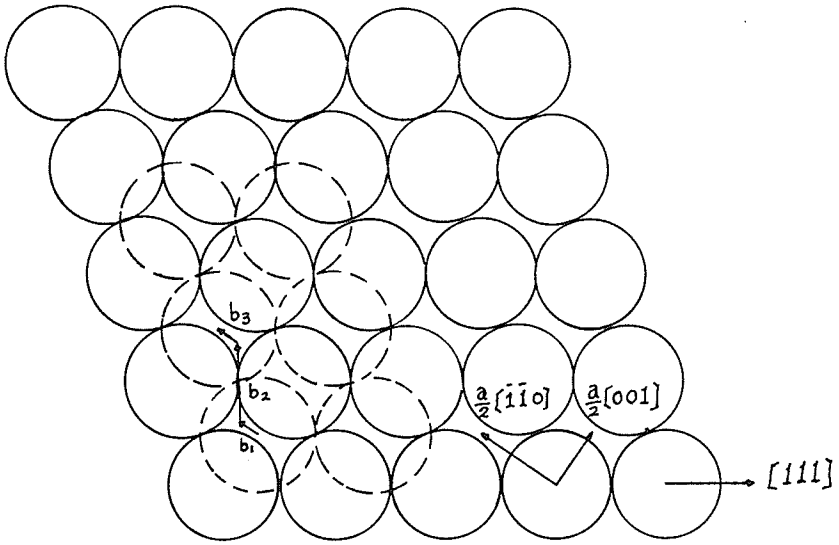

(1$\bar{1}$0) plane

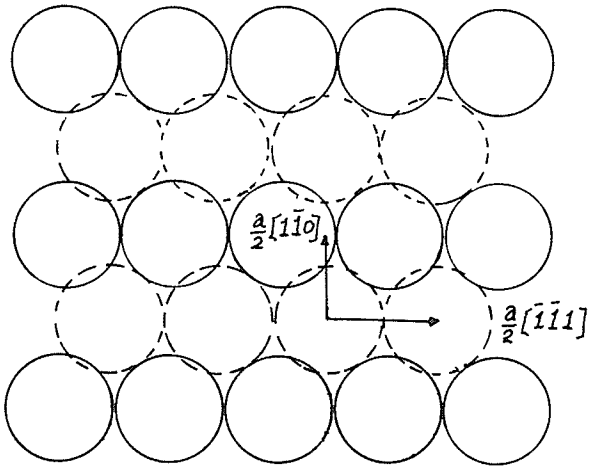

(112) plane

Fig. 2-1 {110} and {112} planes in b.c.c. metals. The dotted circles represent atoms on the top or bottom planes.

The stacking sequence of (112) planes is ABCDEFAB. The possible $\underline{f}$ vectors are

$$\underline{f} = x \cdot a/2\ [\bar{1}\ \bar{1}\ 1] + y \cdot a/2\ [1\ \bar{1}\ 0] \qquad (2\text{-}4)$$

The $\underline{f}$ vectors of 1/6<111> type have been proposed[21] . In fact, they are the twinning vectors on {112} planes. Since split dislocations in b.c.c. crystals are seldom observed in the electron microscope , it is generally believed that the stacking fault energy must be high. However, a b.c.c. lattice can be stable only if the interaction forces between atoms satisfy either of the following conditions[22] :

(1) it is noncentral;

(2) it is a central force but extends beyond the first-nearest neighbour.

Therefore, the atomistic calculations using the interactions forces which satisfy the above stability conditions will generally yield more reliable results. Vitek[23] has performed calculations using three different kinds of interactions forces under the stability conditions and found that there is no stable stacking fault in b.c.c. crystals. Basinski, et al.[24] have also done a similar calculation in sodium in which the effective ion-ion potential is well-known, and found no stable stacking fault in the b.c.c. phase. We therefore can conclude that the instability of a stacking fault is an intrinsic property of the b.c.c. lattice.

The Schmid law has often been found to be disobeyed in some b.c.c. metals such as tungsten[115], molybdenum[116], and niobium.[113,114] The operating slip system is often not the system having the highest resolved shear stress. The anomalous slip occurs in UHV annealed

high purity niobium single crystals when they are stressed in the direction corresponding to the center of the standard triangle. The operating slip systems are the 5th and 7th most highly stressed systems of {110}<111> type.[113,114] The anomalous slip has not been adequately explained. Since niobium has the smallest Zener factor in Table 1-1, the occurrence of the anomalous slip may be related to the small Zener factor. The anomalous slip has not been found in b.c.c. metals with Zener factor greater than one.

2.1.2 THE RATE-CONTROLLING SHORT-RANGE OBSTACLES AT LOW TEMPERATURES

The nature of the short-range obstacles which give rise to the sharp temperature dependence of flow stress in b.c.c. metals has been debated for a number of years, but a consensus has not been reached. The three models that have been most commonly advance are :

(i) the Peierls-Nabarro model,

(ii) the dissociated screw dislocation model

and (iii) the solution hardening model.

The details of these models will be discussed in the following sections. (i) and (ii) are intrinsic in nature because the friction forces which resist the dislocation motion are considered to arise from the b.c.c. lattice itself. Model (iii) is extrinsic because it considers the dispersed impurity atoms as the cause of hardening. One factor which may have hindered the unambiguous differentiation between intrinsic and extrinsic effects is that the materials used by the earlier workers were not sufficiently pure. Stein and co-workers[25] used zirconium purified hydrogen to reduce the carbon concentration in iron to less than 10^{-5} ppm. Altschuler and Christian[26] measured the flow stress of this material and found that the flow stress still depended sensitively on temperature and strain-rate. In the present work, we have investigated the temperature and strain-rate sensitivities of the flow stress of high purity AISI iron (C = 3.5 ppm) and found a substantial lattice contribution to the flow stress. Therefore, it will be concluded that the rate-controlling obstacles in pure b.c.c. iron at low temperatures are intrinsic in nature. Since the flow stress of less pure iron depends

senstively on the impurity content, our major task now is to investigate the role of impurity atoms in modifying the flow stress.

2.1.3 THE SOLUTION HARDENING MODEL

The proponents of the solution hardening model consider the interaction of a glide dislocation with strain fields around dispersed solute atoms, particularly, the tetragonal strain field produced by interstitial solutes. The yield stress has been found to depend on the concentration of the interstitial solutes for concentrations below about 200 wtppm.[25, 27] This has often been used as the supporting evidence for the solution hardening model.

Fleischer[28] assumed an interaction force

$$F = F_0 \, (x/b + 1)^{-2} \qquad (2\text{-}5)$$

where F_0 is the maximum force at x=0 (Fig. 2-2)

The extra energy required to surmount the barrier is given by

$$\Delta G = \int_0^{D'} F \cdot dx - D'F_{app} \qquad (2\text{-}6)$$

where F_{app} is the applied force (Fig. 2-2).

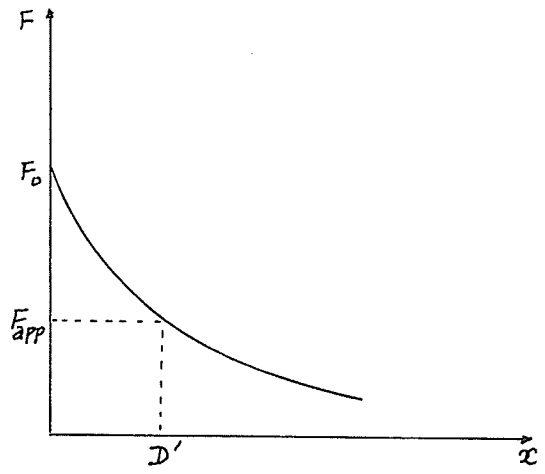

Fig. 2-2 Fleischer's force-distance curve

In a thermally activated process, ΔG is supplied by the thermal fluctuations in the crystal. Based on equation (2 - 5), Fleischer has

derived a simple functional relationship for the effective stress and temperatures.

$$\sqrt{\tau^*/\tau_0^*} = 1 - \sqrt{T/T_c} \qquad (2\text{-}7)$$

where τ_0^* is the effective stress at zero temperature and T_c, the transition temperature between region I and II in Fig. (1-1). Equation (2-7) fits very well the experimental data of lithium fluoride doped with 80 ppm of magnesium.[28] It also fits the earlier data in iron[29] between 300 and 77 K. In view of this, some authors[27, 30] have concluded that the interstitial solute atoms are the cause of hardening at low temperatures. It will be shown later that the results of our investigation at temperatures below 77K, a temperature range more suited for a discriminating appraisal of Fleischer's model, deviate significantly from equation (2 - 7).

2.1.4 THE PEIERLS MODELS

As first pointed out by Peierls [31], the energy of a straight dislocation is a periodic function of position in a direction perpendicular to the close-packed direction. The amplitude of the Peierls energy may be estimated in terms of the variation in the atomic binding energies in the dislocation core. It is necessary to apply a force, τ_p b, per unit length of dislocation to move the dislocation over the Peierls potential hill mechanically. The earlier estimate of the Peierls stress τ_p by Peierls[31] and Nabarro[32] gives

$$\tau_p \simeq \mu \exp(-2\pi w/b) \qquad (2 - 8)$$

where w is the width of dislocations. Equation (2 - 8) is derived from a sinusoidal force-distance curve. w has been considered to vary between 1-10b. Assuming even a rather low value of w = 3b, the Peierls stress is $10^{-9}\mu$ which is seven orders of magnitude less than the theoretical shear stress. Therefore, equation (2 - 8) underestimates the Peierls stress. Guyot and Dorn[50] have shown that the magnitude of the Peierls stress is sensitive to the atomic force law used in the calculation. The question that arises is why the Peierls stress in b.c.c. metals should be so much higher than that in f.c.c. metals of comparable melting points. If the Peierls barrier is indeed the rate-controlling obstacle to dislocation motion in b.c.c. metals at low temperatures, then the higher Peierls stress in these metals must have a common crystallographic origin. This important conclusion was pointed out by Hirsch[33] in 1960. He suggested that the phenomena attributed to a large Peierls barrier in b.c.c. metals were related to the threefold symmetry of <111> screw dislocation axes. This is

borne out by recent atomistic calculations.[23,24,94] The displacement field near the core has the same crystal symmetry along the dislocation line. Under zero external stress, the core of screw dislocation in b.c.c. structure will relax into a starlike arrangement with threefold symmetry, in contrast to the twofold ribbonlike arrangement of edge dislocations in b.c.c. and all dislocations in f.c.c. structure. It is obvious that an extended screw dislocation with three-fold symmetry would not be able to glide easily and that its core would have to undergo a major modification before the dislocation can glide. Hence a high Peierls barrier is expected for screw dislocation in b.c.c. metals. In simple physical terms the high Peierls stress in b.c.c. metals arises solely from the need to effect the sessile-glissile transformation of screw dislocations. This concept has been further extended by several authors[34, 35] who suggest that the core of the screw dislocations in b.c.c. metals, is dissociated into different slip planes, but the width of the dissociation is only a few Burgers vectors. In the modern simplest form, the theory assumes that the core of a screw dislocation is extended into the two slip planes {110} and {112}, commonly observed in the b.c.c. metals, Fig. (2-3a). Thus, the low

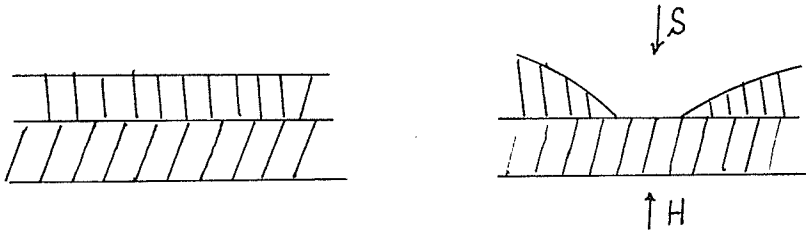

Fig. (2-3) (a) dissociation into {110} and {112} planes. (b) constriction into {110} planes.

energy form of the dislocation is sessile. Before movement of the dislocation can occur, the low energy sessile form must be converted into a higher energy glissile form by constricting the core into the slip plane, Fig. (2-3b). A representative sessile dissociation for a a/2 [1 1 1] screw dislocation is that proposed by Foxall, et al.[34]:

$$\begin{aligned} a/2\,[1\,\bar{1}\,1] \dashrightarrow\ & a/8\,[0\,\bar{1}\,1] && \text{on } (0\,1\,1) \\ + & \ a/6\,[1\,\bar{1}\,1] && \text{on } (1\,1\,1) \text{ or } (1\,2\,1) \\ + & \ a/24\,[8\,\bar{5}\,5] && \text{at the intersection.} \end{aligned}$$

This dissociation involves simple stacking faults on {110} and {112} types of slip planes. This model has the advantage of being able to explain the observed orientation dependence of the yield stress of b.c.c. metals. Because of the nonplanar nature of the core, the mobility of a dislocation will depend not only on the resolved shear stress on the slip plane, but also on that in the constriction plane. In Fig. (2-3b), the arrow marked soft direction indicates that movement of the dislocation in this direction is easier because the applied stress assists the constriction, while the hard-direction requires constriction against the applied stress. Furthermore, since the partial dislocation, a/8 [0 $\bar{1}$ 1] on the (0 1 1) plane is of mixed character, the core configuration will be responsive to the shear stresses acting normal to the total Burgers vector of the undissociated screw dislocation. Based on this model, Duesbery[35] has deduced the following orientation dependence of the axial yield stress for {110} and {112} slip,

$$\sigma_{[101]}^{(t)} \geq \sigma_{[001]}^{(t)} \qquad (2\text{-}9)$$

$$\sigma_{[101]}^{(c)} \geq \sigma_{[001]}^{(t)} \qquad (2\text{-}10)$$

where σ [0 0 1] is the axial yield stress in the [001] direction, and c and t represent compression and tension, respectively. These are in qualitative agreement with the experimental observation.[17] Since the extension of a screw dislocation core is only a few Burgers vectors, the quantitative treatment in terms of elastic interactions between the partial dislocations and of stacking-fault energies is difficult to justify. As a consequence more attention is paid to atomistic calculations. The general features which have been found so far are listed below:

(1) The core of a <111> screw dislocation has three-fold symmetry. The extension occurs on the three zone planes {110}.[23,24,95]

(2) A quantity called "polarity" can be defined in such a way that a positive polarity is assigned to the situation where the relaxation displacement of the atoms closest to the core is in the direction of the Burgers vector, and negative polarity to the opposite case.[94,95] Since the energy of a dislocation does not depend on the sign of the polarity, the occurrence of screw dislocations in either polarity should be equally probable. The "constriction" on a straight dislocation is viewed as the site of changing polarity.[94]

(3) A screw dislocation can advance to the next Peierls potential valley by throwing out double-kinks and by sideways motion of kinks. Consequently, two types of Peierls potentials can be distinguished.

The primary Peierls potential is encounted during the nucleation of double-kinks. The secondary potential is encountered during migration of kinks. Attempts have been made to determine the activation energies of these two processes and the effects of impurity atoms on the activation energies using internal friction technique. (There exists an extensive literature in this specific field of study. See, for instance, 94,96-100 and the references cited in them.)

The results of atomistic calculations are generally sensitive to the interatomic potentials used. Such potentials are not well-known in transitional b.c.c. metals. The calculations made on alkali metals such as sodium[109] and potassium[110] should be more reliable, because the well established pseudo-potential method is applicable on these metals. Unfortunately low-temperature experiment on b.c.c. sodium is not possible due to the martensitic transformation. Recent calculations done on potassium[110] predict an orientation dependence of yield stress in qualitative agreement with experimental results. The potassium crystals used by Basinski, et al.[110] are not very pure, having resistivity ratios between room temperature and 4.2 K of only 200. The extrinsic effects will probably show up at such low purity as will be discussed in the following section.

2.1.5 THE SOLUTION SOFTENING IN DILUTE IRON BASE ALLOYS

There exists an extensive literature on the solution softening in dilute b.c.c. alloys. Since the softening phenomena in various b.c.c. alloys are quite similar, the review in this section will be based on the experimental data in iron based alloys. The study of alloy softening effect may help us to identify the rate-controlling obstacles at low temperatures.

There are twenty-eight elements, including self-interstitials of iron, which cause softening in iron.[36,112] The substitutional elements such as cobalt and chromium cause only hardening, whereas nickel and manganese may cause hardening or softening, depending upon temperature of deformation. The alloying elements may be classified into two types. (1) The potent hardeners, such as C, N, Mn, Ni, Si, Pt, etc., cause strong hardening at high temperatures. The yield stress, in this case, increases with decreasing temperature and reaches a maximum around 300K. Then, it drops sharply between 300 and 200K and falls below the yield stress of unalloyed iron between 100 - 200K. (2) Cobalt and chromium are not effective strengtheners above 300K. They do not cause softening at lower temperatures.

There is a critical concentration for each alloying element which produces maximum softening and this concentration is inversely proportional to the effectiveness of the solute as a strengthening agent.[36] Carbon is a potent hardener above 300 K. Therefore, 180 atppm carbon is enough to cause maximum softening in iron.[37] For nitrogen, which is a less potent hardener, the critical concentration is about 600 atppm.[38] For most substitutional solutes, the critical

concentration is in the neighbourhood of 3 at%.[36]

Recent in situ studies[101] in HVEM have shown that, in the temperature and concentration ranges when solution softening occurs in the Fe-C system, the movement of screw dislocations is characterized by jerky glide, in sharp contrast to the relatively smooth motion of screw dislocations observed in high purity iron. The jerky glide has been interpreted by these authors[101,102] as due to impurity-assisted nucleation of double-kinks.

Irradiation with 2 MeV electrons also causes softening in Battelle iron at 60K.[103] However, these authors do not separate the thermal and athermal components of the flow stress. The softening could be due to the reduction in internal stress.

Three explanations have been given for solution softening. (1) Ravi-Gibala[39] model is based on the Fleischer theory of solution hardening, i.e., the rate -controlling obstacles at low temperatures in b.c.c. metals are the impurity atoms. Their reason for the occurrence of solution softening is that chemical scavenging takes place among the solute atoms and thereby reduces the dislocation pinning centers. It is quite probable that scavenging effects exist. Titanium, for example, will preferentially attract carbon atoms to form carbides. However, if this is the cause of softening, it would occur in the entire low temperature region. Solution softening is generally observed between 100 - 300 K and hardening at both temperature extremes. Solution softening has been found to occur regardless of whether the solute atoms are substitutional or interstitial, whether the solute reacts strongly or not with

interstitial solutes.[36] Therefore, solute scavenging cannot be the cause of softening. (2) Sato - Meshii[40] model is based on the Peierls model, i.e., the rate-controlling mechanism for pure b.c.c. metals at low temperatures is the overcoming of the Peierls barrier by screw dislocation. They consider the motion of a screw dislocation through a combined field of Peierls potential and misfit strain produced by solute atoms and find that the misfit strain assists the nucleation of double-kinks, but impedes the sideward motion of kinks. The results of their calculation predict that solution hardening occurs in the higher temperature range ($T > 100$ K) and softening at lower temperatures. Again this is inconsistent with experimental observations that softening occurs between 100 and 300 K for most solutes in iron. (3) Wuthrich and Frank[41] unify the solution hardening model of Fleischer and the dissociated dislocation model to develop their explanation of solution softening. They assume that solute atoms impede sessile - glissile transformation of screw dislocations. The result of their calculation is in qualitative agreement with experimental observations. That is, solute atoms cause softening between 100 and 200 K and hardening at other temperatures. The physical reason for the occurrence of softening is that the activation energy for the constriction of an extended screw dislocation is proportional to the average distance between two neighboring solute atoms. This energy decreases with increasing solute concentration. We will discuss this model again in more detail in section 4.1.3.

In summary, the extended screw dislocation core model is the most promising model to explain the strong temperature sensitivity of flow stress in iron at low temperatures. Solute atoms do cause strong hardening and, in some temperature and concentration ranges, softening in iron.

2.2. PLASTIC FLOW AT INTERMEDIATE AND HIGH TEMPERATURES

It has been mentioned in the previous section that mobile dislocations in b.c.c. metals at low temperatures encounter two types of barriers. They are the localized Peierls barrier and the long-range internal stress due to the interaction with another dislocation or a group of dislocations . The effective stress which acts on a mobile dislocation is $\tau^* = \tau - \tau_\mu$. As the temperature increases, the available energy fluctuations in the lattice also increase. Consequently the τ^* decreases. A transition temperature, T_c, can be practically determined such that at $T > T_c$, $\tau^* = 0$. That is in Region II, the localized Peierls barrier becomes transparent to the screw dislocations. The deformation is done entirely by the applied stress to overcome the long-range stress. The characteristic features observed in b.c.c. metals at low temperatures, such as long straight screw dislocations, delayed cell formation, and the invalidation of Schmid law, vanish in region II. As pointed out in section 1 deformation behavior of b.c.c. metals in region II ressembles that of f.c.c. metals. The important point here is the origin of τ_μ . Leslie[36] has shown that the athermal behavior of iron in region II is observed only in the case of the initial yield stress and that the flow stress is again temperature dependent. Sastry, et al.[12] also observed similar behavior in copper, copper - aluminum alloy, and molybdenum. If τ_μ is due to the long-range elastic interaction between dislocation stress fields, it is difficult to explain why the flow stress in region II is temperature dependent at larger strains. Furthermore, as the temperature increases, the yield

and flow stresses depend on temperature and strain rate again (i.e., region III of Fig. 1-1). The long-range stress field between dislocations can not be overcome by thermal activation in this temperature range. Therefore, τ_μ in regions I and II can not be ascribed solely to the long-range elastic interaction between dislocations.

The high temperature plastic flow (region III) is also thermally activated. Following the same concept as in region I, the obstacles to dislocation motion can be divided into long - range and short - range obstacles. However, the nature of these obstacles have yet to be clarified. In the following two sections we consider the intersection and diffusion controlled processes.

2.2.1 INTERSECTION MECHANISM

When a dislocation glides on its slip plane, it will meet forest dislocations piercing through the slip plane. Such elastic interactions between mobile and forest dislocations are relatively strong in the f.c.c. and b.c.c. structures because the Burgers vector of a mobile dislocation is not, in general, perpendicular to the Burgers vector of the forest dislocation. The interaction can be either attractive or repulsive depending on the relative orientations of the Burgers vectors. The stresses required to cut an attractive or a repulsive forest dislocation would be exactly the same if the dislocations were straight and rigid under the action of stress. Carrington, et al.[4] and Saada[3] have studied this problem in some detail and concluded that it is more difficult on the average for a mobile dislocation to cut across an attractive tree than a repulsive one, because dislocations are flexible. In the attractive case, the quadruple node (Fig. 2 - 4) will split into two triple nodes. This reaction reduces energy and therefore stabilizes the system.

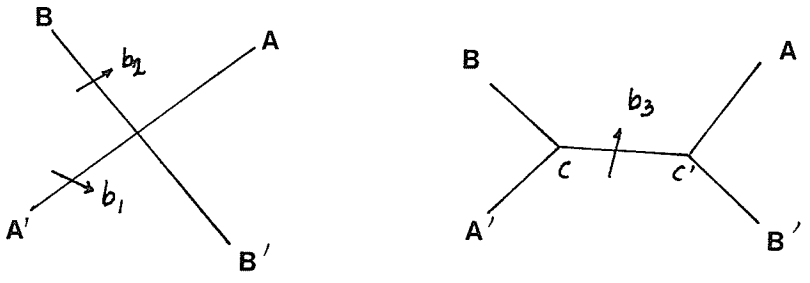

Fig. 2 - 4 Junction Reaction

2.2.2 DIFFUSION CONTROLLED PROCESSES

There exists ample evidence in the literature that the diffusion controlled processes do play an important role in the high temperature plastic flow of metals. Sherby and Burke[42] and Sherby and Miller[43] have compiled the existing data and come to the conclusion that the activation energies for the steady state creep are equal to the self-diffusional energies. Since the diffusional processes are thermally activated, the steady state strain rate is usually described by an empirical constitutive equation of the Arrhenius form

$$\dot{\varepsilon}_s = f(\sigma, \alpha, T) \exp(-Q/kT) \tag{2-15}$$

where $f(\sigma,\alpha,T)$ is a function of applied stress, stacking fault energy and temperature, and Q is the activation energy for steady state creep which is equal to the self-diffusion energy Q_{SD}. Following Mukherjee, et al.,[44] the function f is represented by a power function of stress. Equation (2-15) can be rewritten as

$$\dot{\varepsilon}_s = A' (\mu b/kT) (\sigma/\mu)^n D \tag{2-16}$$

where μ is the shear modulus and D is the self-diffusion coefficient. A′ contains the stacking fault energy and structure factors. The power n varies between 1 and 5, depending on stress. The description of steady-state creep in terms of equation (2-16) is only phenomenological and is not always perfect, as has been pointed out by Poirier.[45] He has shown that the Arrhenius plots of five pure metals are concave upwards and that the region where the activation

Fig. 2 - 4 shows that a mobile dislocation AA′ of Burgers vector $\underline{b}_1$ meets a tree BB′ of Burgers vector $\underline{b}_2$. They react to form a junction dislocation CC′ of Burgers vector $\underline{b}_3$,

$$\underline{b}_3 = \underline{b}_1 + \underline{b}_2 \tag{2-11}$$

Since the self-energy of a dislocation line is proportional to the square of its Burgers vector, the reaction in equation (2-11) is energetically favorable if

$$b_1^2 + b_2^2 > b_3^2 \tag{2-12}$$

From equation (2-11) we get

$$b_1^2 + b_2^2 + 2\,\underline{b}_1 \cdot \underline{b}_2 = b_3^2 \tag{2-13}$$

Therefore, for a junction reaction to occur, one must have

$$\underline{b}_1 \cdot \underline{b}_2 < 0 \tag{2-14}$$

Saada's[3] quantitative estimate shows that the hardening due to the attractive trees predominates over that due to the repulsive trees and also over the hardening due to the long - range elastic interaction between dislocations. Sastry and Tangri[11] have proposed that the attractive junctions are the main source of internal stress at low and intermediate temperatures. This mechanism will be discussed in more detail in section 4.

energies for creep and self-diffusion coincide is limited, usually begins only about 0.6 or 0.7 Tm and does not always extend to the melting point. He therefore suggests that there exist parallel mechanisms which are competitive with the diffusion controlled climb at $T > 0.5$ Tm. In response, Sherby and Weertman[46] argue that $Q < Q_{SD}$ observed for some metals at temperatures near 0.5 Tm can be explained in terms of the dislocation pipe diffusion. Their evidence in support of the contention that the diffusion controlled process is the rate-controlling mechanism for steady-state creep is that the activation energy for creep is equal to the activation energy for self-diffusion for 21 metals.

The theories based on diffusion-controlled dislocation motion can be classified into two groups: those based on the glide of jogged screw dislocations and theories based on climb of edge dislocations.

The theories based on the glide of jogged screw dislocations are concerned with the chemical force on the jog. The chemical force arises from the nonequilibrium vacancy concentrations near the jog when it moves nonconservatively by absorbing or emitting vacancies. The problems associated with this model are :

(1) the densities of vacancy absorbing and emitting jogs and

(2) the diffusion path.

The jogs on a screw dislocation can be created either by intersection with forest dislocations or by thermal activation such as cross-slip. Based on Cottrell's theorem, Weertman[71] argues that there is a net number of vacancy absorbing jogs on a screw dislocation. Others[104,105] assume that the two types of jogs are

equally probable. The distribution of jogs affect the diffusion path of vacancies. If both types of jogs are distributed on a screw dislocation, the fast diffusion path would be the dislocation core. However, if only one type of jog is allowed, the lattice diffusion is quite possible. The resulting strain rate equation depends on the choice of these assumptions. For example, if both type of jogs are equally probable, the steady-state strain rate is given by[104]

$$\dot{\varepsilon} = 2\pi \rho_s DZ (b/a)^3 \sinh (\sigma b^2 \ell / 2kT)$$

where ρ_s is the mobile screw dislocation density, D the diffusion coefficient depending on the choice of diffusion path, z the number of atoms per unit cell, and ℓ the interjog spacing. Other symbols have the usual meaning. The primary difficulty of the jogged screw dislocation model is the prediction of the stress exponent in the strain rate equation. Our present data indicate that ℓ decreases with increasing stress. Therefore, the stress dependence of the steady-state strain rate in the above equation would be essentially contained in ρ_s. This requires that ρ_s is at least proportional to the fourth power of stress. This is not in accord with the well establised rule that dislocation density is proportional to the square of stress. Furthermore, if the strain rate is controlled by the motion of screw dislocations, then there would be more screw dislocations than edge dislocations in the deformed crystals. This is in contradiction with experimental observations.[44]

The theories based on climb of edge dislocations can be divided into two main groups. (1) Nabarro's creep theory[106] assumes that the strain is produced by climb of edge dislocation. This theory

underestimates the steady-state strain rate for most pure metals.[47] (2) Weertman's creep theory[71] and its variants[47] assume that strain is produced by glide and that the strain rate is controlled by the climb at the head of pile-ups. The argument against this model is that pile-ups are not generally observed.

In pure metals after deformation in region III, dislocations usually arrange themselves into 3-dimensional network. Several high temperature deformation theories[73,76,107,108] are concerned with the growth of network based essentially on the classical recovery-creep concept. Again, the strain rate equations differ from theory to theory, depending on the specific assumptions made on the climb processes and the diffusion path. Evans and Knowles[76] consider the climb of link dislocations as well as nodes and derive a more general type of strain rate equation given by

$$\dot{\varepsilon} = \text{constant}\ \frac{\sigma^3 b}{kT}\left[\frac{D}{\ln\left(\frac{\mu}{2\sigma}\right)} + \frac{3D_p\,\sigma^2}{\mu^2}\right]$$

where D_p is the pipe diffusion coefficient. Spingarn, et al.[63] derive a similar equation as above by taking into consideration the curvature of dislocations during climb. These theories predict a stress exponent which may vary between 3 and 5, depending on the dominant diffusion path.

The dislocation distribution during steady-state flow is inhomogeneous. High densities of dislocation are found in the subboundaries and at least one order of magnitude less in the subgrain. Therefore, the network growth model would be more applicable at the subboundaries.

The inhomogeneity of dislocation distribution would also give rise to the internal stress. Several authors[48,49,105] take the view that the internal stress at steady-state flow is established by the balance between strain hardening and recovery. Strain hardening is caused by glide-controlled generation of dislocations, while recovery is due to climb-controlled annihilation of dislocations. Therefore, glide and climb are interdependent processes.

In conclusion, there is considerable evidence that the steady-state flow of pure metals is controlled by diffusion. However, our understanding of the rate-controlling mechanism is still incomplete. The theories based on the climb of edge dislocations generally predict that the strain rate is proportional to third power of stress, whereas stress exponents greater than 4 are usually observed. The formation of dislocation substructure and internal stress associated with it should be carefully investigated.

2.3. THERMODYNAMICS OF PLASTIC FLOW

It is generally accepted that the plastic flow of metals at low and high temperatures (region I and III) is thermally activated. The shear strain-rate is given by the general equation of Arrhenius type

$$\dot{\varepsilon} = \dot{\varepsilon}_o \ (\tau, T) \ \exp(-\Delta G/kT) \qquad (2\text{-}17)$$

where $\dot{\varepsilon}_o = NA_f b \nu$,

N = density of activation site,

A_f = area swept after a successful event,

ν = vibration frequency of the dislocation segment,

τ = flow or effective stress,

ΔG = Gibbs free energy = $\Delta H - T \Delta S$

ΔG cannot be evaluated directly from the experimental data. The problem here is that the pre-exponential factor $\dot{\varepsilon}_o$ is not known. There are two ways one can proceed further : (1) build a theoretical model and derive $\dot{\varepsilon}_o(\tau, T)$ in terms of the known quantities such as temperature and stress[50]; (2) make an assumption that $\dot{\varepsilon}_o$ is a certain function of τ and T.[51] Following either of these methods, one can evaluate ΔG from equation (2-17),

$$\Delta G = kT \ell n \ (\dot{\varepsilon}_o / \dot{\varepsilon}) \qquad (2\text{-}18)$$

ΔG can be visualized from the obstacle-dislocation interaction force diagram (Fig. 2-5).

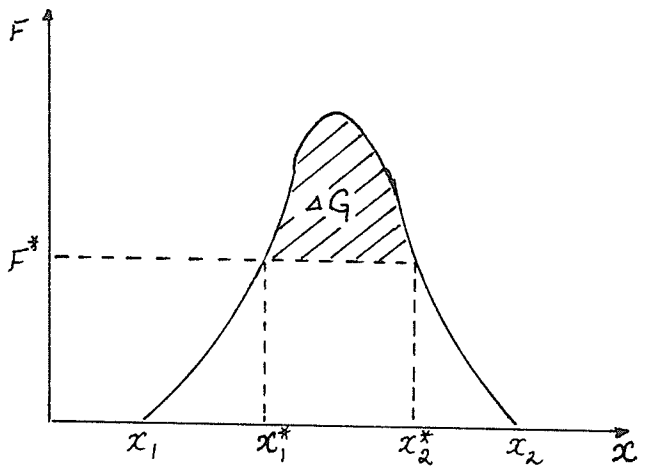

Fig. 2-5 Force Distance Diagram

Under the force F^*, the equilibrium positions are x_1^* and x_2^* The shaded area is G. Therefore, G may be written as

$$\Delta G = \int_{x_1^*}^{x_2^*} F dx - \tau^* b \ell (x_2^* - x_1^*) \tag{2-19}$$

where ℓ is the length of the dislocation segment involved in the activation process. The slip distance during activation $x_2^* - x_1^*$ is usually represented by the activation area $A^* = \ell (x_2^* - x_1^*)$, or volume $V^* = bA^*$, i.e.

$$V^* = bA^* = b \ell (x_2^* - x_1^*) \tag{2-20}$$

The total free energy is given by

$$\Delta G_o = \int_{x_1}^{x_2} F \, dx \tag{2-21}$$

which is the free energy at zero effective stress, an important characteristic of the obstacle. The activation enthalpy, entropy, and volume are given by the thermodynamic relationships

$$\Delta G = \Delta H - T\Delta S \tag{2-22}$$

$$\Delta H = \left[\frac{\partial \, (\Delta G/T)}{\partial \, (1/T)} \right]_{\tau} \tag{2-23}$$

$$\Delta S = - \left(\frac{\partial \Delta G}{\partial T} \right)_{\tau} \tag{2-24}$$

$$V^* = - \left(\frac{\partial \Delta G}{\partial \tau} \right)_{T} \tag{2-25}$$

These thermodynamic variables are useful for the identification of the rate-controlling obstacles. Again these variables cannot be

determined directly from experimental data without making further assumptions. The apparent or experimental activation volume and enthalpy are defined by

$$V_a^* = kT \left(\frac{\partial \ell n \dot{\varepsilon}}{\partial \tau} \right)_T \tag{2-26}$$

$$\Delta H_a = -k \left[\frac{\partial \ell n \dot{\varepsilon}}{\partial (\frac{1}{T})} \right]_{\tau^*} = - TV_a^* \left(\frac{\partial \tau^*}{\partial T} \right)_{\dot{\varepsilon}} \tag{2-27}$$

Equation (2-26) and (2-27) can be obtained from (2-23) and (2-25) by setting $\dot{\varepsilon}_o$= constant. Therefore, V_a^* and ΔH_a, in general, are not true thermodynamic variables defined by equation (2-23) and (2-25). It has been shown by Surek, et al.[51] that ΔG can be evaluated from H and V^* by

$$\Delta G = \frac{\Delta H + V^* \tau \cdot \frac{T}{\mu} \frac{d\mu}{dT}}{1 - \frac{T}{\mu} \cdot \frac{d\mu}{dT}} \tag{2-28}$$

based on the assumption that the obstacle-dislocation interaction force is proportional to the shear modulus μ,

$$F = \mu(T) g(x) \tag{2-29}$$

where $g(x)$ is an unspecified function of distance. ΔG can be calculated from experimental data in two cases[52] :

(1) $\dot{\varepsilon}_o$ = constant, (2) $\dot{\varepsilon}_o$ is a function of modulus reduced stress $\dot{\varepsilon}_o = f\ (\tau / \mu)$. Then,

$$\Delta G = \frac{\Delta H_a + V_a^* \tau^* \frac{T}{\mu} \frac{d\mu}{dT}}{1 - \frac{T}{\mu} \frac{d\mu}{dT}} \qquad (2\text{-}30)$$

It will be shown that the first condition, i.e. $\dot{\varepsilon}_o$ = constant, is satisfied by the Ferrovac E iron at low temperatures. In this case, $\Delta H = \Delta H_a$, $V^* = V_a^*$, and $\Delta G \approx \Delta H_a$. The condition (2) is found to hold in the high temperature deformation of Fe, Mg, Zr, and ice.[52]

CHAPTER 3

EXPERIMENTAL PROCEDURES

3.1 SPECIMEN PREPARATION

The vacuum-induction-melted Ferrovac E iron was purchased from Crucible Steel Company of America. The chemical analysis in wt% is shown in Table (3-1). Rods of 12.5 x 12.5mm cross-section were cut from the as-received slab and cold-swaged into a diameter of 6.5mm without intermediate anneal. They were machined into cylindrical specimens of dimensions 2 cm(gauge length) by 3 mm(diameter) with 1/4" x 20 threaded ends. Annealing at 850^{o} C for one hour resulted in an average grain diameter of 48 μm. These specimens were used for both cryogenic and high temperature tests. The ultra-high purity iron used at low temperature tests was produced at the Battelle Laboratory of the American Iron and Steel Institute, bearing the identification number 122-d. The impurity contents are shown in Table (3-2). The cylindrical specimens having dimensions 2 cm (gauge length) by 3.5 mm (diameter) were machined from this material. Heating in the dynamic vacuum of 5×10^{-6} torr at 800^{o} C for 10 minutes produced an average grain diameter of 1 mm.

Table (3-1)

Chemical Analysis of Ferrovac E Iron in wt%

C	Mn	P	S	Si	Ni	Cr
0.005	0.001	0.002	0.006	0.006	0.021	0.002

Mo	V	W	Co	Cu	Al	Sn
0.001	<0.004	0.01	0.003	0.001	0.01	.003

Pb	N	O
0.0005	0.003	0.03

Table 3-2 Analysis of AISI-Battelle iron. All analyses are ppm by weight.

Nonmetallic Impurities	
Oxygen	2.5
Nitrogen	1.0
Hydrogen	0.16
Carbon	
Combustion-Conductometric	3.5
Sulfur	1.00
Mass Spectrometer	

Total nonmetallic impurities 8.

Metallic Impurities Often Detected With the Mass Spectrometer
(Impurities not detected are denoted N together with the estimated detection limits)

Aluminum	2.000	Nickel	N<1.000
Arsenic	0.100	Phosphorus	0.050
Boron	0.002	Potassium	0.030
Calcium	5.000	Silicon	N<0.500
Chromium	1.000	Sodium	3.000
Cobalt	0.200	Tantalum	N<0.300
Columbium	N<0.050	Tin	0.050
Copper	10.000	Titanium	0.100
Germanium	N<2.000	Tungsten	0.050
Magnesium	0.1000	Vanadium	N<0.050
Manganese	3.000	Zinc	N<0.200
Molybdenum	N<0.050	Zirconium	N<1.000

Total detected metallic impurities 27.
(Includes values marked ≤ except germanium, and values underlined below plus an arbitrary 2 ppm aluminum.)

Metallic Impurities not Usually Detected With the Mass Spectrometer
(Impurities detected in this bar are underlined)

Antimony	N<0.02	Holmium	N<0.02	Rubidium	N<0.02
Barium	N<0.02	Indium	N<0.5	Ruthenium	N<0.02
Beryllium	N<0.005	Iodine	N<0.03	Samarium	N<0.03
Bismuth	N<0.01	Iridium	N<0.02	Scandium	N<0.100
Bromine	N<0.1	Lanthanum	N<0.01	Selenium	N<2.00
Cadmium	N<0.2	Lead	0.03	Silver	N<0.05
Cerium	N<0.01	Lithium	N<0.002	Strontium	N<0.02
Cesium	N<0.01	Lutetium	N<0.01	Tellurium	N<1.0
Dysprosium	N<0.03	Mercury	N<0.03	Terbium	N<0.01
Erbium	N<0.05	Neodymium	N<0.1	Thallium	N<0.02
Europium	N<0.02	Osmium	N<0.03	Thorium	N<0.01
Gadolinium	N<0.03	Palladium	N<0.02	Thulium	N<0.03
Gallium	N<0.05	Platinum	0.5	Uranium	N<0.01
Gold	N<0.1	Praseodymium	N<0.02	Ytterbium	N<0.03
Hafnium	N<0.03	Rhenium	N<0.02	Yttrium	N<0.05
		Rhodium	2.0		

3.2 THE CRYOSTAT AND HIGH TEMPERATURE APPARATUS

The cryostat design, capable of maintaining constant temperatures between 2 and 300 K, is shown in Fig. (3-1). In the temperature range 77 to 300 K, the inner dewar is filled with liquid nitrogen. Below 77 K liquid helium is used. The specimen is cooled by the helium gas trapped in the diving bell. Any desired temperature above the normal boiling point of refrigerant is achieved by regulating the power input into the heating elements of the upper and lower specimen grips. The power input to the heating coils is automatically controlled by a Cryogenic Research Company Temperature Controller model TC - 103. The temperature of the specimen is accurately monitored by the germanium and carbon resistance thermometers located at the center and the top end of the specimen. The temperature fluctuation along the specimen can be controlled within 1^0 K. Tests above room temperature were conducted in argon atmosphere. The stainless steel specimen chamber was surrounded by a three-zone furnace. The temperature of the specimen was monitored by a Pt - Pt + 13% Rh thermal couple.

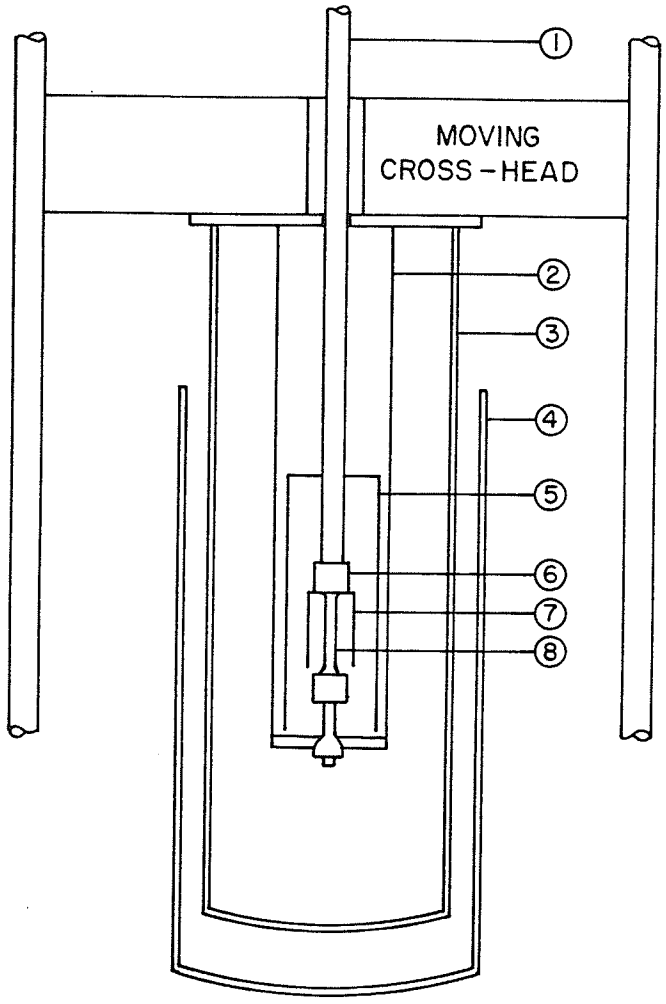

① PULL ROD
② COMPRESSION TUBE
③ LHe DEWAR
④ LN_2 DEWAR
⑤ DIVING BELL
⑥ HEATER and GRIP
⑦ COPPER SHIELD
⑧ SPECIMEN

Fig.3-1 Cryostat.

3.3 TESTING PROCEDURE.

(A) Low temperature tensile deformation (T < 300 K).

All the Ferrovac E specimens were pre-strained at room temperature to beyond Lüder's strain region ($\simeq$ 3.5% strain) to prevent inhomogenous deformation and to inhibit twinning at low temperatures. The high purity AISI iron was fairly ductile at low temperatures. No yield drop and twinning were observed. As such, all these specimens were tested without any pre-straining at room temperature. Two types of test were performed :

1. Differential-temperature tests.

The specimen was deformed at temperature T_1 at a strain rate of 0.0025 min.$^{-1}$. Then the cross-head was stopped and the temperature of the specimen was decreased by a few degrees to T_2. The plastic flow was resumed at T_2, Fig. 3-2a. If the dislocation structure remained constant during the temperature change, then the increase in the flow stress could be attributed to the increase in the thermal component of the flow stress. The temperature sensitivity of the effective stress, $\Delta\tau^* / \Delta T$, could be evaluated.

2. Strain rate cycling tests.

The specimen was deformed into the plastic region at a given temperature employing a base strain rate of 0.0025 min.$^{-1}$. Then the strain rate was increased by a factor 10 and the change in the flow stress measured. If we made the assumption that the long-range internal stress remained constant at the moment of strain rate increase, then the increase in flow stress could also be attributed to the increase in the effective stress. The strain rate

sensitivity of the effective stress, $\Delta\tau^*/\Delta \ln \dot{\varepsilon}$, could be evaluated. The temperature was decreased by 5 to 15° K and the accompanying change in flow stress was noted. The strain rate cycling test was again imposed at the new temperature. These data were used to evaluate the activation volume and enthalpy.

(B) High temperature tensile deformation.

Two types of tests were performed : (1) Strain rate cycling tests were carried out up to 50% strain at temperatures between 300 and 800° C. The Cottrell-Strokes ratio was calculated from the flow stress change associated with a factor 2 change in the strain rate divided by the flow stress, Fig. (3-2b). These data were also used to calculate activation volumes. (2) The second type of tests were performed to determine the yield stress and the steady state flow stress. The specimens were pulled to fracture between 400 and 800° C in the strain rate range 10^{-5} to 8×10^{-3} sec.$^{-1}$ The creep-like $\log\sigma$ versus $\log \dot{\varepsilon}$ relationship were established.

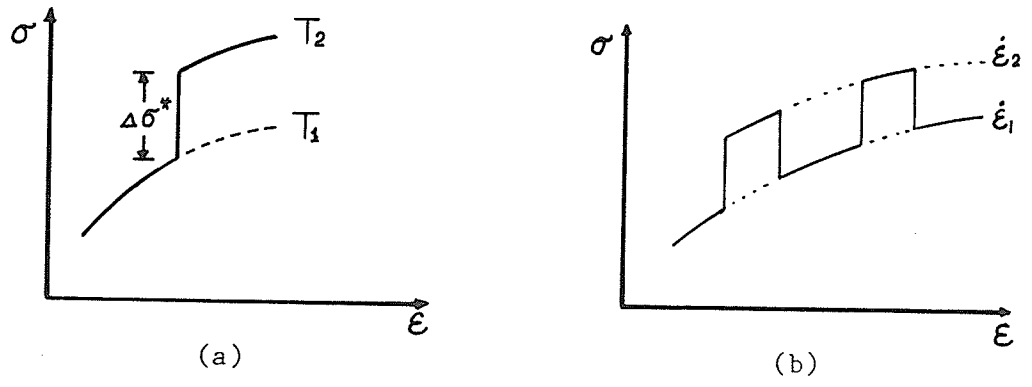

Fig. (3-2) (a) Differential-temperature tests, (b) strain rate cycling tests.

CHAPTER 4

RESULTS AND DISCUSSIONS

4.1 PLASTIC FLOW OF α-IRON BETWEEN 0-300K (REGION I)

The two factors which may have hindered the unambiguous identification of the rate-controlling obstacles in region I are (1) the presence of impurities in iron and (2) the effective stress τ^* data below 77 K. Impurity atoms can increase or decrease the flow stress of iron depending on their concentration and temperature. Among the elements investigated so far, carbon is the most effective to cause hardening in iron. The present work includes materials of two different purities : (1) the Ferrovac E iron which is most commonly used by the previous investigators and (2) the AISI-Battelle iron which is produced at Battelle Laboratory.

Most of the reports in the literature regarding the low temperature deformation behavior of iron are concerned with yield stress rather than the effective stress measurements. One encounters two major problems in the yield stress measurements. Firstly , the initial yield stress is more sensitive to the sensitivity of the machine even when the yield criteria such as the proportional limit and yield stress at 0.2% proof strain, etc. are specified. Secondly, one is faced with problems such as the dislocation source operation and the effects of impurities on the density and distribution of dislocations at the initial yield. The so-called stage 0 is mainly due to the glide of the more mobile edge dislocations. Therefore, yield stress may not represent the true effective stress. The present investigation employs the differential-temperature testing technique

to determine the temperature dependence of the effective stress without recourse to the internal stress measurements and thus avoiding the aforementioned difficulties.

4.1.1 FERROVAC E IRON

Ferrovac E iron of this composition (Table 3-1) is ductile at low temperature. Deformation twinning can be completely suppressed by pre-straining at room temperature to beyond the Luders's strain region ($\approx$3.5% strain). Fig. (4-1a) shows the recrystallized Ferrovac E iron. Fig (4-1b) shows the microstructure of the deformed specimen which was not pre-strained at room temperature. This specimen was used in the differential-temperature test at 23.0, 19.5, 14.4, and 9.5^0 K. It can be seen that twinning is a competitive mode of deformation. On the other hand, Fig. (4-1c) show the microstructure of the pre-strained specimen which was deformed at 77, 50, 35, 20, and 10K. Necking occured at 10K. This picture shows the elongated grains in the neck region. No deformation twins are observed.

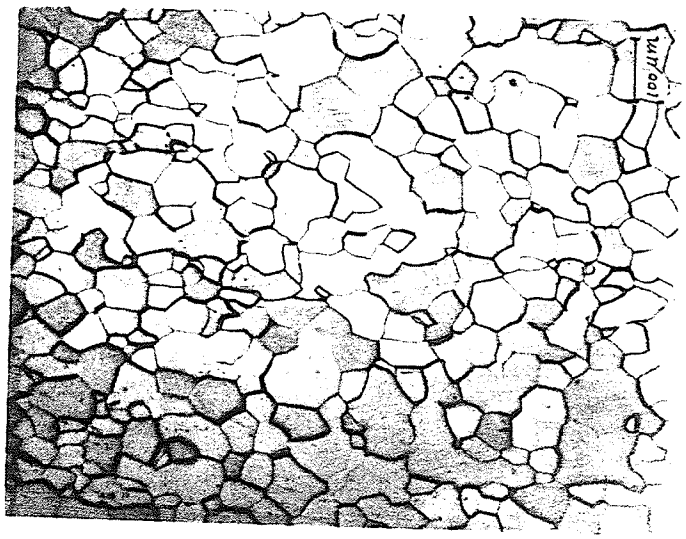

Fig. 4-1 (a) Recrystallized Ferrovac E iron.

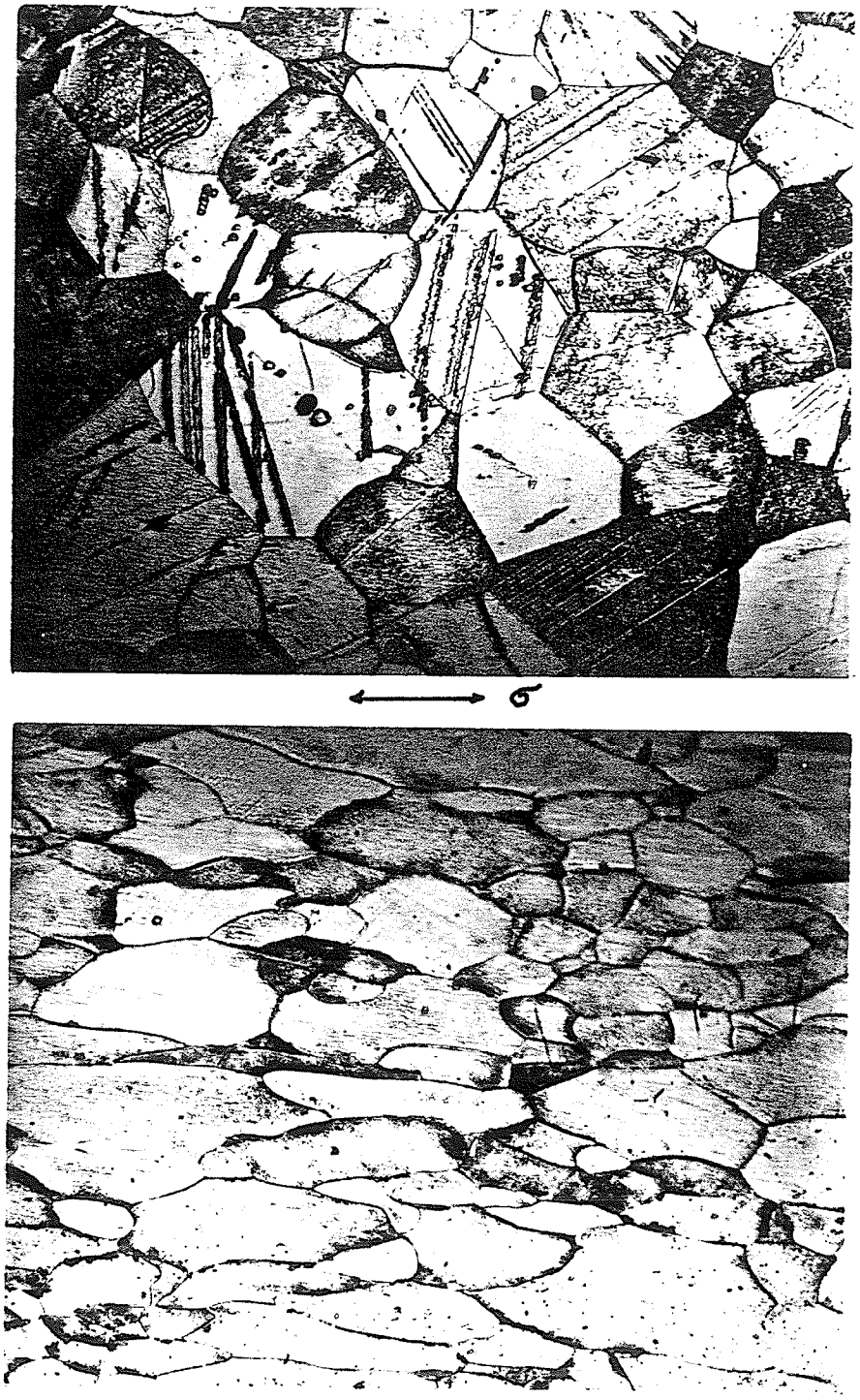

Fig. 4-1 (b) without pre-straining at room temperature, twinning is a competitive mode of deformation. (c) with 3.5% pre-strain, elonged grains in the neck region after deformation at 10 K.

The results of the differential temperature tests are documented in Fig. 4-2 wherein the change in the shear stress per unit temperature change is plotted against temperature. Shear stress is derived from tensile stress by employing a Taylor factor of two. The solid curve represents the least square fit of the experimental data. Fig. 4-2 also shows that the linear relationship is valid between 300 and 70K. Below 70K, however, $-\Delta\tau^*/\Delta T$ increases more rapidly with decreasing temperature than predicted by Eq. (4-1). The transition temperature T_c from region I to region II is deduced from Fig. 4-2 to be 300K for $\dot{\varepsilon} = 0.0025\ \text{min}^{-1}$. This is in fair agreement with the T_c values reported in the literature for comparable strain rate.[54] T_c is the temperature at which the thermal fluctuation is enough to comply with the applied strain-rate.

The effective stress τ^* can be obtained by either cumulative summing up of the stress increments derived from differential temperature tests (dots in Fig. 4-3) or numerically integrating $\partial\tau^*/\partial T$ shown in Fig (4-2). The result is represented by the solid line AC in Fig. (4-3). It can be seen in Fig. (4-3) that both methods yield the same results. If the Smidt's linear approximation, Eq. (4-1), is employed in the integration, one obtains the curve AD. Although the deviations between AC and AD are not great, the differences in the slopes of both curves are quite significant. Therefore, the temperature sensitivity, $\partial\tau^*/\partial T$, will be used as a criterion for the comparison of the τ^*---T profiles of various materials.

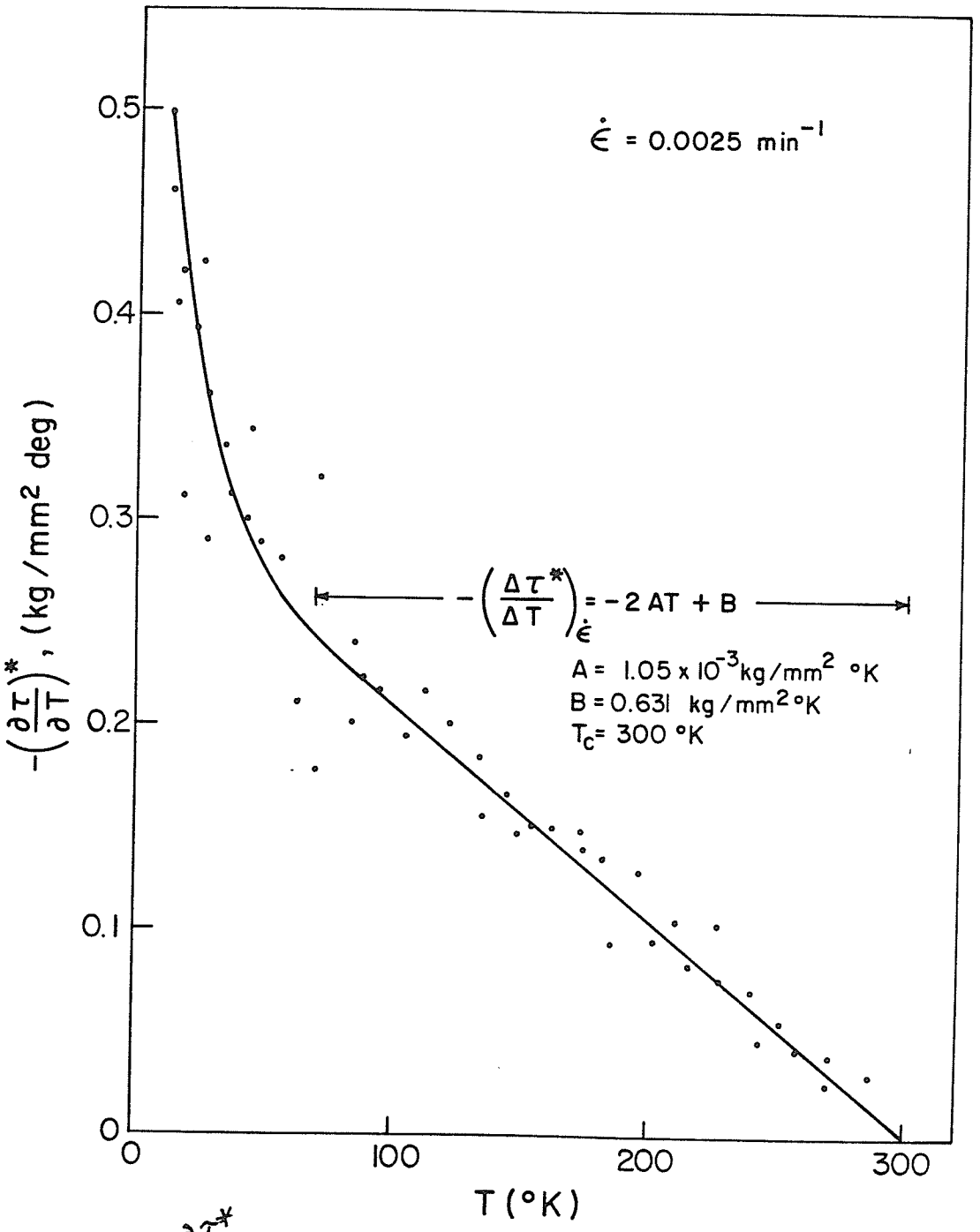

Fig.4 -2 $\partial\tau^*/\partial T$ determined from temperature-change tests.

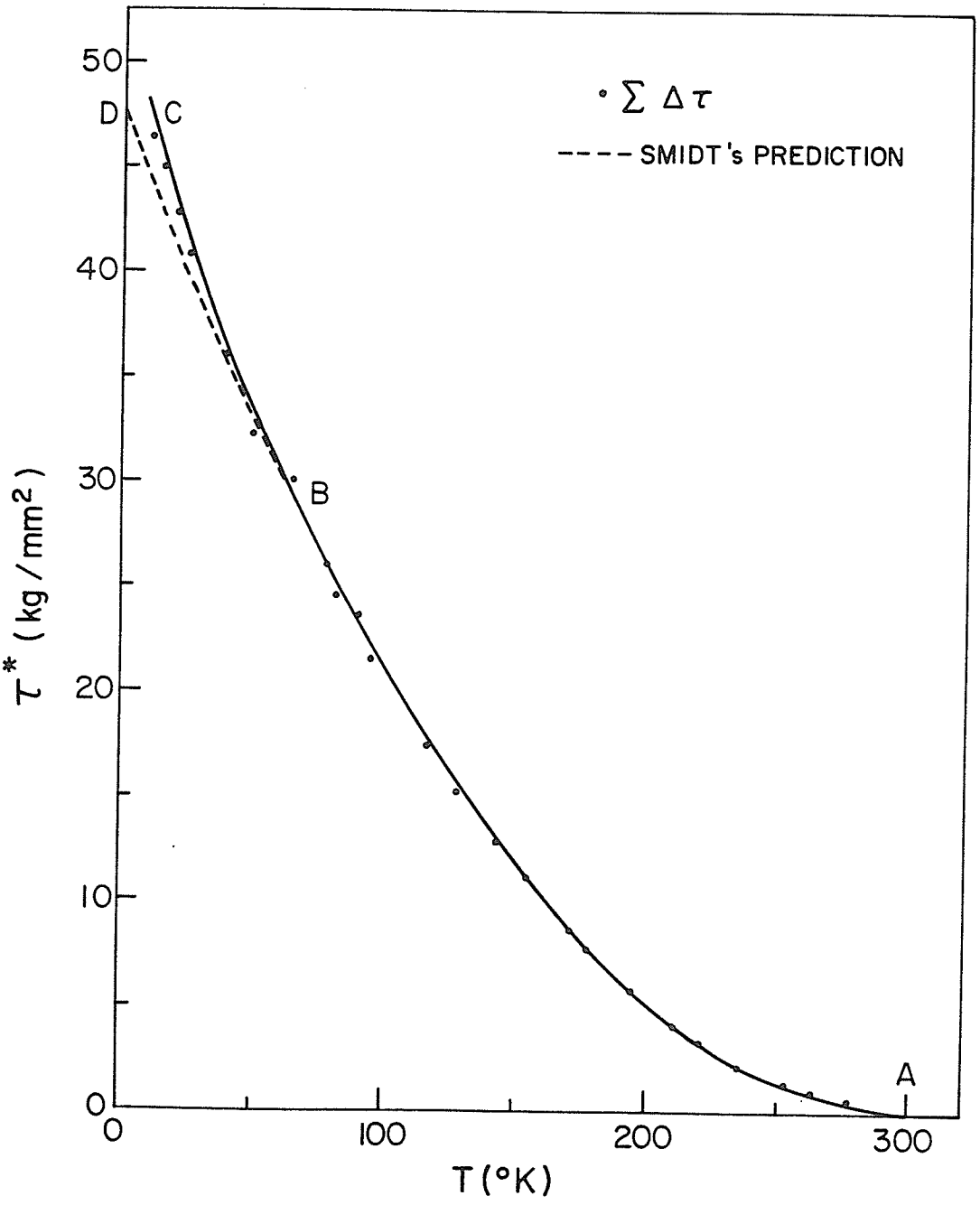

Fig. 4-3 Variation of effective shear stress with temperature in Ferrovac E iron.

Extrapolation of the curve AC in Fig. 4-3 gives the effective stress stress $\tau_0^* = 52.5$ Kg/mm^2 at 0 K , whereas Smidt's linear approximation yields $\tau_0^* = 47.5$ Kg/mm.^{2}

The results of differential strain-rate tests are represented by the activation volume V_a^* which is calculated from Eq. (2-26). The dependence of V_a^* on effective stress is shown in Fig. (4-4) where V_a^* is seen to be within 100b.[3] The apparent activation enthalpies are then calculated from V_a^* and $\partial\tau^*/\partial T$ using Eq. (2-27). The results are shown in Fig. (4-5). A straight line seems to fit the $H_a - T$ data fairly well. The total enthalpy ΔH_0 (ΔH_a at $T = T_c$) required to surmount the barrier is read from Fig. (4-5) as 0.75 eV. This value is in good agreement with those reported in the literature.[53,55] Attempts to compute ΔG, the Gibbs free energy, from the data of Fig. (4-4) and (4-5) via the approaches of Surek, et al.[51] have shown that $\Delta H \simeq \Delta G$.

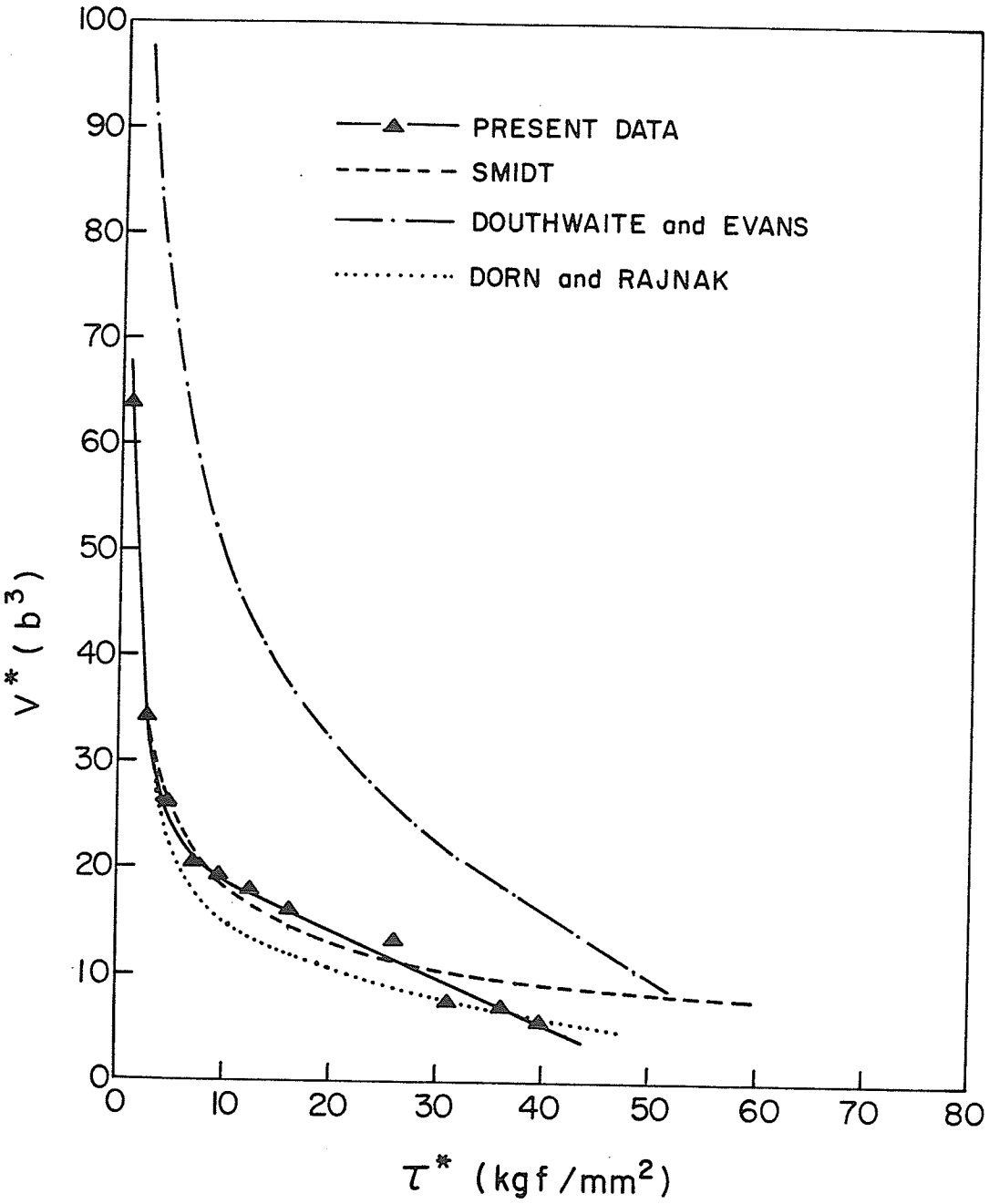

Fig. 4-4 Comparison of experimental and theoretical $V^* - \tau^*$ curves. (▲ Ferrovac E iron).

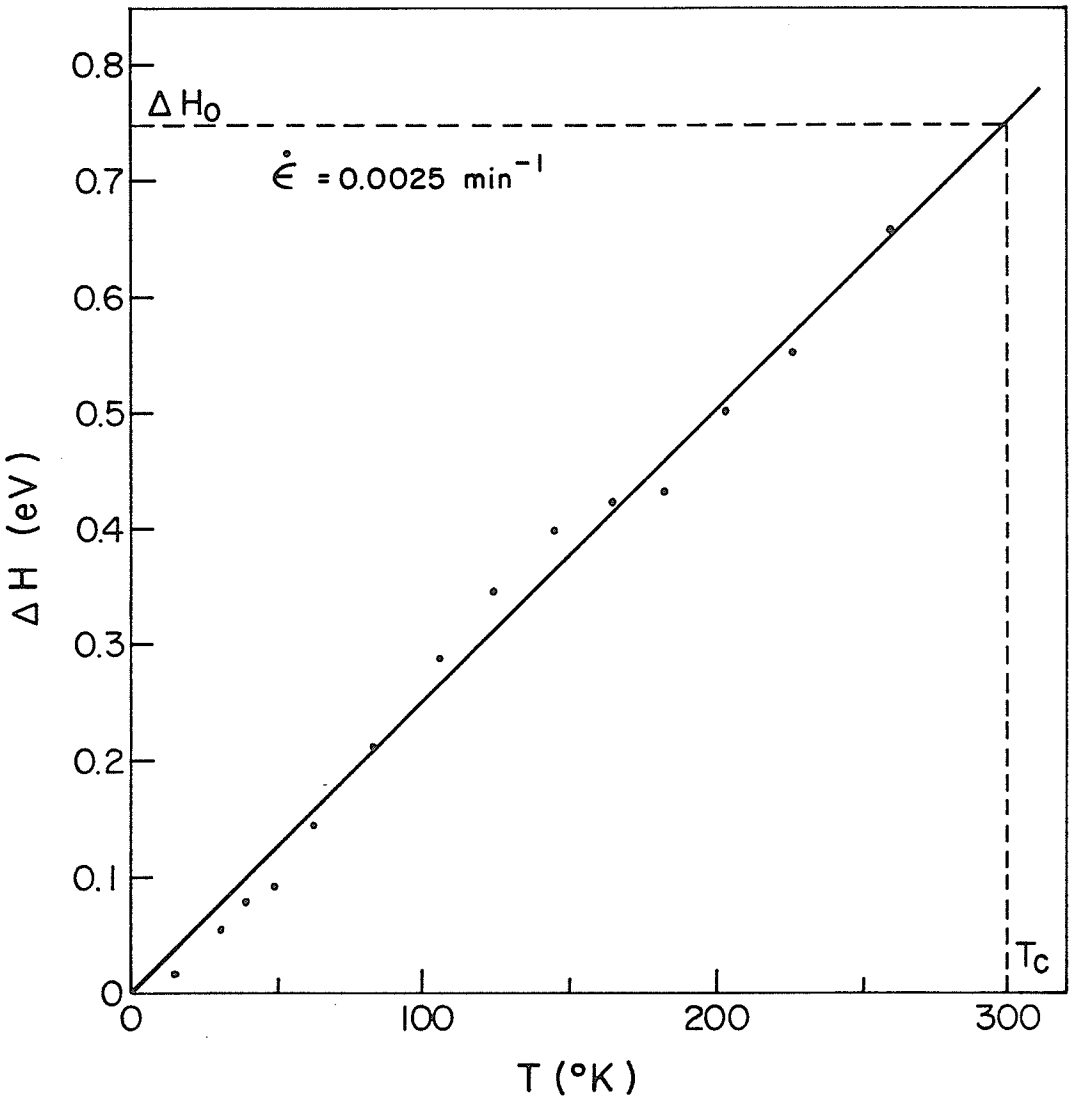

Fig. 4-5 Variation of activation enthalpy with temperature for Ferrovac E iron.

4.1.2 COMPARISON OF FERROVAC E EXPERIMENTAL RESULTS WITH THEORETICAL PREDICTIONS

The objective of testing the Ferrovac E iron is two-fold. Firstly, this material has been commonly used in various laboratories for the study of the deformation behavior of iron. However, the information below 77K has been incomplete. Because the range 0-77K forms a substantial portion of region I in iron, any conclusion regarding the rate-controlling obstacles in region I must take account of the deformation behavior in this temperature range as well. Secondly, this material contains 352 atppm of carbon and nitrogen together, the two strong hardeners for iron. Therefore, the data will be useful for the study of the effects of these interstitial atoms, in particular, the solid solution softening effect in iron.

Smidt[53] suggested a linear relationship between $(\partial\tau^*/\partial T)$ and T given by

$$-\Delta\tau^*/\Delta T = -2AT + B \qquad (4\text{-}1)$$

The activation enthalpy and volume can be derived analytically from equation (4-1).

$$H / H = 1 - \sqrt{\tau^*/\tau_o^*} \qquad (4\text{-}2)$$

$$V^* = \Delta H_o / 2\sqrt{\tau^* \tau_o^*} \qquad (4\text{-}3)$$

where ΔH_0 is the enthalpy at zero effective stress and τ_0^* is the effective stress at zero temperature. Fig. (4-2) shows that Smidt's linear approximation (Eq. (4-1)) is valid between 70 and 300 K. Below 70 K, $-(\Delta\tau^*/\Delta T)$ increases more rapidly with decreasing temperature than predicted by Eq. (4-1). Therefore the long extrapolations used by Smidt to obtain the activation parameters below 70 K or at high stress can lead to erroneous results. It has been mentioned earlier that Smidt underestimates the τ_0^* value. The discrepancy in using Eq. (4-1) below 70 K is again reflected in the V^* versus τ^* plot (Fig. (4-4)) where the curve flattens off at higher stresses in contradiction with the experimental data.

The material used in this investigation contains 230 atppm of carbon and 120 atppm of nitrogen. It is useful to reexamine the effects of the interstitial impurity atoms on the dislocation mobility in the light of the additional data gathered at low temperatures. The two models that have been developed for the low temperature deformation of α-iron and of b.c.c. metals in general are:

1. the lattice hardening model due to Dorn and Rajnak[56] and
2. the solution hardening model of Fleischer.[28]

Dorn and Rajnak consider the nucleation of a stable double kink in a dislocation attempting to cross a Peierls hill as the rate-controlling mechanism. They assume the energy of a dislocation is a periodic function of position, with the same periodicity as the

crystal lattice in the direction perpendicular to the dislocation. The line energy per unit length of dislocation is given by

$$\Gamma(y) = \frac{\Gamma_c+\Gamma_o}{2} + \frac{\Gamma_c-\Gamma_o}{} \left(\frac{\alpha}{2} + \cos\frac{2\pi y}{a} - \frac{\alpha}{2}\cos\frac{4\pi y}{a}\right) \tag{4-4}$$

where Γ_c and Γ_0 are the line energies per unit length of dislocation lying at the top and bottom, respectively, of the Peierls potential. a is the lattice periodicity. The parameter α is introduced to modify the line energy profile. When $\alpha = 0$, $\Gamma(y)$ is purely sinusoidal. The free energy of activation is given by

$$\Delta G = 2\int_{y_o}^{y_c} \left\{\Gamma^2 - \left[\tau^* b\,(y-y_o) + \Gamma(y_o)\right]^2\right\}^{\frac{1}{2}} dy \tag{4-5}$$

where y_0 is the position of the dislocation under the stress τ^* and y_c, the position of the double-kink at the saddle point configuration. $\Delta G - \tau^*$ and $\tau^* - T$ are evaluated numerically from equation (4-5).

The proponents of the solution hardening model, on the other hand, consider the interaction of a glide dislocation with the tetragonal strain field produced by the interstitial impurity atoms. Fleischer[28] has derived a $\tau^* - T$ relationship according to

$$\sqrt{\tau^*/\tau_o^*} = 1 - \sqrt{T/T_c}$$

A comparison of the experimental results with the predictions of the two models is shown in Fig. (4-6).

Limiting our attention to temperatures between 70 and 300 K, it can be seen that the datum points fall on the curve for either model. This is why the earlier investigators could not unambiguously arrive at the rate controlling obstacles in this metal. When the data below 77K are included, it is clear that the operation of Fleischer's model can be ruled out. The Dorn-Rajnak predictions seem to fit the experimental data well with the adjustable parameter $\alpha = -1$ in equation (4-4). However it should be noted that the $\tau^* - T$ relation calculated from Dorn-Rajnak model is sensitive to the line energy profile. The variation of α to render the matching of theoretical and experimental curves does not have a sound physical basis.

Fleischer's original description of the force-distance curve (equation 2-5) for an interstitial obstacle is since known to be only approximate. More rigorous treatments of the problem are now available. It is of interest at this point to see if the present results can be interpreted in terms of the more recent approaches to the solution hardening problem.

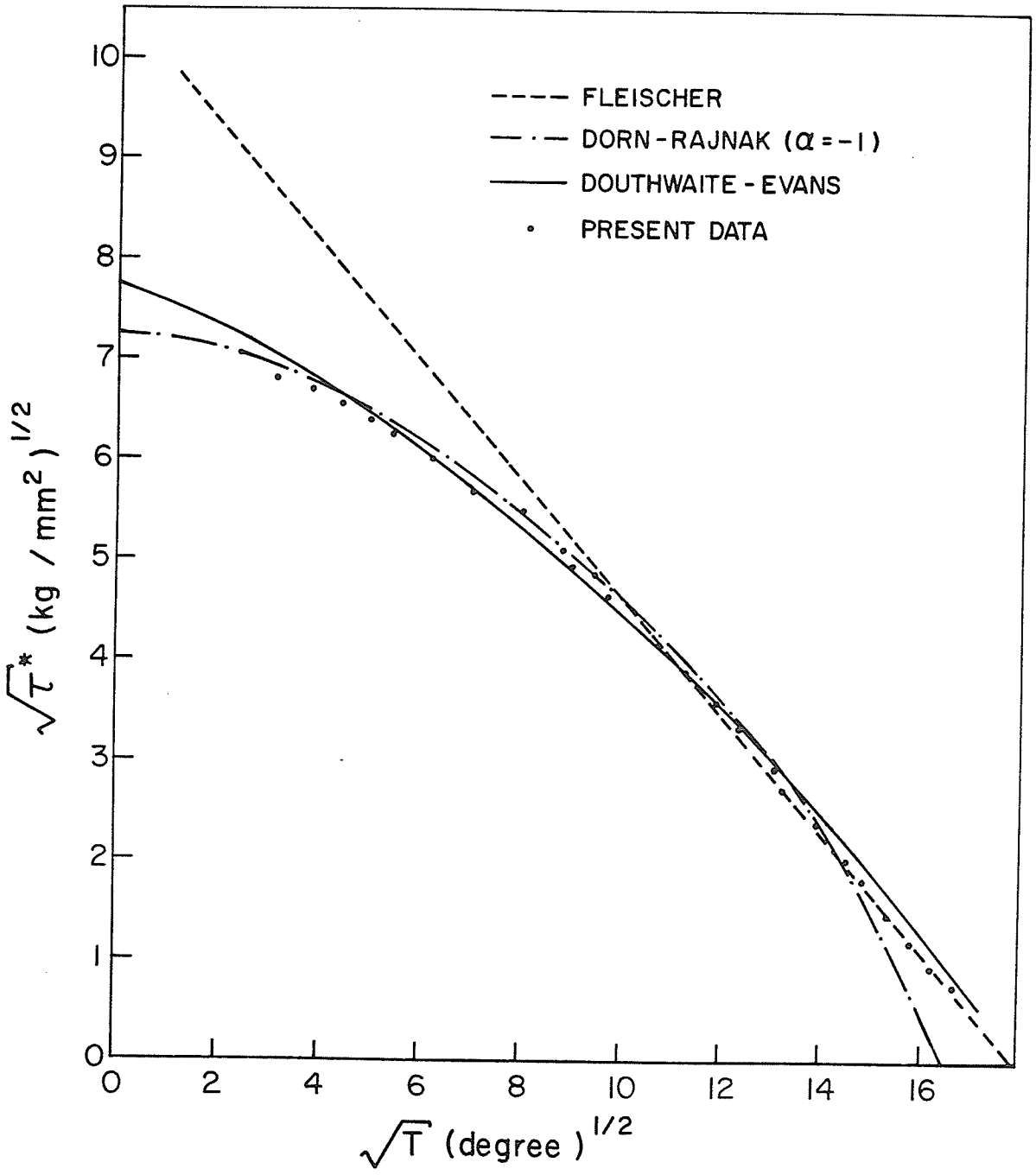

Fig. 4-6 Comparison of τ^*-T curve of Ferrovac E iron with theoretical predictions.

Barnett and Nix[57] have presented solutions to the point defect-dislocation interaction problem. Their solutions have recently been improved by Douthwaite and Evans.[58] They consider the interaction between screw dislocations and the tetragonal strain fields produced by interstitial solute atoms in an anisotropic cubic crystal. The interaction forces depend on the relative configuration of the dislocation line and the tetragonal axis of the strain field. The strongest interaction is between a dislocation lying along [111] direction and the tetragonal axis is either [100] or [010] as shown in Fig. (4-7).

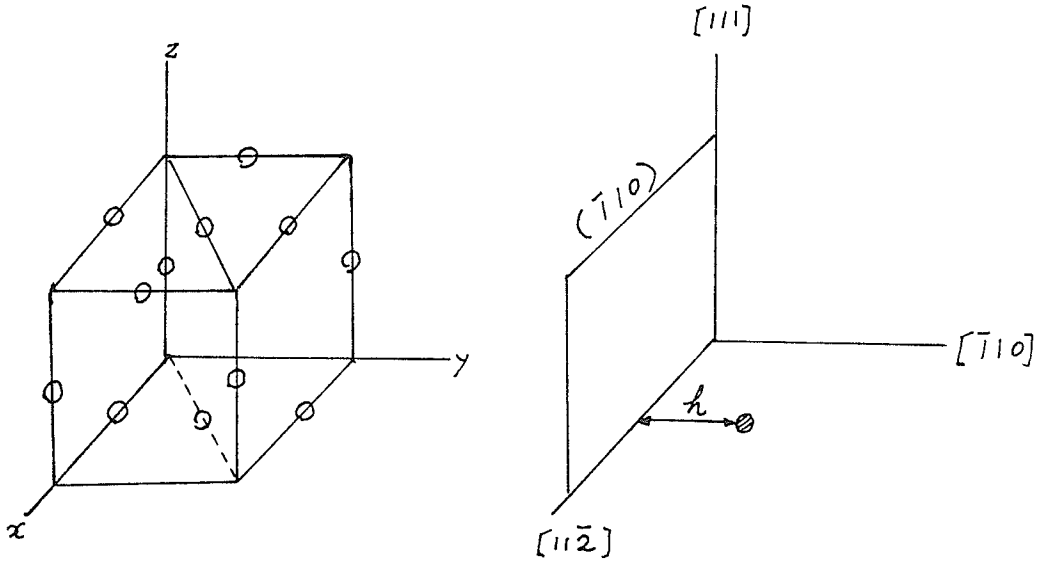

Fig. (4-7) (a) Octahedral interstitial site,

(b) coordinate system

The force on a [111] dislocation is given by[58]

$$F = 2\sqrt{2}\, b\, V\, \varepsilon_T \sin(2\theta + \pi/3) \sin^2 \theta / 6\pi S'_{44} (1-\delta)^{\frac{1}{2}} h^2 \qquad (4\text{-}7)$$

where $V = a^3/2$, $\varrho_T \simeq 0.9$, $h/x = \tan\theta$,

$S'_{44} = S_{44} + \frac{4}{3}(S_{11} - S_{12} - S_{44}/2)$, Sij are stiffness constant and $\delta \simeq 0$

Based on the Douthwaite-Evans force-distance relation, the activation parameters can be calculated numerically as follows. The activation enthalpy is given by

$$\Delta H = \int_{\beta}^{\gamma} (F - \tau^* b\ell)\, dx \tag{4-8}$$

where β and γ are the equilibrium positions and ℓ, the effective barrier spacing, is evaluated from the Friedel relation

$$\ell = (\mu b/N\tau^*)^{1/3} \tag{4-9}$$

Here N is the area density of barrier on the slip plane. Equation (4-8) gives ΔH versus τ^* relationship. By assuming (see Fig. 4-5)

$$\Delta H/\Delta H_o = T/T_c \tag{4-10}$$

the dependence of τ^* on temperature can be obtained from equation (4-8). The results are plotted on Fig.(4-6). It can be seen that the

functional relationship between τ^* and T calculated from Douthwaite-Evans force is in better agreement with the experimental results. However, a good theory should predict all the observed physical phenomena. The activation volume is defined by

$$V^* = b\ell(\gamma - \beta) \qquad (4\text{-}11)$$

V^* can be calculated from Douthwaite-Evans force-distance relationship. The results are plotted in Fig. (4-4). The agreement is less satisfactory when the theoretical and experimental activation volumes are compared.

In conclusion, the present data show that Smidt's linear relation for $(\Delta\tau^*/\Delta T)_\varepsilon$ versus T is not valid below 70 K in Ferrovac E iron. Therefore the linear extrapolation technique used by Smidt to obtain the activation parameters below 70 K is not adequate. Both Fleischer and Douthwaite-Evans solution hardening theories cannot completely describe the experimental results. Therefore, the motion of dislocations in region I in Ferrovac E iron is not solely controlled by the interstitial solute atoms.

4.1.3 HIGH PURITY BATTELLE IRON

There has been a continuous interest in purifying iron crystals in recent years in an attempt to explore the intrinsic mechanical properties of iron.[59] In 1963, Stein and co-workers[60] introduced ZrH_2 purification technique to reduce the concentrations of interstitial impurities below their detection limit (10^{-3} ppm). Since then this technique has been widely used to purify iron. As purer iron crystals become available, one would expect the temperature and strain-rate sensitivity of flow stress to decrease with decreasing impurity content. On the contrary, the present data show that the great sensitiveness of flow stress to temperature and strain-rate at low temperatures still remains in the purer crystals. This indicates a substantial lattice contribution to friction stress. The testing of high-purity Battelle iron serves two purposes : (1) to explore the intrinsic mechanical properties of iron; (2) to shed some light on the role of impurity atoms in controlling the dislocation mobility.

Fig. (4-8) shows the temperature sensitivity of the effective stress for Battelle iron. The salient feature in this plot is that it consists of two approximately linear portions of different slopes connected by a transition region centred at 220 K. The $\partial\tau^*/\partial T$ reproducibility of the results is excellent in the as-received Battelle iron. The temperature sensitivity of the Ferrovac E iron is also plotted in Fig. (4-8) for comparison. It can be seen that

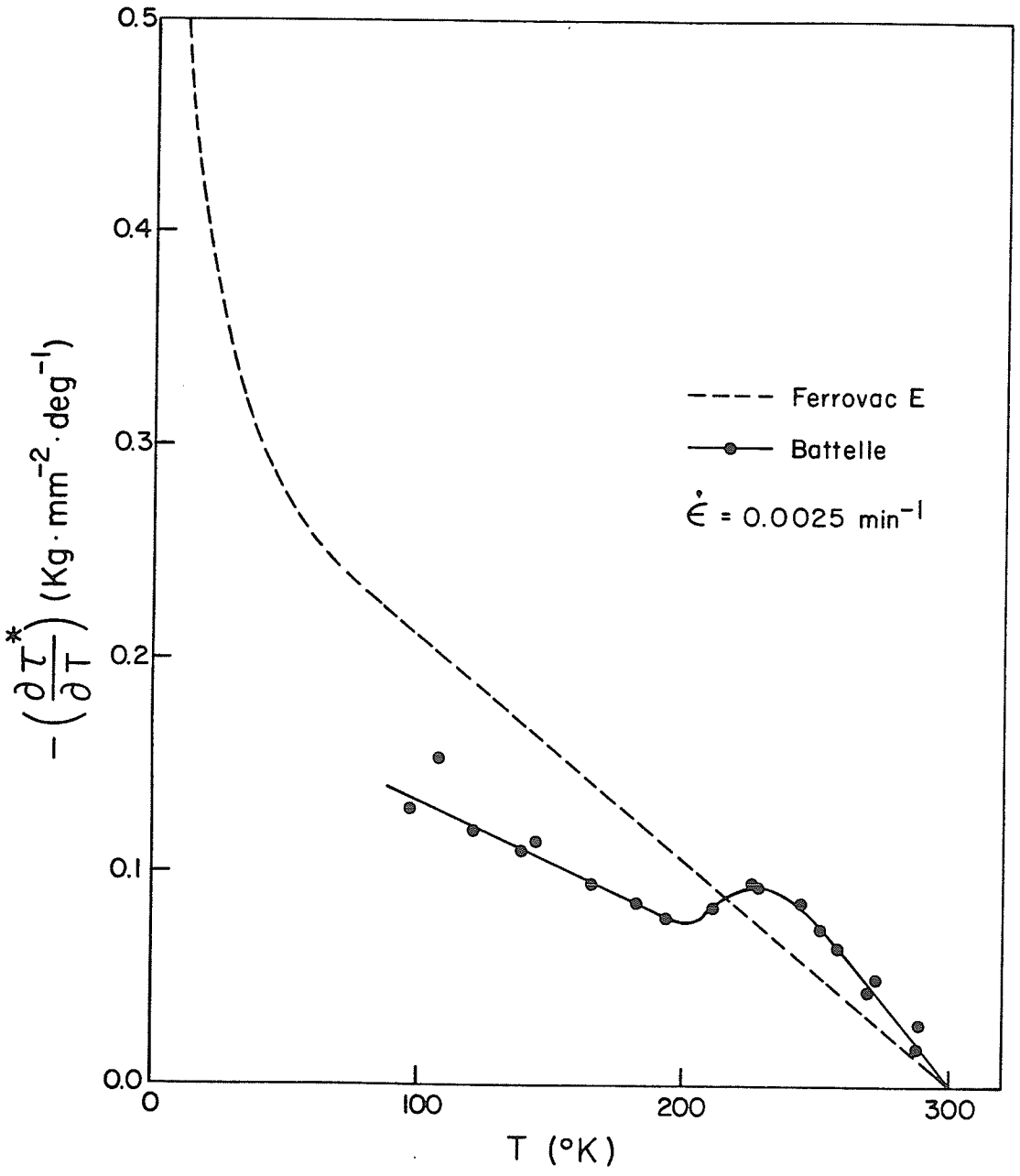

Fig. 4-8 Temperature sensitivity of the effective stress for Battelle iron.

the plot is linear between 70 and 300 K giving the parabolic efffective stress versus temperature relationship commonly observed in less pure iron.[53] Another important feature in Fig. (4-8) is that the temperature sensitivity of flow stress for the Ferrovac E iron is lower than that of the purer Battelle iron between 220 and 300 K. This is closely related to the solid solution softening effect and will be considered in more detail later.

Fig. (4-9) shows the temperature dependence of the effective stress for the Battelle and Ferrovac E irons. This figure displays two important features. (1) There is a concave down region between 180 and 250 K for Battelle iron. It must be emphasized that the concave down region occurs only in the thermal component of the flow stress, i.e., the effective stress, versus temperature plot.[92] (2) Between 180 and 300 K, the effective stress of high purity Battelle iron is greater than that of the less pure Ferrovac E iron. We therefore suggest that the concave down region in high purity iron may be related to the solution softening effect observed in less pure iron.

In the temperature region where deformation is thermally activated, the strain-rate sensitivity (SRS), $\partial\tau^*/\partial\ell n\dot{\varepsilon}$, passes through a maximum at a certain temperature T_s. The SRS for the high purity Battelle and Ferrovac E irons are shown in Fig. (4-10). The magnitude of the SRS maximum decreases with decreasing impurity concentration. It is also of interest to note that T_s increases with decreasing impurity content.

The SRS data transformed into activation volume using Eq. (2-26)

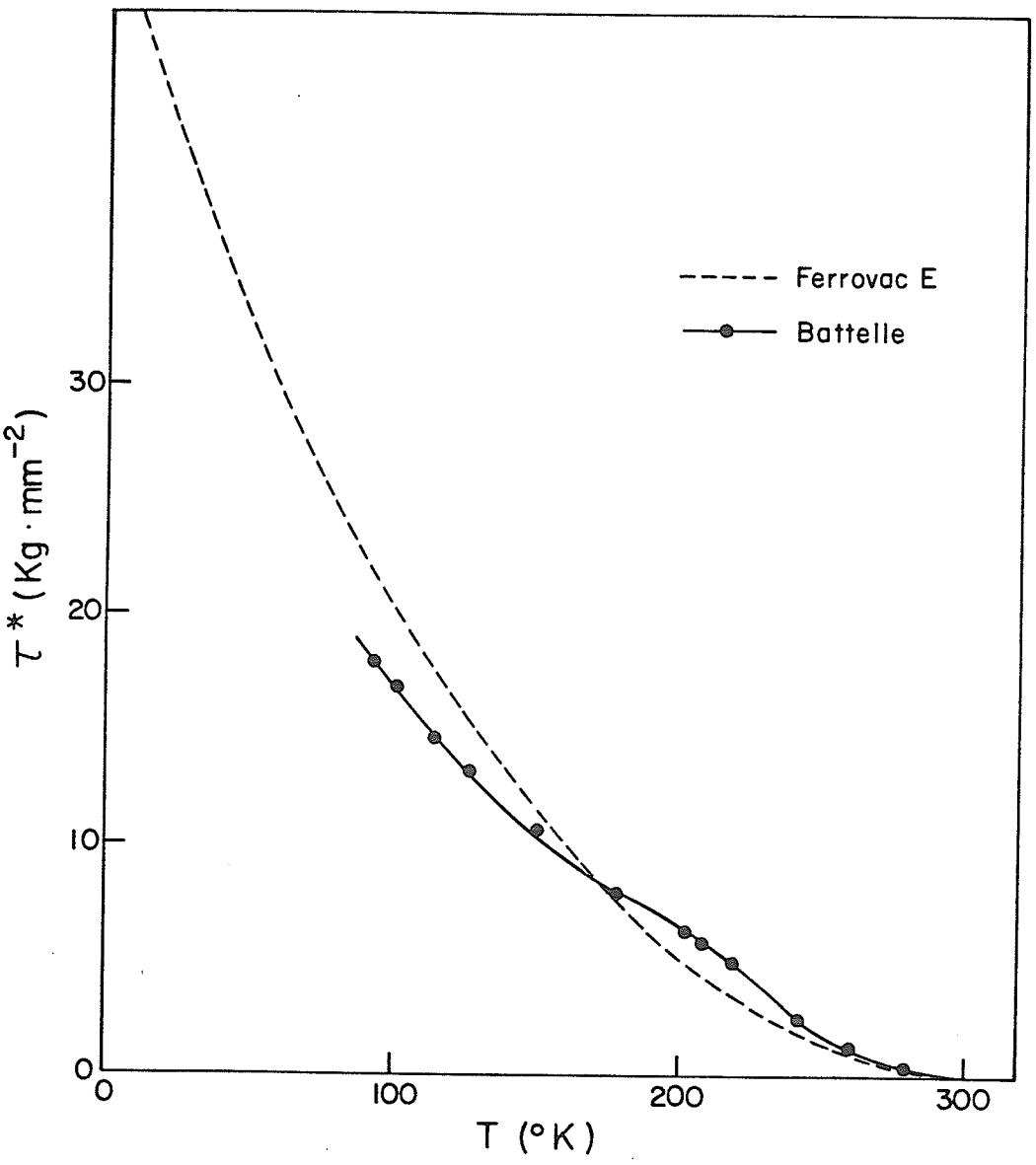

Fig. 4-9 Effective stress as a function of temperature for Battelle iron.

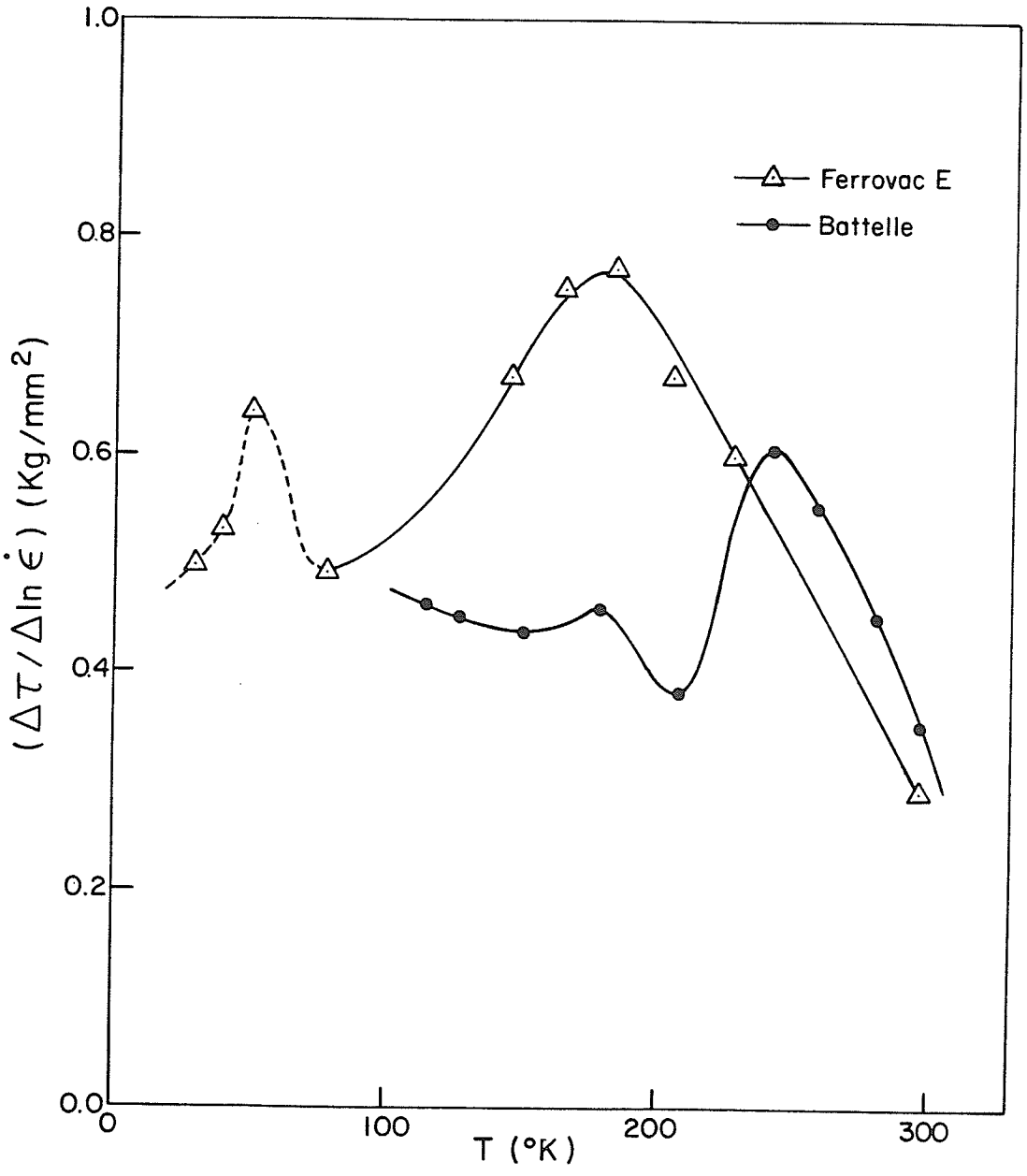

Fig. 4-10 Strain rate sensitivity of flow stress.

are shown in Fig. (4-11). The striking feature here is the local maximum at $\tau^* = 6$ Kg/mm^2 in the high purity Battelle iron. It will be proved in the next section that the local maximum in V^* is directly related to the concave down region in τ^* -- T curve.

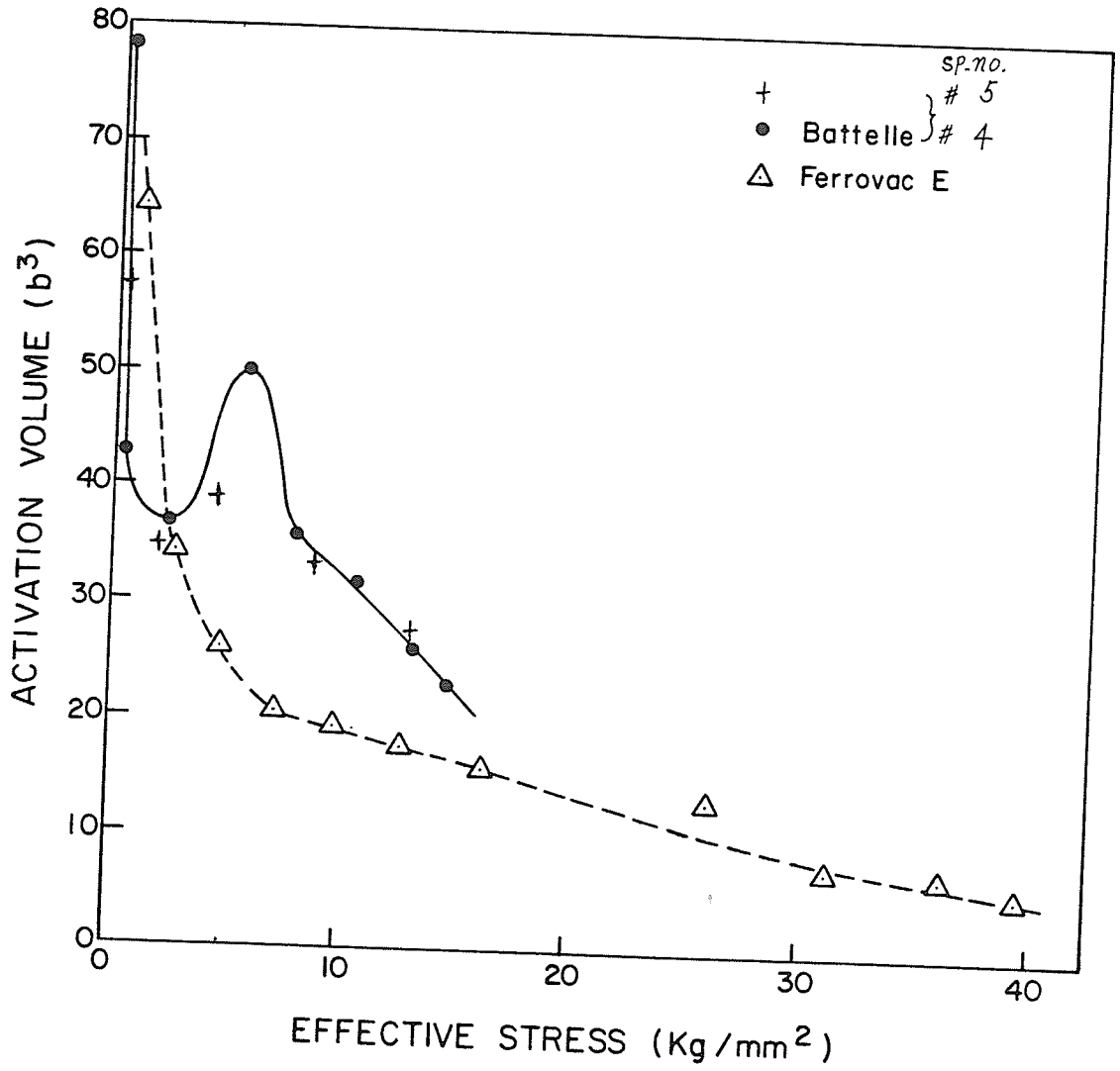

Fig. 4 -11 Activation volume as a function of effective stress.

4.1.4 INTRINSIC VERSUS EXTRINSIC MECHANISMS

For a long time it has been known that the yield stress of b.c.c. metals shows a much stronger dependence on the temperature of deformation than that of f.c.c. metals in the temperature region I. Much of the experimental work in the past was mainly concentrated on b.c.c. transition metals and the strong temperature dependence of yield stress of these metals was widely attributed to interstitial impurities such as carbon, nitrogen and oxygen. These impurities are, indeed, effective hardeners because an interstitial impurity atom occupying an octahedral site of b.c.c. lattice produces a tetragonal strain field which is equivalent to an elastic dipole.[62] The interaction between screw dislocations and tetragonal strain fields forms the basis of the solution hardening theories of Fleischer.[28] Stein, et al.[25] have shown that the critical resolved shear stress and its temperature sensitivity of iron at temperatures below 300 K decrease with decreasing interstitial content. However, the measurement of initial yield stress is complicated by several factors such as the definition of yield point, dislocation source operation, and the exhaustion hardening due to the more mobile edge dislocation. The present work (Fig. 4-9 and 4-10) shows that interstitial impurities indeed contribute to the thermal component of the flow stress of Ferrovac E iron which contains interstitial impurities. However, the characteristic of strong temperature dependence of the effective stress still persists in the high purity Battelle iron. This indicates that this characteristic is intrinsic in nature. We therefore come to a conclusion that the low temperature flow behavior

of iron containing impurities, particularly of interstitial type, is a combined effect of intrinsic and extrinsic mechanisms.

To observe the intrinsic effects of iron at low temperatures, the impurity content must be low. The degree of purity is therefore crucial in this context. Assume that screw dislocations move by thermally activated nucleation of double-kinks (DK) of critical length. The distance between two neighboring impurity atoms, L, must be greater than the critical length of DK. If the impurity atoms are randonly distributed, L can be estimated by $L = b/\sqrt{c}$, where c is the concentration of impurity atoms. The Battelle iron contains about 20 atppm of carbon and nitrogen. The average separation of carbon and nitrogen atoms is about 225 b. Another way of estimating L is to take into consideration the effective interaction distance, r_1, between an impurity atom and the screw dislocation core. Then the average separation in the <111> direction is given by

$$L = b^3 / [\pi (r_1 + r_2)^2 c],$$

where r_2 is the core radius which is approximately equal to 5b. There is some uncertainty in r_1. However, the DK nucleation can be disturbed only when the solute atoms interact strongly with the core of a screw dislocation. For a rough estimate, we take $r_1 = 5b$. Then, L is estimated to be 160 b for carbon and nitrogen. The activated dislocation length, i.e., the length of a double-kink in the saddle-point configuration, can be estimated from Fig. 4-11 to be about 50 b. This is smaller than L by a factor of more than 3. Therefore, the carbon and nitrogen contents of Battelle iron are acceptably good for observing the intrinsic effects. Other solute atoms, which do not

produce as strong strain field as carbon and nitrogen, require much higher concentration to disturb the DK process. Hydrogen is the only solute which remains mobile in the entire region I. The protons can jump from interstice to interstice like an ideal 'lattice gas', owing to their small size and mass. Since iron does not have a strong tendency to form hydride, the chemical interaction between iron and hydrogen must be relatively weak. It has been shown[111] that hydrogen causes softening in iron in the concentration of about 100 atppm. The Battelle iron contains 9 atppm of hydrogen. This concentration is not high enough to disturb significantly the DK process. Therefore, it is quite possible that the concave-down region in τ^* - T curve of the Battelle iron is an intrinsic effect.

A number of authors[56,65] assume that the strong temperature dependence of flow stress of b.c.c. metals is due to large Peierls barriers. Screw dislocations overcome Peierls potential hill via nucleation of kink pairs. It has been shown in the Section 2.1.4 that the results derived from this type of theories are sensitive to the shape of Peierls potential. One can always adjust the parameters which define the Peierls potential so that the predictions of the theory will match the experimental results. This has been demonstrated in Fig. (4-6). Therefore, this type of models is entirely phenomenological. The physical basis that b.c.c. metals have large Peierls barrier was originally suggested by Hirsch.[33] He pointed out that the phenomena associated with large Peierls barrier in b.c.c. metals had a common crystallographic origin and were related to the three-fold symmetry of screw dislocation axes <111>.

It has been mentioned in Section 2.1.4 that Hirsch's suggestion has been confirmed by the atomistic calculations. Since the displacement field of a screw dislocation core has three-fold symmetry, the core structure must undergo a major modification before the dislocation can glide. Hence a high Peierls barrier is expected. A theory of dislocation dynamics based on three-fold symmetry of screw dislocation core has not been fully developed so far. Instead of core structure having three-fold symmetry, Foxall, et al.[34] suggested that a screw dislocations split on one of the {110} planes and on one of the {112} planes. The quantitative analysis based on this core model has been done by Duesbery.[35] We will compare the predictions of this theory with the experimental results. It is shown in Fig. (4-9) that τ^* versus T curve of high purity Battelle iron has a concave down region between 180 and 250 K. This, in fact, is inherent in Duesbery's theoretical τ^* - T curve, but it was considered as an odd case. The change of curvature from concave downward to upward at 180K in τ^* - T curve has a significant effect on the activation volume. This can be proved below. Substituting the experimental activation enthalpy,

$\Delta H = -TV^* (\partial\tau^* / \partial T)$, into the rate equation, we obtain

$$k\ell n (\dot{\varepsilon} / \dot{\varepsilon}_o) = V^* (\partial\tau^*/\partial T)_{\dot{\varepsilon}} \qquad (4\text{-}9)$$

Differentiate Eq. (4-9) at constant strain rate gives

$$\left(\frac{\partial^2 \tau^*}{\partial T^2}\right)_{\dot{\varepsilon}} = \frac{-1}{V^*}\left(\frac{\partial \tau^*}{\partial T}\right)^2_{\dot{\varepsilon}} \left(\frac{\partial V^*}{\partial \tau^*}\right) \qquad (4\text{-}10)$$

In the concave down region of the τ^* - T curve, $(\partial^2\tau^*/\partial T^2) < 0$. Eq. (4-10) implies that $(\partial V^*/\partial \tau^*) > 0$, i.e., V^* increases with increasing τ^*. This is shown in Fig. (4-11) as a local maximum which is not observed in less pure iron. We can now conclude that the concave down region in the τ^* - T curve and the local maximum in the $V^* - \tau^*$ curve are a manifestation of a single material property. The concave down region in τ^* vs T curve can not be ascribed to dihydrogen hardening, as proposed by Quesnel, et al.,[37] because a similar behavior has also been observed by Diehl, et al.[70] in their outgassed iron. It has been mentioned earlier that Duesbery's model based on the dissociation of screw dislocation on {110} and {112} planes predicts these two charcteristics of pure iron. Therfore, it is quite convincing that the concave down region in τ^* vs. T curve is an intrinsic property of pure iron. As such, any meaningful explanation of the effect of impurities must start with a suitable model which can account for this intrinsic property of pure iron.

Fig. (4-9) shows that the impurity atoms cause softening between 180^o and 300^o K and hardening below 180^o K. The scavenging mechanism proposed by Ravi and Gibala[27] is inadequate to explain these experimental results for the following reasons : The scavenging model is based on the solution hardening concept and softening is proposed to arise due to the clustering of solute atoms under suitable

conditions, such as the presence of an element with strong chemical affinity towards the residual impurity atoms. This mechanism, however, predicts softening throughout the temperature range of our investigation. Furthermore, the lower limit of the effective stress in a scavenged material must be the effective stress of the ideally pure material. The experimental observation that, in the temperature range 180-300 K, τ^* for the lower purity Ferrovac E iron falls below the very high purity Battelle iron suggests that a logical approach to softening must start by considering the effect of impurity atoms on the intrinsic mechanism reponsible for τ^* of pure iron. Two theories, which follow this line of thought, have been proposed by Sato and Meshii[40] and Wuthrich and Frank.[41] Sato and Meshii consider the motion of undissociated screw dislocations in the combined stress fields of Peierls-Nabarro and misfit strain centers. They assume that a size misfit defect produces a torque on a screw dislocation and thus assists the nucleation of double-kinks. The results of their calculation show that hardening occurs at higher temperatures and softening at lower temperatures. This again is inconsistent with our experimental observations. It has been mentioned earlier that Duesbery's calculation based on the dissociated screw dislocation model predicts a τ^* versus T curve of the correct nature for high purity iron. This model assumes that a screw dislocation in the low-energy sessile form is extended partly on one of the {110} planes and partly on one of the {112} planes. A segment of this dislocation can glide only when it is constricted into a planar form on the slip plane. The saddle point configuration depends on the magnitude of the

applied stress. The concave down region in the τ^* versus T curve occurs at intermediate stresses. The activation process in this stress range is the formation of double-kinks of critical length. The critical length is determined by the condition that the decrease in the energy of the dislocation due to re-extension out of the slip plane is equal to the constriction energy. It may be concluded that, in this stress or temperature range, the solute atoms interfere with the operation of this mechanism. Following a similar kind of reasoning, Wuthrich and Frank have predicted the hardening and softening characteristics which are in qualitative agreement with our experimental results. They have pointed out that the effect of solute atoms on the motion of extended screw dislocation will depend on the concentration and the magnitude of applied stress in the following manner :

(a) Whenever $\ell < L$, solute atoms cause hardening. Here L is the average separation between neighboring solute atoms at sessile screw dislocations and ℓ , the length of a double-kink in the saddle point configuration in an impurity free metal, as has been described in Section 4.2.2. L is usually determined by the Friedel's relation, equation (4-6). Under the action of applied stress, the nucleation of glissile loops will take place and grow up to the length L. In other words, solute atoms serve to reduce the free length of dislocations. In the limiting case $\ell \ll L$, the sessile-glissile transformation is essentially unaffected by the presence of impurity atoms. As such, the motion of screw dislocations is controlled by the intrinsic mechanism. However, when ℓ becomes comparable to L, the

sessile-glissile transformation of screw dislocations and the subsequent nucleation of double-kinks are not rate-controlling. The saddle point configuration is reached only when the kinks are depinned from the impurity atoms. In this case, solute atoms cause hardening. At low temperatures (i.e., high stresses) where ℓ is smaller than or comparable to L, a condition applicable for all practical levels of impurity in iron ($\leq 10^{-4}$ for carbon), solution hardening is to be expected.

(b) When $\ell > L$, the activation process can be visualized as the recombination of the extended dislocation over a length L simultaneously with the depinning of a partial dislocation from an impurity site. Therefore, the recombination and pinning energies are the major contributions to the activation energy. The physical reason for the occurrence of solution softening given by Wuthrich and Frank is that the recombination energy is proportional to L and therefore the activation energy decreases with increasing impurity concentration. At lower stresses (i.e., high temperatures) ℓ becomes large and the conditon $\ell > L$ can be satisfied for relatively low concentrations of solute ($< 10^{-3}$ for carbon). The results of their calculation are shown in Fig. 4- 12. This is in qualitative agreement with our experimental observation of softening between 180 and 300 K.

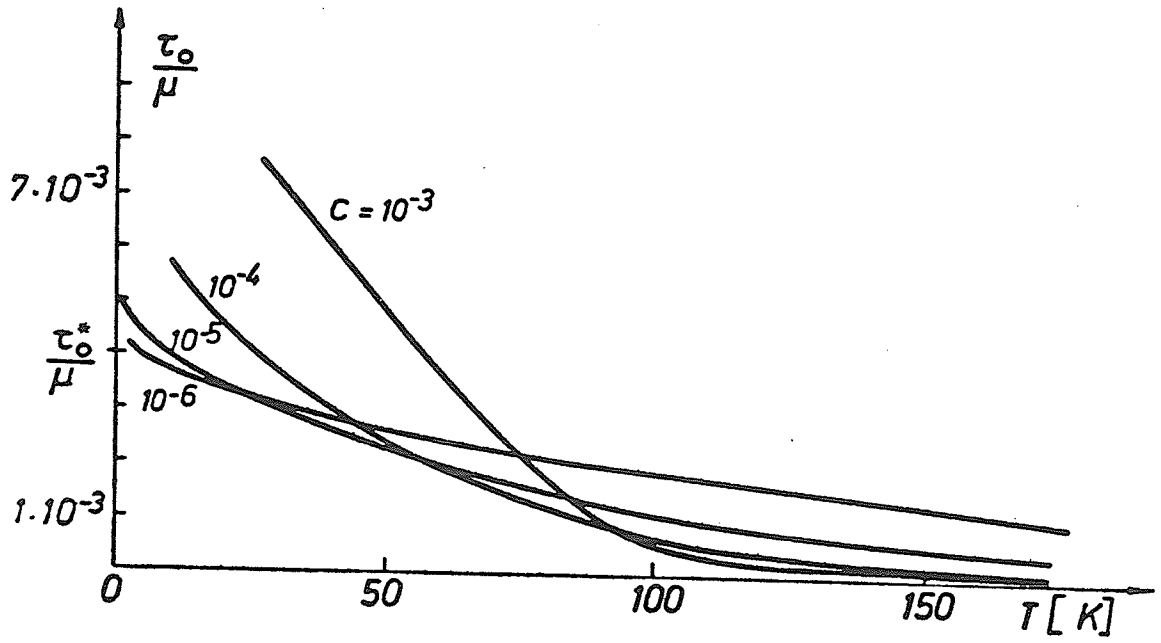

Fig. 4-12 Effect of impurity concentration on τ^*-T curve predicted by Wuthrich and Frank.[41]

The concept discussed above can be extended to explain the variation in the critical concentration, C_m, which causes maximum softening from element to element. As this concentration is exceeded, softening is replaced by hardening. Leslie[36] has shown that C_m is inversely proportioned to the effectiveness of the solute as a strengthening agent. For the mechanism (b) to operate, the following conditon must be satisfied,

$$\gamma L w \geq \Delta E \qquad (4\text{-}11)$$

where γ is the stacking fault energy, w, the width of dissociation, and ΔE is the interaction energy between a partial dislocation and an impurity atom. For interstitial solutes such as carbon and nitrogen which produce tetragonal distortion, ΔE is large. As such, for equation (4-11) to hold, L must be large which requires that C_m be small. This is borne out by the experimental observations that for carbon in iron, C_m is 185 atomic ppm[40], whereas for most substitutional solute atoms for which ΔE is relatively small, C_m is of the order of a few atomic per cent.[36]

In conclusion, the theories of Duesbery[35] and Wuthrich and Frank[41] predict the low temperature deformation behavior of iron in qualitative agreement with our experimental results. Both theories must contain the essential physical aspect, that is, the nonplanar core structure of screw dislocations in b.c.c. metals. However, recent atomistic calculations[23,24] show that the core structure of screw dislocation in b.c.c. lattice has three-fold symmetry instead of the simple dissociation on {110} and {112} planes used in the theories of Duesbery and Wuthrich and Frank. Furthermore, as the

approximate width of stacking fault is only one to two Burgers vectors, the quantitative analysis in terms of partial dislocation becomes suspect. In view of the above, it is felt that both theories require further refinement.

The results of atomistic calculations[23,24,95] indicate that the extension of a screw dislocation core occurs only on the three zone planes of {110} type. Based on this model, the energy to form a stable double-kink should include (1) the energy required to reverse the polarity, including the compressional and dilatational constrictions, (2) the energy to form a pair of kinks, and (3) the energy to separate the two kinks. When kinks move along the dislocation line, they will encounter the secondary Peierls stress. (Here we tentatively distinguish the secondary Peierls stress from the primary one which a screw dislocation experiences when it moves in the direction perpendicular to its axis.) The deformation behavior of iron in region I can be explained qualitatively if we assume that kink nucleation and migration are interdependent processes, i.e., one must occur after the other. In such events, the slower process is rate-controlling.

Fig. (4-13) shows the activation enthalpy as a function of effective stress for the Battelle and Ferrovac E irons. It can be seen that the reduction in activation energy by impurity atoms occurs in the region of low stresses (i.e., for $T > 180$ K). At high stresses, the addition of solutes increases the activation energy.

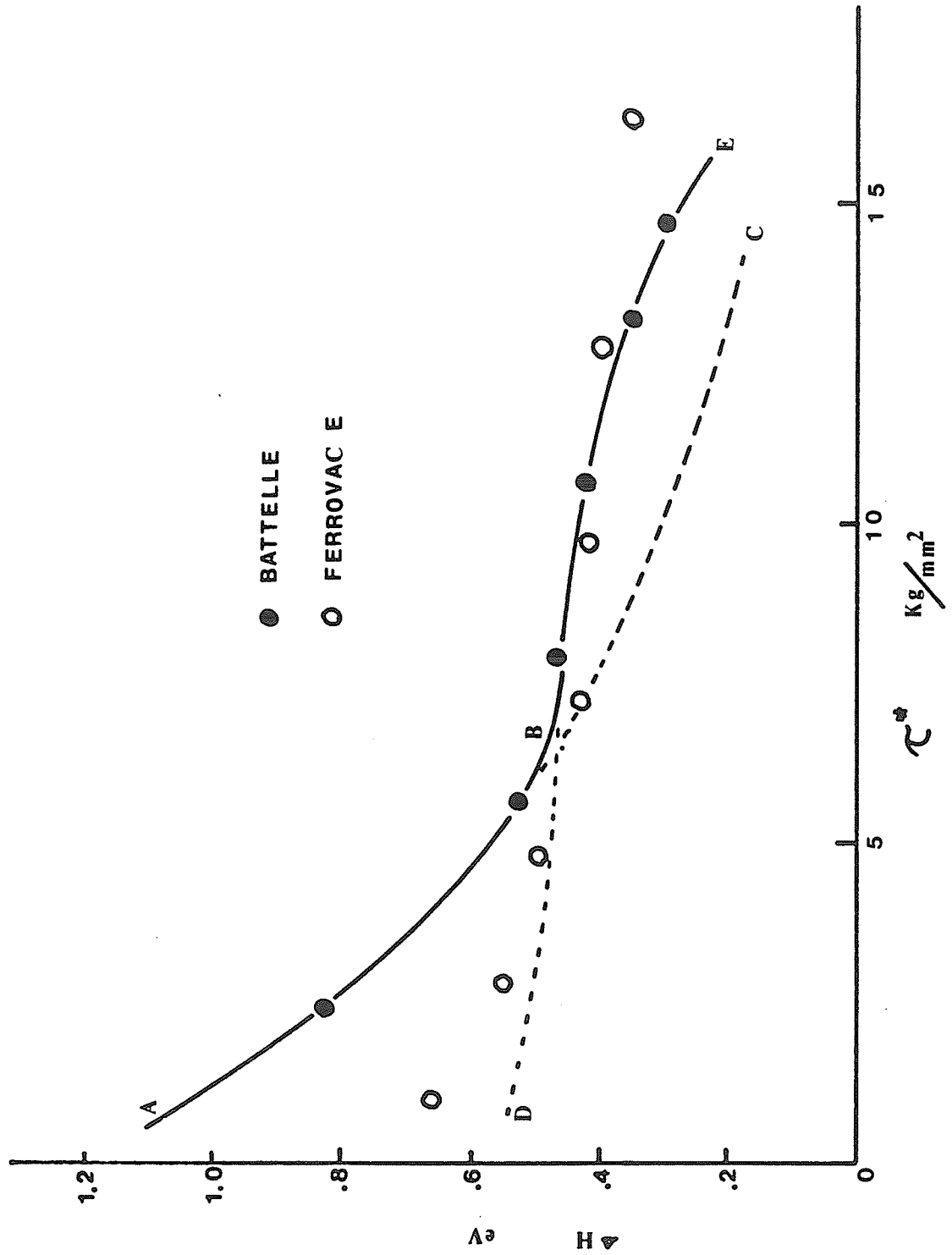

Fig. 4-13 The activation enthalpy in region I as a function of effective stress.

It has been argued at the beginning of this section that the behavior observed in the Battelle iron is possibly free from the extrinsic effects. Then, based on the data shown in Fig. (4-13) for the Battelle iron, we propose that curve ABC represents the variation of activation energy with stress for the nucleation of double-kinks and curve DBE for the migration of kinks. At low stresses, the strain rate is controlled by the nucleation of stable double-kinks, because the activation enthalpy for nucleation is greater than that for migration. It is well-known that the size misfit strain produced by solute atoms assists the nucleation of double-kinks and resists the motion of kinks.[40,94,112] Therefore, solution softening occurs at low stresses (i.e., higher temperatures in region I) and hardening at high stresses. The transient (Fig. 4-8) observed in the Battelle iron occurs at the mechanism change (i.e., near point B in Fig. 4-13).

The above model cannot be used to explain the softening due to substitutional solute atoms because concentrations up to a few atomic percents are required to cause softening. The strain field produced by solute atoms would overlap at such high concentrations. This warrants a separate investigation.

In summary, a simple model, which is based on double-kink nucleation at low stresses and kink migration at high stresses, seems to explain the deformation behavior of iron in region I. Reliable data on kink nucleation and migration as functions of stress have not been reported in the literature. More work in this area is apparently needed.

4.2 PLASTIC FLOW AT INTERMEDIATE AND HIGH TEMPERATURES (REGION II AND III) IN FEERROVAC E IRON

The three-fold symmetry of screw dislocation core in b.c.c. lattice and the subsequent sessile-glissile transformation form the basis of dislocation dynamics in α-iron at low temperatures. However, at 300 K (0.17 Tm) and above, these rate-controlling obstacles at low temperatures become "transparent" because there are enough thermal fluctuations in the crystal to assist the overcoming of these obstacles. Therefore, at intermediate temperatures, the applied stress is equal to the internal stress extrapolated from the low temperature region, Fig. (1-1).

In the case of Ferrovac E iron, the region II is not a plateau or an athermal region, as can be seen in Fig. (4-14) because this region is masked by the effect of dynamic strain-ageing due to residual carbon and nitrogen. The positive temperature sensitivity of flow stress between 50 and 200 C (Fig. 4-14) is a manifestation of the ageing effect. In the following sections, we will try to identify the possible deformation mechanisms in the region III.

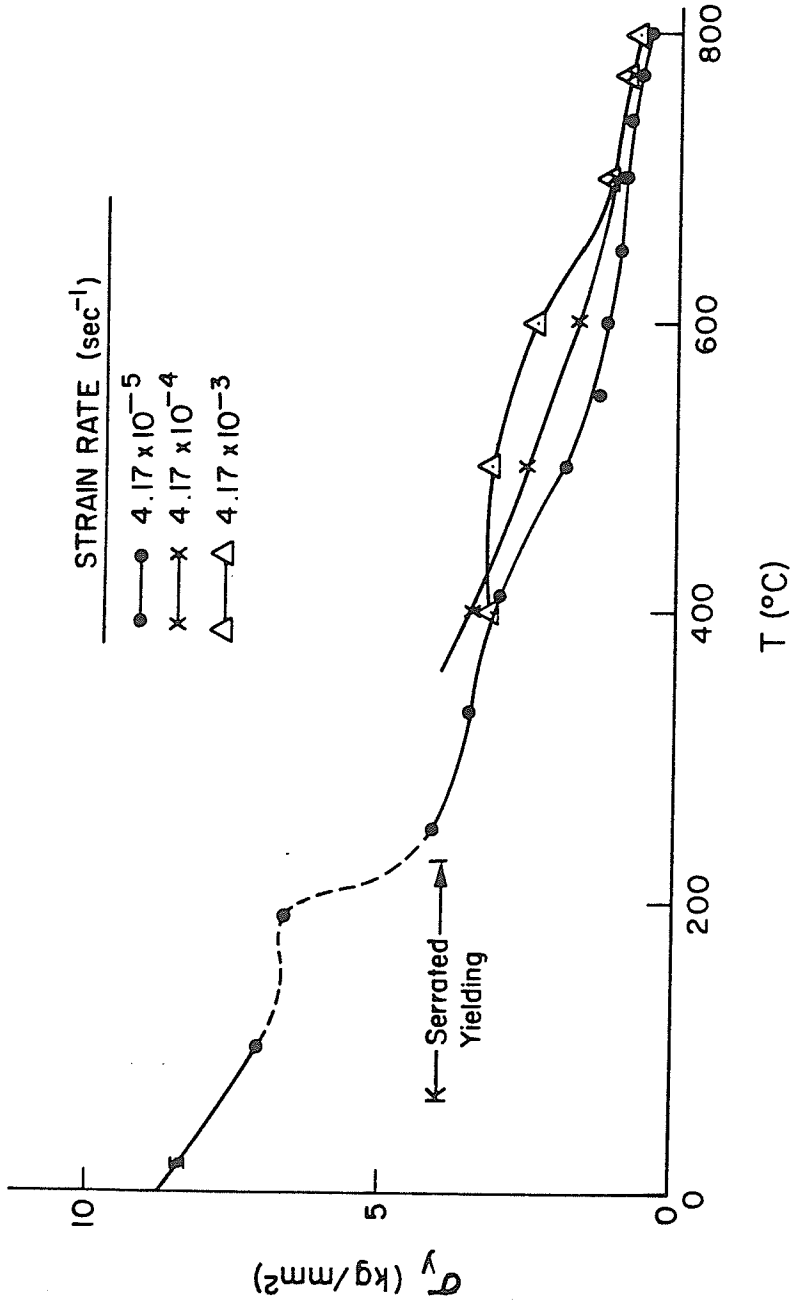

Fig. 4-14 Yield stress of Ferrovac E iron in region II and III.

4.2.1 REGION III - THE THERMALLY ACTIVATED FLOW OF FERROVAC E IRON AT HIGH TEMPERATURES.

As has been mentioned earlier, there is no sharp transition from region II to III and region III can extend into region II as strain increases. We have essentially two thermally activated deformation regions (I and III) in α-iron. In this section, the results of initial yield and steady-state flow behavior of Ferrovac E iron between 673 and 1073 K will be presented and discussed. Below 673 K, not only the effect of impurity is present, it is also difficult to establish the steady-state flow before the on-set of tensile instability.

Fig. (4-15) shows the temperature dependence of the 0.1% off set yield stress and the steady-state flow stress for the three different strain rates. It is quite clear that the temperature sensitivity of the steady-state flow stress is much higher than that of the yield stress. The steady-state flow stress drops sharply between 400 and 500 C (673 -773 K) followed by a wavy curve between 500 and 800 C (773-1073 K). The wavy curve follows the same pattern for the three strain rates. Therefore, it is a material property. The yield stress does not follow the same pattern of change as steady-state flow-stress. The yield stress decreases gradually with increasing temperature between 400 and 700 C. Above 700 C, it becomes less temperature sensitive.

The plots of yield stress and steady-state flow stress versus strain rate are shown in Fig. (4-16) and (4-17). The strain-rate can be represented approximately by a power law of yield stress, τ^n

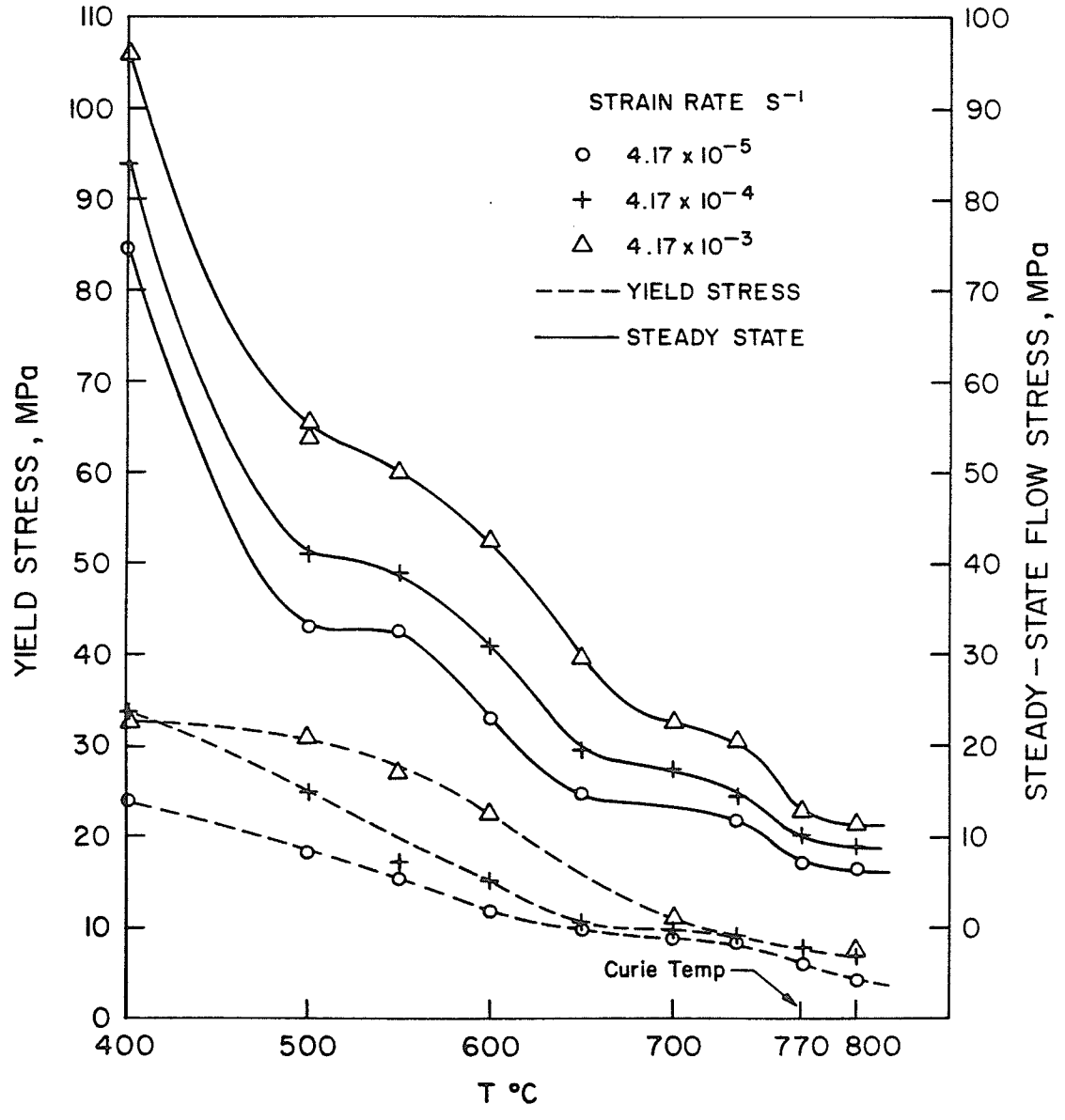

Fig. 4-15 Yield and steady-state flow stresses at three different strain rates in region III.

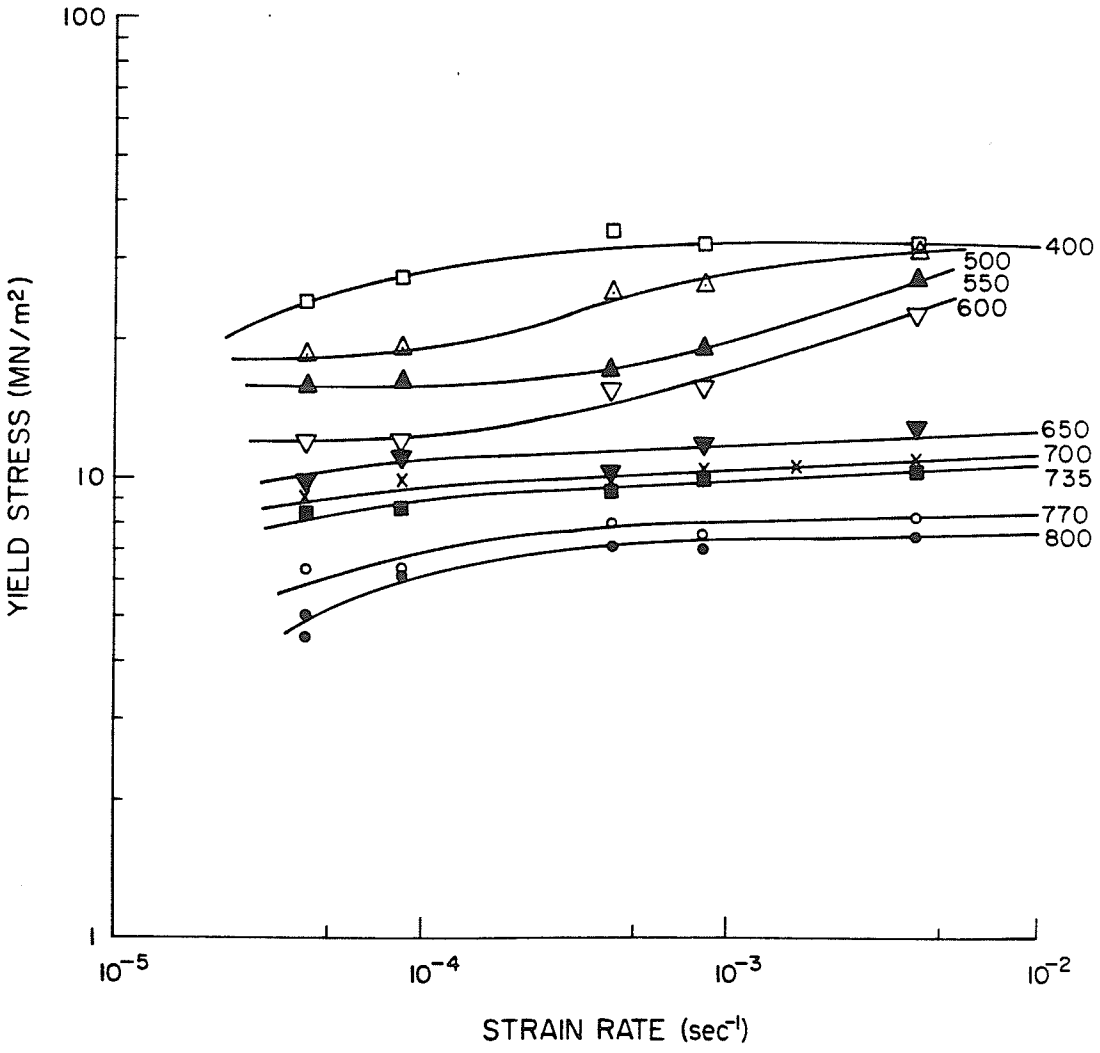

Fig. 4-16 Yield stress versus strain rate plots.

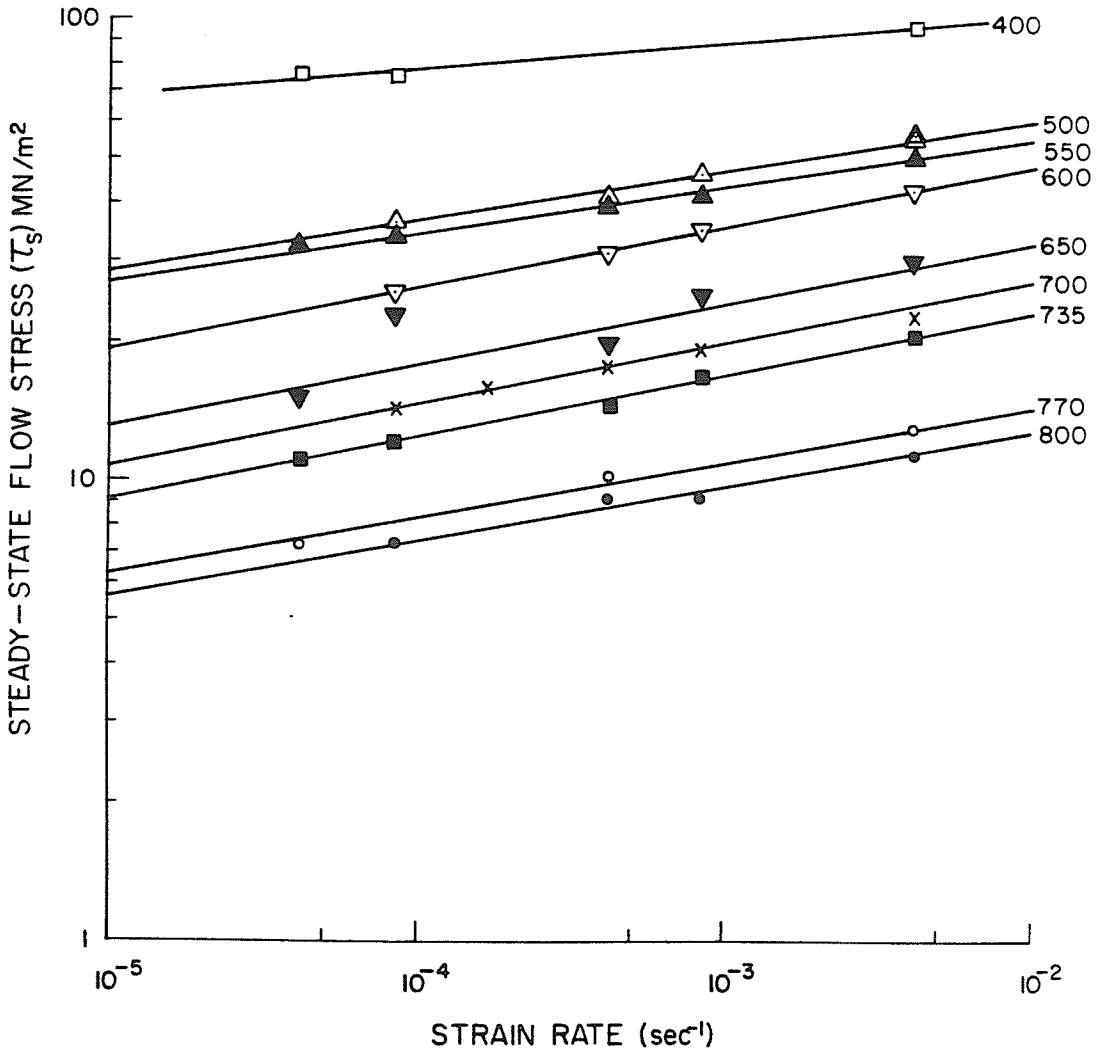

Fig. 4 -17 Steady-state flow stress versus strain rate plots.

($18 < n < 36$), between 650 and 800 C and in the strain rate range of 10^{-4} - 5×10^{-3} sec^{-1} (may be also valid at T > 800 C and $\dot{\varepsilon} > 5\times10^{-3}$ sec^{-1} which are not investigated). Outside the above temperature and strain rate ranges, the strain rate sensitivity of yield stress varies with strain rate. A much higher strain rate sensitivity occurs between 500 and 600 C for $C > 10^{-4}$ In sharp contrast to the yield stress, the strain rate sensitivity of the steady-state flow stress is not affected significantly at various temperatures and strain rates. The steady-state strain rate can be represented by $\dot{\varepsilon} \alpha \tau_s^n$ ($n = 8 \pm 1$). This n value is rather high for iron compared with 4.5 for other metals. However this n value is in fair agreement with the value of 6.7 obtained from creep tests by Ishida, et al..[69]

The activation volumes are evaluated from strain-rate-change tests both at initial yield and at steady-state according to

$$V_a^* = kT \left(\partial \ell n \dot{\varepsilon} / \partial \tau^*\right)_T . \qquad (4\text{-}12)$$

The results are shown in Fig. (4-18). Within the experimental scatter, all the datum points seem to indicate a smooth $V_a^* - \tau$ curve. This suggests that the same mechanism may control the rate of flow at initial yield and at steady-state. The internal stresses are difficult to measure at elevated temperatures. They are assumed to be negligible relative to the effective stresses at yielding.[10] However,

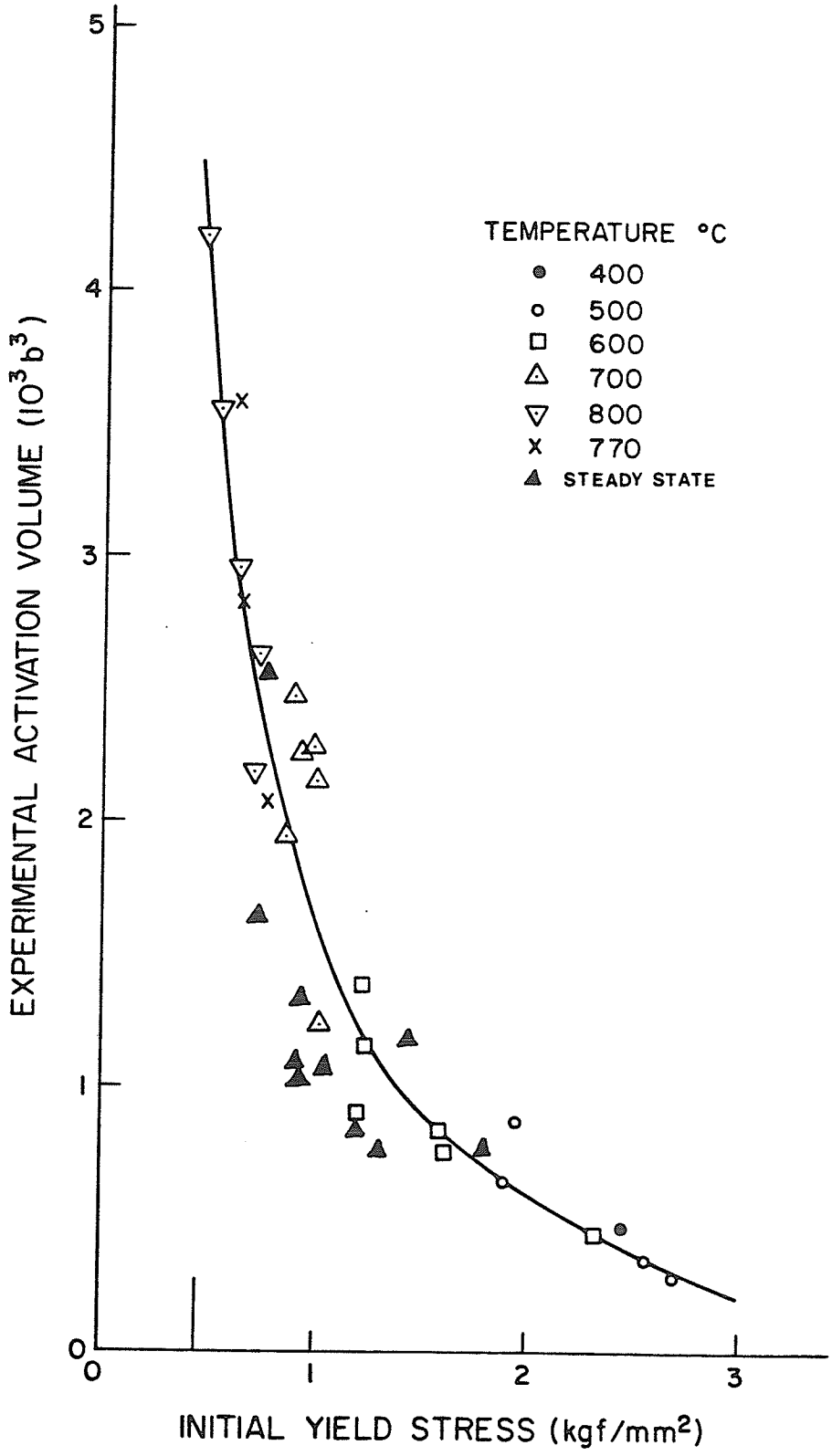

Fig. 4 -18 Activation volume versus stress plots in region III.

the internal stress at steady-state flow is not known with any certainty. Ideally, the activation volumes should be plotted against the effective stress. The plot in Fig. (4-18) will shift the curve along the stress axis because of the inclusion of internal stress component. The activation volume varies approximately in the range of 200 to 4000 b^3 which is an order of magnitude larger than that in the region I.

The strain rate versus 1/T relations at a constant stress can be obtained from Fig. (4-19) and (4-20). These curves are used to evaluate the experimental activation enthalpies,

$$\Delta H_a = -k \left[\partial \ell n \dot{\varepsilon} / \partial (1/T)\right]_{\tau^*} \qquad (4\text{-}13)$$

The results are shown in Fig. (4-21). Below 0.48 Tm. the activation enthalpy based on yield stress is insensitive to temperature and stress, and $\Delta H \approx \frac{1}{2} Q_{SD}$. The activation enthalpy based on steady-state flow stress is also less than Q_{SD} and insensitive to stress for T < 0.48 Tm, but it increases with increasing temperature.

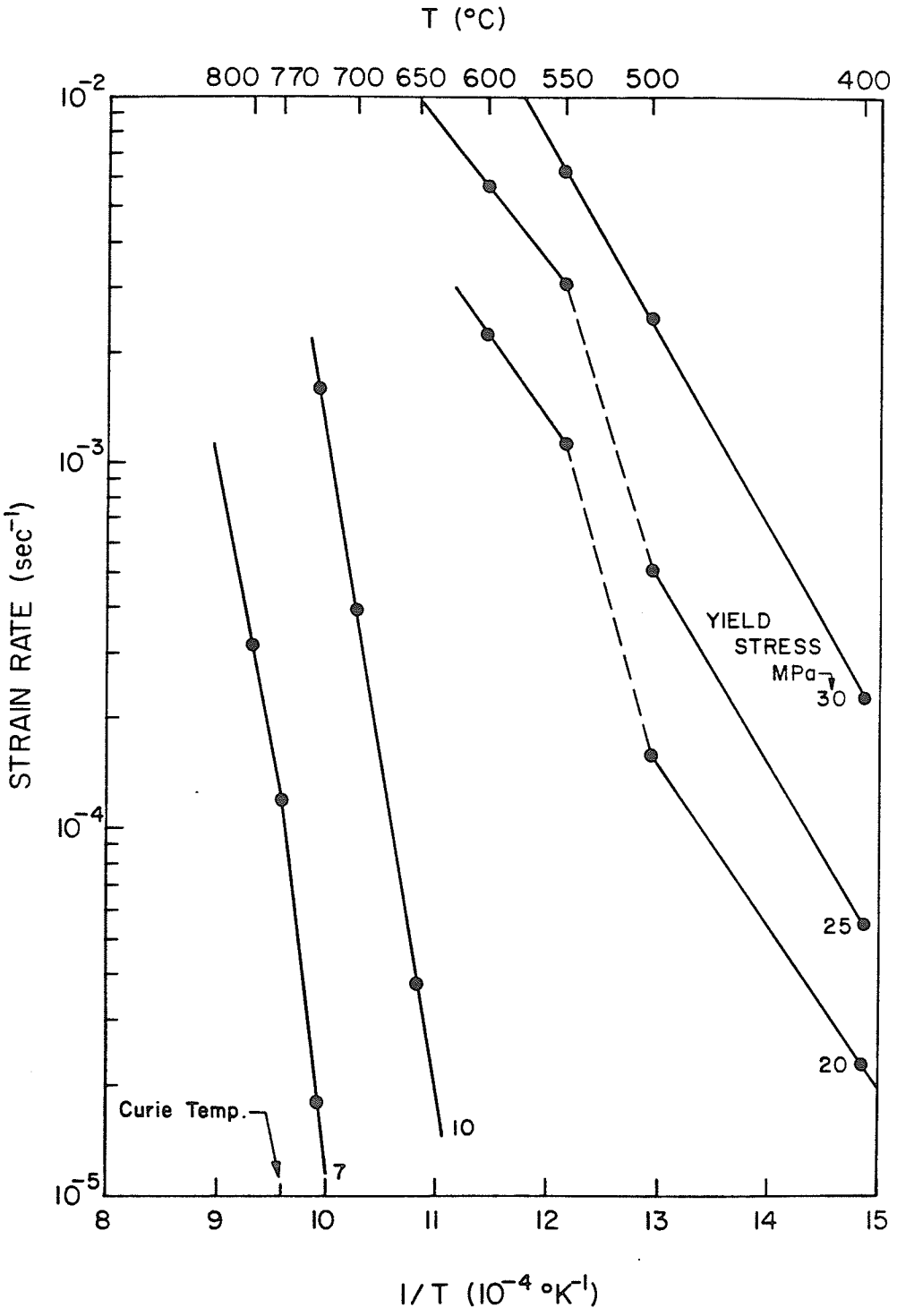

Fig. 4-19 $\dot{\epsilon}$ -T plot for constant yield stress.

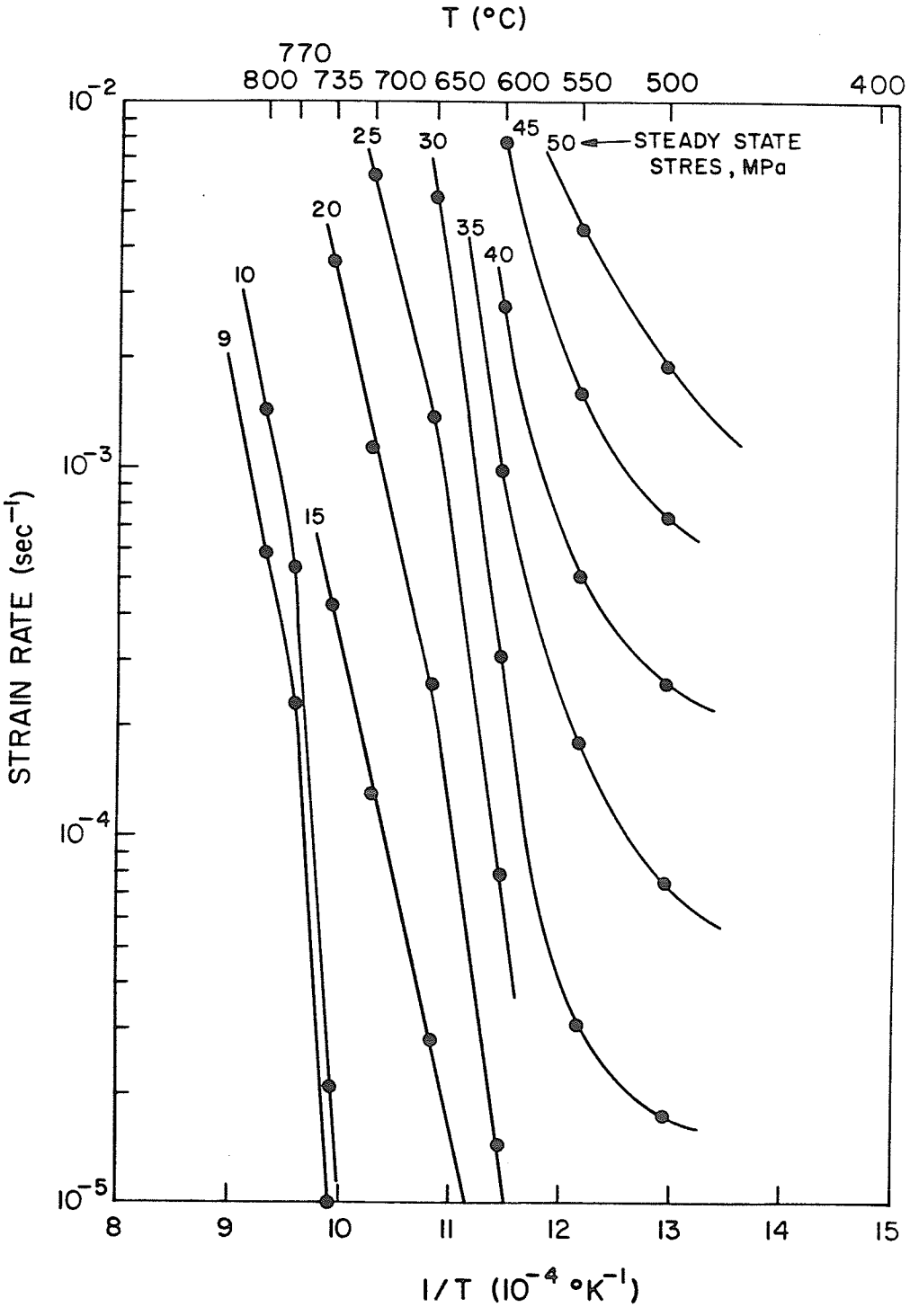

Fig. 4-20 $\dot{\epsilon}$ -T plot for constant steady-state flow stress.

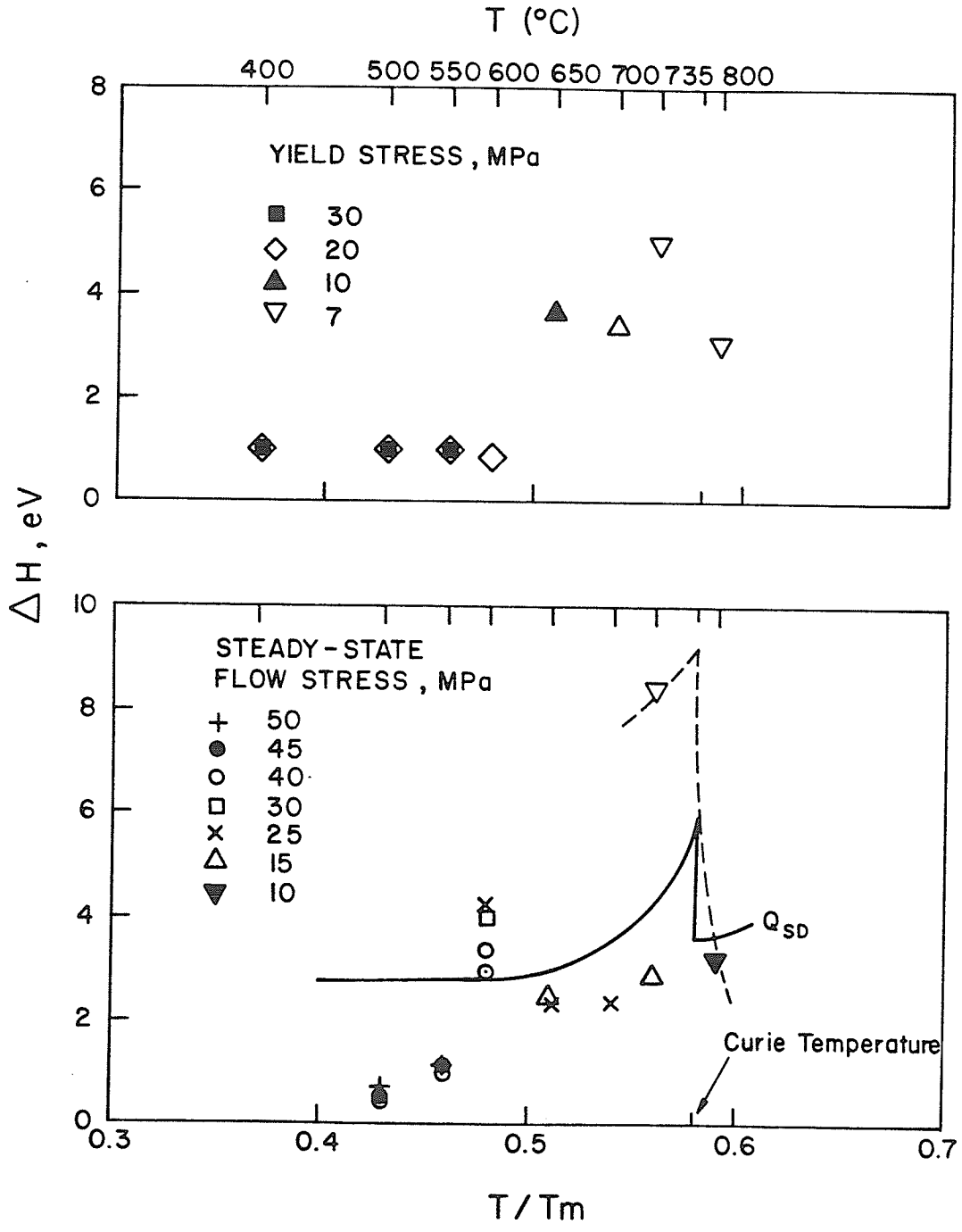

Fig. 4-21 Activation energies at constant yield and steady-state flow stresses

Above 0.48 Tm, the activation enthalpies both at yielding and at steady-state flow seem to approach Q_{SD} . These observations are consistent with the creep activation energies for several b.c.c. and f.c.c. metals compiled recently by Evans and Knowles.[76] That is, below 0.5 Tm, the creep activation energies are in the range of 0.55 to 0.8 Q_{SD} . As the temperature increases beyond 0.5 Tm, the creep activation energy approaches the self-diffusion energy. H undergoes a discontinuity in iron at Curie temperature (770 C) arising from the discontinuity of $d\mu/dT$, Fig. (4-22). The present data are not sufficient to clearly established this abrupt change in H at Curie temperature.

The experimental activation enthalpies are $\Delta H \approx Q_{SD}/2$ for $T < 0.48$ Tm and $\Delta H \simeq Q_{SD}$ for $T > 0.48$ Tm. This feature is also commonly observed in high temperature creep tests. Therefore, the most plausible mechanism in region III is diffusion controlled dislocation motion. We will discuss more detailed mechanism in the following two sections.

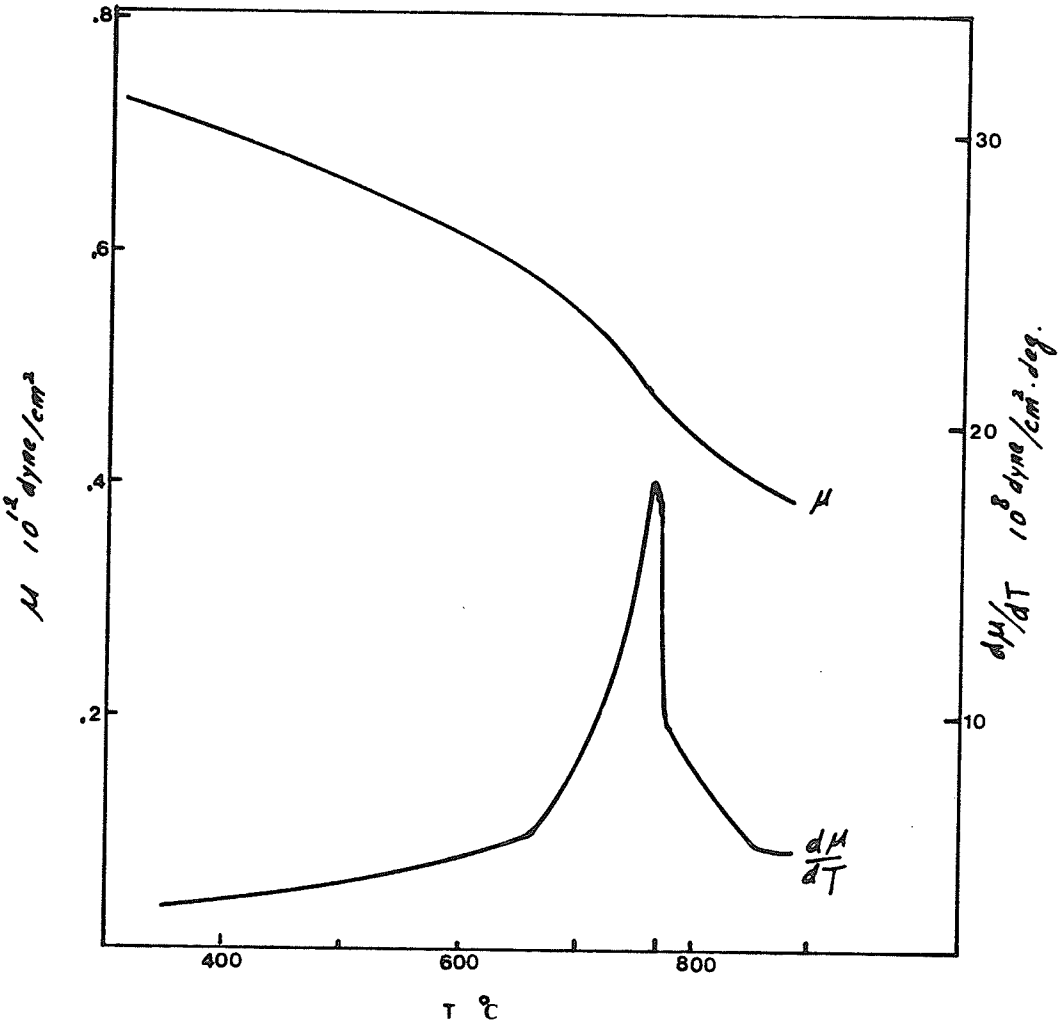

Fig. 4-22 μ - T plot after Denver.[77]

4.2.2 DEFORMATION MECHANISM IN REGION III.

The deformation in region III is, in general, characterized by a steady-state flow for pure metals in the stress range $10^{-5} < \sigma/\mu < 10^{-3}$. During steady-state flow, each grain in a pure poylycrystalline metal is polygonized into subgrains having constant misorientation.[44] This indicates that the number of dislocations in a subboundary also reaches a steady-state. The objective of this section is to develop a dislocation model for the steady-state flow which is based on experimentally observed microstructure, that is the formation of subgrains. The subgrain size has been found to be a function of stress only, regardless of the history of the specimen.[44] In this model, the mobile dislocations are assumed to be released from the subgrain wall and to make a fast glide in the subgrain before they are arrested by subgrain wall again. The work-hardening and recovery (i.e., the recovery creep concept of Bailey-Orowan) will probably take place in the subboundaries in which the density of dislocations is an order of magnitude higher than that in the subgrain. However the strain is mainly produced by dislocation glide in the subgrain.

If each grain is viewed as a composite of metal and subboundary network, the flow stress may be approximated by the rule of mixtures

$$\sigma = f_b \sigma_b + f_g \sigma_g \qquad (4\text{-}14)$$

where f_b and f_g are the volume fractions of subboundary and subgrain, respectively. σ_g is the strength of the subgrain. The shear strength of a subboundary, σ_b , is given by

$$\sigma_b \simeq \mu b/\ell \tag{4-15}$$

where ℓ is the average link length of dislocations in the subboundary. Assuming cubic subgrains, the volume fraction of subboundary is given by

$$f_b = 6wL_s^2 / L_s^3 = 6w / L_s \tag{4-16}$$

where L_s is the subgrain size, and w, the width of the subgrain wall. Then the increase in strength due to subboundary wall is given by

$$\sigma - f_g\sigma_g = f_b\sigma_b = 6\mu bw/(\ell L_s) \tag{4-17}$$

Since stress is proportional to the square root of the dislocation density, σ_b is greater than σ_g by a factor of at least 3. Equation (4-17) states that the flow stress is inversely proportional to the subgrain size. This is consistent with experimental observations.[44]

We will now consider the mechanisms of the release of dislocations from the subboundary network in more detail. It is assumed that a dislocation will be released when a node in the network is broken. Two mechanisms of climb controlled node breaking will be considered.

(1) In b.c.c. metals, the dislocation network is composed of a/2<111> and a<100> types of link dislocations, as have been discussed in Chapter 2. The junction dislocations of a<100> type are

sessile. A link dislocation such as AP in Fig. 4-23b can climb and annihilate with a neighboring link dislocation, resulting in an imbalance in the network. Therefore a link dislocation longer than the critical length, $\mu b/\sigma$, may be created.

(2) The two segments AP and A'Q in Fig. 4-23c can bow out under applied stress, but the stress is not sufficient to expand the loop into a semicircle A dipole is formed at DD'. Annihilation of the dipole by climb frees the dislocation segment AA' from the attractive junction PQ.

The above two mechanisms are quite similar. The rate controlling process in both mechanisms is the climb controlled annihilation of dipoles. The basic driving force for climb is the mutual attraction between the dipole dislocations. However, the probability of forming a dipole in mechanism (1) is not known with any certainty. The operation of mechanism (2) would be a more frequent event. This also provides a self-consistent view of all the dislocation mechanisms operating in the three temperature regions. As has been discussed earlier, the athermal bowing of mobile loops between attractive forest dislocations is the major cause of internal stress in region I and II. In region III, the maximum bowing stress (i.e., the stress required to expand a dislocation loop into a semicircle) is not required because of the operation of the mechanism (2) stated above.

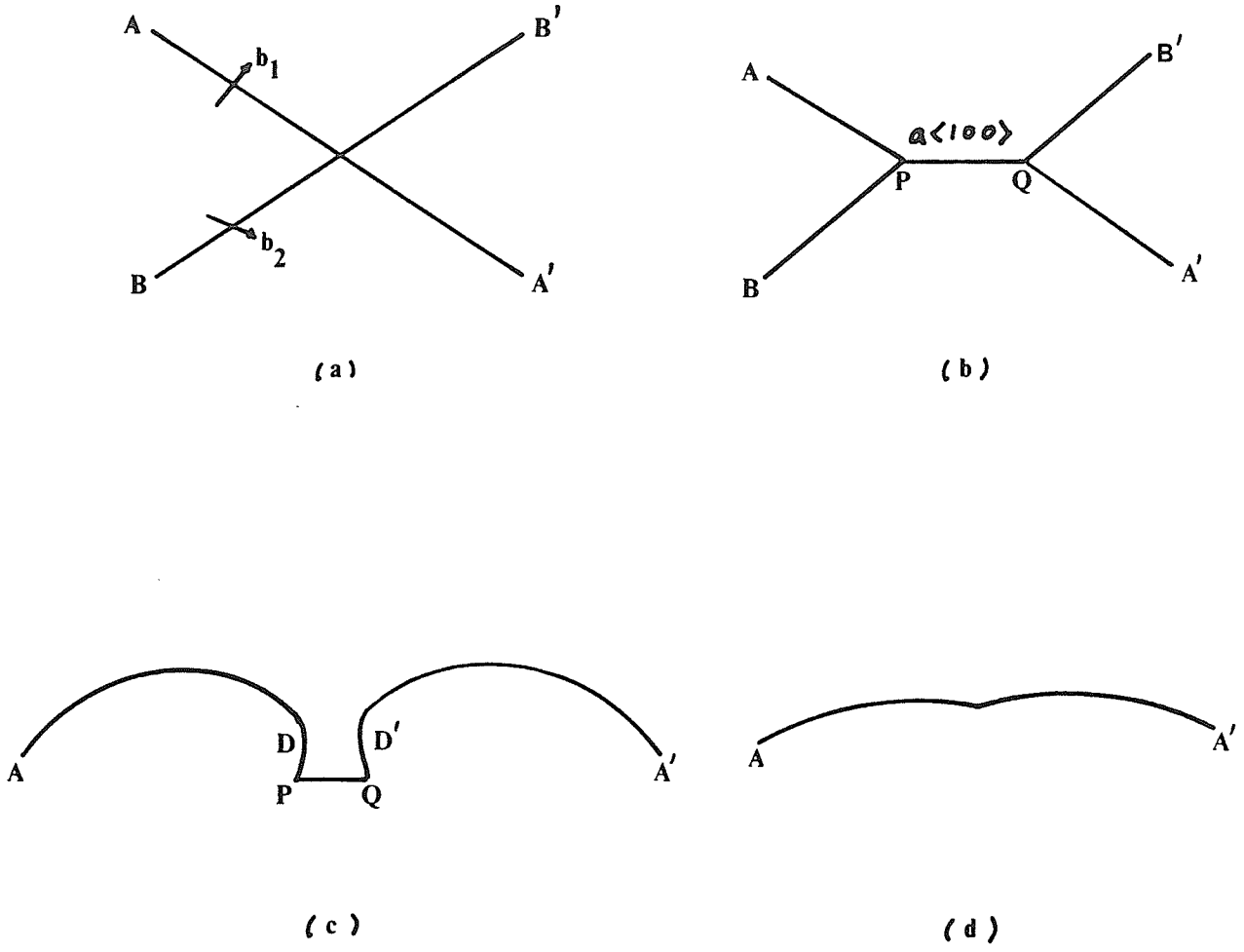

Fig. 4-23. (a) and (b), formation of attractive junction. (c) and (d), thermally activated unzipping of attractive junction.

The steady-state strain rate equals the product of an orientation factor η, the inverse of the time required to annihilate a dipole dislocation, the number of links in the subboundary, the area swept by the released loop, the Burgers vector, and the subgrain volume. That is

$$\dot{\varepsilon} = \eta \cdot V/(\ell/2) \cdot 3wL_s^2/\ell^3 \cdot L_s^2 \cdot b/L_s^3 \tag{4-18}$$

It is assumed that the average climb distance is $\ell/2$. The average climb velocity is given by Weertman[71]

$$V = (\beta\pi D/b)\ (\sigma\Omega/kT)/\ell n(\ell/b) \tag{4-19}$$

where $\beta \simeq 1$ and $\Omega \simeq b^3$.

Combining equation (4-18) and (4-19), we have

$$\dot{\varepsilon} = \left(\frac{6\eta\pi\beta w}{b\ell n(\ell/b)}\right)\ \left(\frac{D\ \mu\ b}{kT}\right)\ \left(\frac{\sigma}{\mu}\right)^5 \left(\frac{L_s}{b}\right) \tag{4-20}$$

(4-20)

$L_s = L_0(\mu/\sigma)$, $L_0 = 5\text{x}10^{-6}$mm (cf. 47),

$\eta = 10$, $\ell n\ (\ell/b) \simeq 10$.

The thickness of subboundary wall w, is not known. For the present purpose, we assume w = 1000b (cf. 68). Then equation (4-20) can be re-arranged into nondimensional terms,

$$\frac{\dot{\varepsilon}kT}{D\mu b} \simeq 1.5 \times 10^5\ (\sigma/\mu)^4 \tag{4-21}$$

A comparison of equation (4-21) with steady-state creep data[49] is shown in Fig. (4-24). The agreement is quite good, considering that equation(4-21) gives only the order of magnitude estimate. Several problems associated with this model are not solved. (1) The average climb velocity, equation (4-19), is derived from the climb of two straight dipole dislocations. The climb velocity of link dislocations is not known. (2) It is assumed that the glide of dislocations in the subgrain is instantaneous. This is known to be approximate. (3) The number of annihilating dipoles in the subboundary is not known. The assumption that it is equal to the number of link dislocations represents an overestimate (4) Equation (4-21) predicts a stress exponent n=4. If pipe diffusion is involved[76], the diffusion coefficient in equation (4-20) should be replaced by $(D/\ln(\mu/2\sigma) + 3D_p \sigma^2 / \mu^2)$. Then the stress exponent varies between 4 and 6. However, the measured n value for iron is 8, which can not be understood in terms of the existing theories. Nevertheless, the above model is an attempt to describe the steady-state flow in terms of the microstructures.

For completion, the use of activation volumes as an indicator of a specific rate-controlling mechanism, must be discussed briefly. The unit activation process during the climb of a dislocation is the absorption or emission of a single vacancy. This is accomplished by the movement of a jog along the dislocation line. Therefore, the activation area, that is the area swept by the dislocation during thermal activation, is approximately equal to b^2 (or $V^* \approx b^3$).

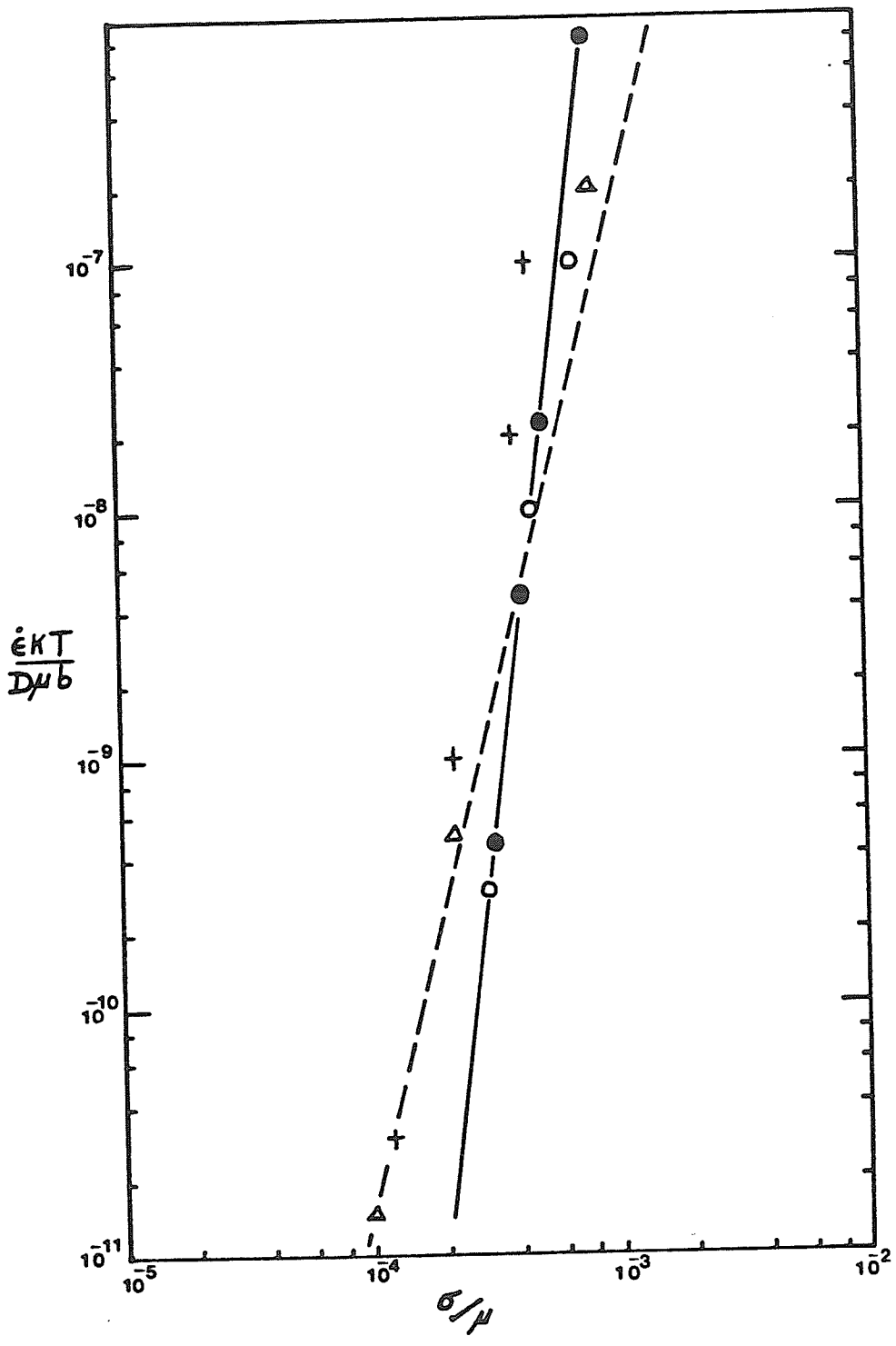

Fig. 4-24 Comparison of the present data (●) with the prediction of equation 4- 21 (– – –). The shear modulus and diffusion data are taken from references 77 and 118. The steady-state creep data[49] for Fe (o), W (+) and Nb (Δ) are also shown in this figure.

However the experimental activation volume depicted in Fig. 4-18 varies between 200 to 4000 b^3. In fact, these are not the true activation volumes. The experimental activation volume, V^*, evaluated according to equation (2-16) is equal to V^* defined by equation (2-25) only when the pre-exponential factor, $\dot{\epsilon}_o$, in equation (2-17) is not a function of stress. This is approximately satisfied in region I. Immarigeon and Jonas[10] have shown that $\dot{\epsilon}_o$ is a power function of stress for iron deformed in region III. Then

$$V^* = kT \left[\partial \ell n \left(\dot{\epsilon}/\dot{\epsilon}_o\right)/\partial\tau\right]_T = V_a^* - kT \left(\frac{\partial \ell n \dot{\epsilon}_o}{\partial \tau^*}\right)_T$$

If $\dot{\epsilon}_o$ = constant $\cdot \tau^{*n}$, then

$$V_a^* = b^3 + nkT/\tau^*$$

Therefore the strong stress dependence of the experimental activation volume is not in conflict with the operation of the climb-controlled mechanism.

4.3 SUMMARY AND CONCLUSIONS

1. The temperature sensitivity of effective stress, $\partial\tau^* / \partial T$, of Ferrovac E iron has been measured between 4.2 and 300K. This quantity is not linearly dependent on temperature, if the datum points below 77 K are included. The effective stresses have also been evaluated. Our results show that Smidt's linear approximation (equation (4-1)) underestimated the effective stress below 77 K. The effective stress at 0 K is estimated to be 52.5 Kg/mm^2 (515 MPa). This is the stress which is required to move a screw dislocation at absolute zero. Since Ferrovac E iron contains 350 atppm of carbon and nitrogen, the two strong hardeners for iron, the true intrinsic properties of iron are, in fact modified by these interstitial atoms.

2. The Battelle iron has impurity contents which are about an order of magnitude lower than that of Ferrovac E iron. Accordingly, the flow behavior of Battelle iron would reflect to a greater degree its intrinsic properties. The temperature sensitivity of the effective stress of Battelle iron consists of two approximately linear portions of different slopes connected by a transition region centered at 220 K. The Battelle iron has higher temperature sensitivities of effective stress than that of Ferrovac E iron between 220 and 300 K. It has been identified that solute atoms can cause softening between 180 and 300 K and hardening below 180K.

3. Recent atomistic calculations[23,24] have shown that screw dislocation in b.c.c. metals have three-fold symmetry. As a result of that, the core of a screw dislocation would have to undergo a major

modification before it can glide. Based on the present data, it is speculated that the strain rate is controlled by the double-kink nucleation at low stresses and kink migration at high stresses.

4. At intermediate temperatures (T > 300 K for $\dot{\varepsilon} = 0.0025\ \text{min}^{-1}$.), the Peierls barriers become transparent to screw dislocations because there is sufficient thermal fluctuations in the crystal. Therefore, the thermal component of flow stress becomes zero. Dislocations move by overcoming the long-range internal stress, which is mainly due to the formation of attractive junction dislocations.

5. At high temperature (T > 670 K, the transition temperature varies with strain rate and strain), the flow stress of iron becomes sensitive to temperature and strain rate again. The high temperature flow of iron is characterized by a steady-state flow at large strains. In pure metals, steady-state flow is generally associated with the formation of a steady-state substructure. It is assumed that the subboundary network controls the steady-state flow. The glide of dislocations in the subgrain produces the only significant strain. This leads to the strain-rate equation

$$\dot{\varepsilon} kT/D\mu b \simeq 1.5 \times 10^{5} \ (\sigma/\mu)^{4}$$

It gives a reasonable estimate of steady-state strain rate for several b.c.c. metals. The above equation predicts a stress exponent of 4, which is only one half of the measured n value for iron.

PART II

DEFORMATION OF TWO-PHASE SYSTEM

CHAPTER 5

DUAL-PHASE STEEL

The element iron, which is one of the most important engineering materials, is not always used in the pure state. Carbon, by far the most efficient hardener for iron, is used to make various grades of steels. Iron alloys of technological importance are in fact often composed of two or more phases. To understand or to predict the mechanical behavior of such mixtures, one must know the mechnical properties of each phase and the interaction of two phases. The study of the mechanical properties of α-phase in Part I provides the background knowledge for the understanding of the behavior of two-phase systems.

Two-phase materials in general may be divided into three classes based on the geometry of their microstructures.

(1) Dispersion and precipitation hardened alloys.

The harder second phase may be present in the form of particles. The mechanical properties of this class of materials are well understood in terms of Orowan mechanism. If the hardness of the particles is much greater than that of the matrix, two additional stresses are required to deform the matrix : (a) the stress required to bow dislocation between two adjacent particles and (b) a uniform back stress which is proportional to the volume fraction of the particles and the shear strain cause by the Orowan dislocation loops around each particle.[78]

(2) Fibre composite.

The extension of the harder second phase in one dimension facilitates

the load transfer to the fibre, if the fibres are aligned with the stress axis. When the fibre is continuous then, the yield strength of the composite obeys the rule of mixtures.

(3) Two-phase material with coarse microstructures.

We will only deal with this type of material in this section. In this class of materials, the grain sizes or mean-free-paths of the two phases are comparable. It comprises a large amount of engineering materials, including the dual-phase steels of recent development. The strength and plasticity of these materials are not well understood due to the inherent complexity of their microstructures. The relevant structural parameters which affect the mechanical properties of coarse two-phase alloys have been summarized by Fischmeister and Karlsson.[79] They are (a) the volume fractions of the constituent phases, (b) the size and shape of the constituent regions, (c) continuity, and (d) the flow stress ratio of the two phases. In general, the distribution of stress and strain in each phase falls intermediate between the two simple models, i.e., the isostrain and isostress models. Fischmeister and Karlsson[79] have shown that the strain distribution in the matrix phase depends on the distribution and shape of the harder second phase. The continuity and the aspect ratio determine load distribution in each phase. The relative strength of each phase affects both stress and strain distribution. Since several structural variables are involved, the description of plasticity of two-phase materials in terms of dislocations has not been successful. The only promising tool is the finite-element method applied to the actual microstructure, although only two-dimensional

case has been done so far.[79]

Iron-carbon system can be used to produce a series of coarse two-phase alloys, such as ferrite-cementite and ferrite-martensite mixtures. The latter has been designated as dual-phase steel. Although it is still under development, it is becoming "the steel of the 1980's" (just as the high strength low alloy (HSLA) steel was the steel of 1970's). The dual-phase steel was originally derived from HSLA steels by intercritically annealing and/or quenching these steels, Fig. 5-1. The resulting dual-phase steels not only have the same tensile strength as their parents HSLA steels, but also exhibit superior formability.[80] One of the objectives of this investigation is to study the work-hardening characteristics and Bauschinger effect of a dual-phase steel.

When work hardenable materials, particularly plastically inhomogenous materials, are deformed by forward and then reverse loading, they usually exhibit a decreased reverse yield stress. This decrease of the yield stress is identified as Bauschinger effect (BE). For the quantitative assessment of BE, it is convenient to plot both forward and reverse stresses in the positive direction as a function of cumulative strain. In some instances the reverse flow curve is displaced to lower stresses and eventually becomes parallel with the forward curve. The stress difference of parallel displacement is termed permanent softening. Orowan[86] suggested that the permanent softening was cause by long range back stress. He also suggested that on reverse straining the back stress should vanish at about 1 to 3% strain. This has been verified by Wilson,[83] who

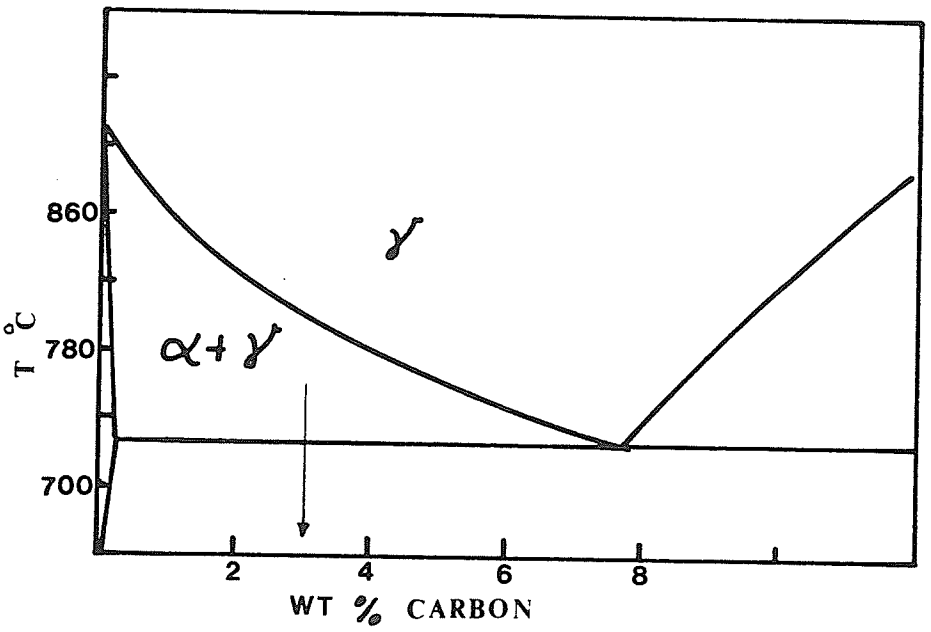

Fig. 5-1 Phase diagram of iron-carbon system.

measured X-ray line shifts and found that at the critical reverse strain where the mean internal stress decayed to zero, the permanent softening was approximately twice the mean internal stress which existed prior to reverse straining.

Many models have been suggested to explain BE. They have been critically reviewed recently by Sowerby, et al..[87] In general, these models can be classified as microscopic and continuum models. The microscopic models are concerned with dislocation arrangement which produces long-range back stress. On the other hand, the continuum models disregard microstructural details and divide the work-hardening into isotropic and kinematic hardening. Isotropic hardening is due to the uniform expansion of the original yield surface, while kinematic hardening occurs by translation of the initial yield surface in the stress space. We will compare the predictions of both microscopic and continuum models with experimental results.

5.1 EXPERIMENTAL PROCEDURES

The material used in this study was HSLA line-pipe steel. The composition was, in Wt%, 0.10 C, 1.55 Mn, 0.014 P, 0.006S, 0.27Si, 0.040Nb, and 0.035V. Rods were cut from the as-received 3/4" thick gas pipe along the axis of the pipe. The rods were normalized at 900^{o} C for 30 minutes and air-cooled to room temperature. They were machined into cylindrical specimens having the dimensions of the gage section of 12mm x 6mm (diameter). This aspect ratio was adequate for compression up to 6% strain without buckling. The specimens were annealed at temperatures between 730 and 865 C for 30 minutes and quenched into water at 22 C. Tension-compression tests were carried out on a MTS machine equipped with a Wood's metal grip.

The specimens for metallographic examinations were mounted in Castolite resin and etched in a mixture of saturated picral and 1% sodium bisulfide in equal volume.[81] The volume fraction and the mean-free-path of martensite regions were measured on a Bausch and Lomb image analyser. The average strains of ferrite and martensite regions were obtained by measuring the average grain diameter in the direction of the stress axis. The external strain of the cylindrical specimen was estimated by measuring the decrease in the diameter using an optical comparator. The lateral strain was converted to axial strain using the measured Poisson's ratio of ν=0.51 in the plastic range.

The microhardness tests were made using a 20 gram indenting load in a region at least three times larger than the diagonal of the indentation.

5.2 RESULTS

1. Microstructure

Fig. (5-2) shows the two-phase microstructures resulting from intercritical anneal at various temperatures. It can be seen that some banding of martensite still remains, even though the specimens are normalized before the intercritical anneal. The morphology and the structure of martensite appear to vary with annealing temperature. The austenite grains are nucleated mainly on the ferrite grain boundaries. The martensite produced by quenching from 730 and 760 C does not show any fine structure even at a magnification of 3000. It, therefore, can be concluded that the softer ferrite in the two-phase structure does not provide strong enough constraint which is apparently necessary during martensitic transformation to produce plate-martensite such as in fully martensitic high carbon steels. On the other hand, the martensite produced by quenching from 820 and 865 C are of lath-type, characteristic of low-carbon martensite.

Fig. (5-3) shows the hardness variation during isochronal anneal of dual-phase and fully martensitic steels. The first dip in the curve has been identified metallographically to be due to tempering of martensite. This occurs at 150^{o} C for the fully martensitic steel and 200^{o} C for the dual phase steel. The cause of the second dip was not investigated.

All the dual-phase steels used in this study do not contain any detectable retained austenite. The specimens for X-ray diffraction test were chemically polished to prevent deformation. The X-ray machine was set in the proper sensitivity range and calibrated to

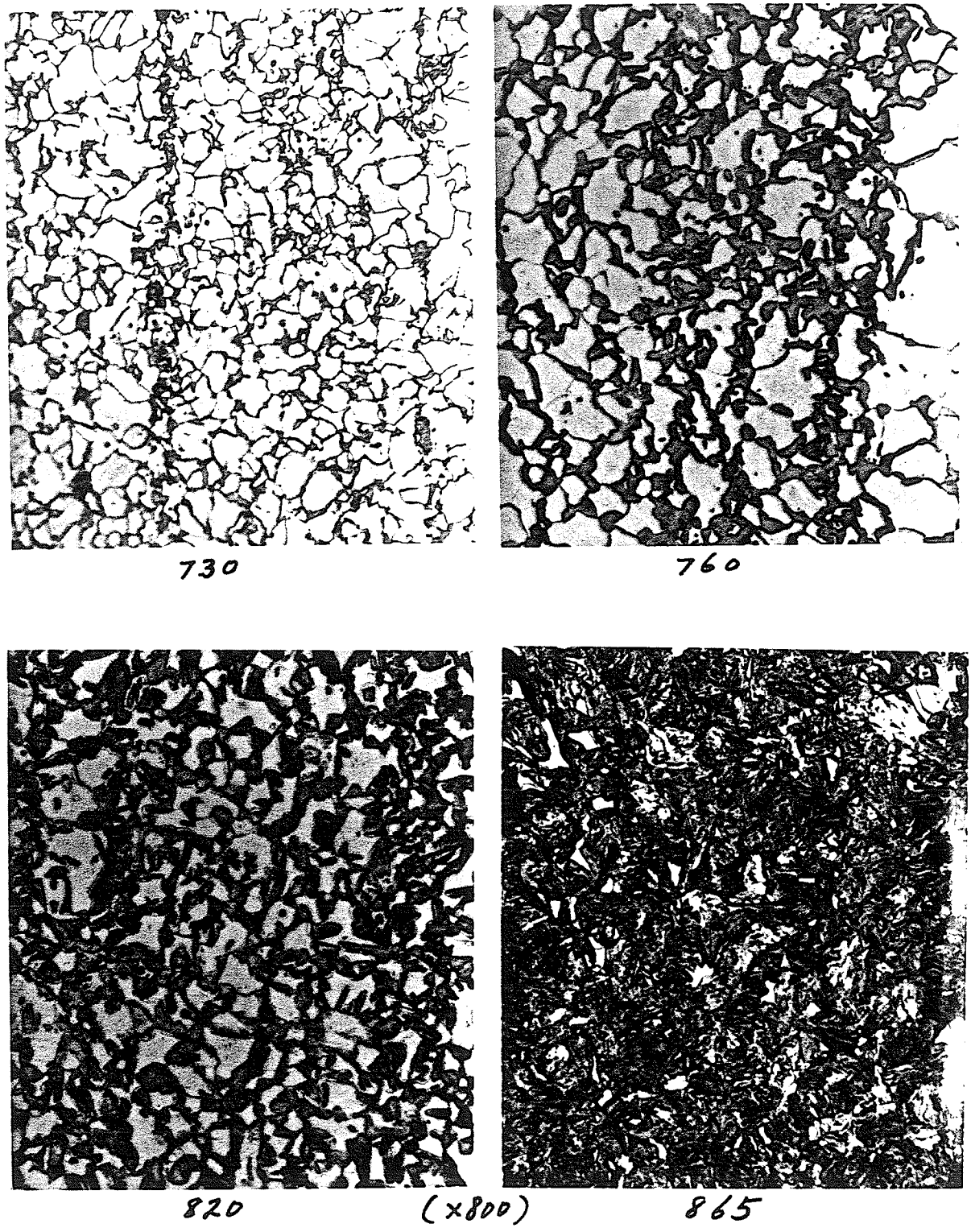

Fig. 5-2 Two-phase microstructures resulting from intercritical anneal at various temperatures.

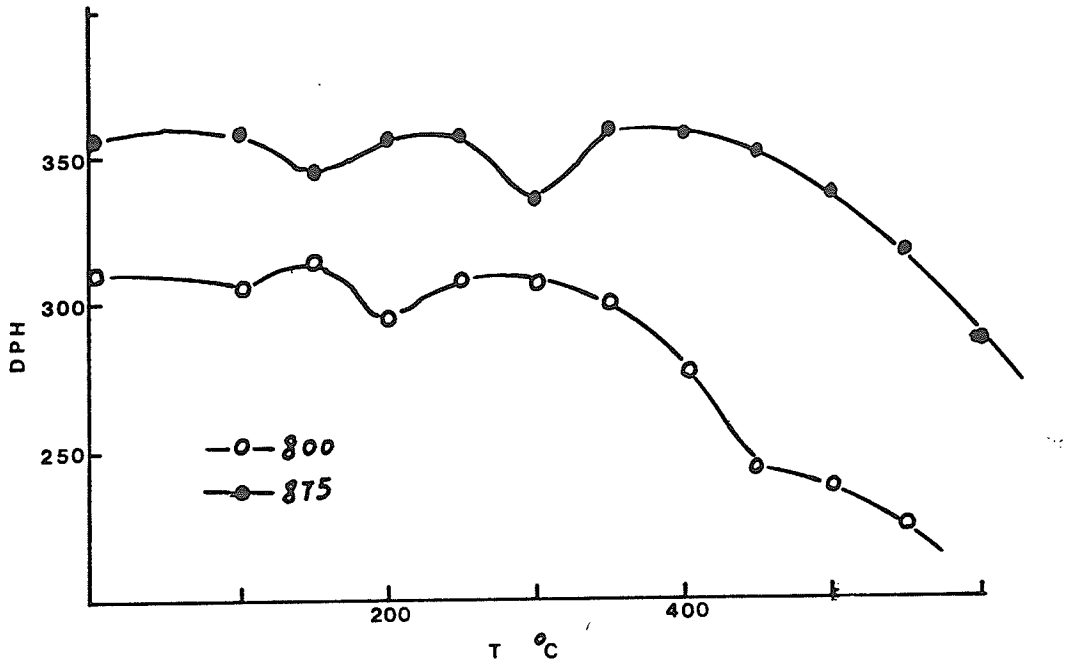

Fig. 5-3 Hardness variation during isochronal anneal of dual-phase and fully martensitic steels.

detect at least one volume per cent of austenite. High Mn steels often contain significant amount of austenite because Mn tends to stabilize the austenite phase.

2. Work-hardening

The work-hardening behavior is often analyzed in terms of the power law

$$\sigma = K\varepsilon_p^n \qquad (5\text{-}1)$$

where σ = true stress

ε_p = true plastic strain

n = strain hardening coefficient

When equation (5-1) is obeyed, n is equal to the uniform strain[80]. The log-log plots of the stress-strain curves (Fig. 5-4a) for the four dual-phase steels are depicted in Fig. (5-4b). It can be seen that the plots are not linear, indicating that equation (5-1) is not obeyed in this dual-phase system. The curvature increases with increasing martensite content. Rashid[82] also found similar behavior in the GM-980 X dual-phase steel. The work-hardening rate, $\Theta \equiv d\sigma/d\varepsilon$, for the first three percent strain are shown in Fig. (5-5). The steel produced at the intercritical anneal temperature (IAT) of 730° C has a lower initial work-hardening rate. The rest of the dual-phase steels seem to have the same initial work-hardening rate. The work-hardening rate can be normalized with flow stress to distinguish the extent of uniform strain, assuming the instability criterion $\Theta/\sigma = 1$. These are shown in Fig. (5-6). The steel having the highest strength (IAT =865° C) has only about 5% uniform strain. The uniform strain increases with decreasing strength. Davies[80] has shown that uniform strain decreases with increasing martensite content in other dual-phase steels.

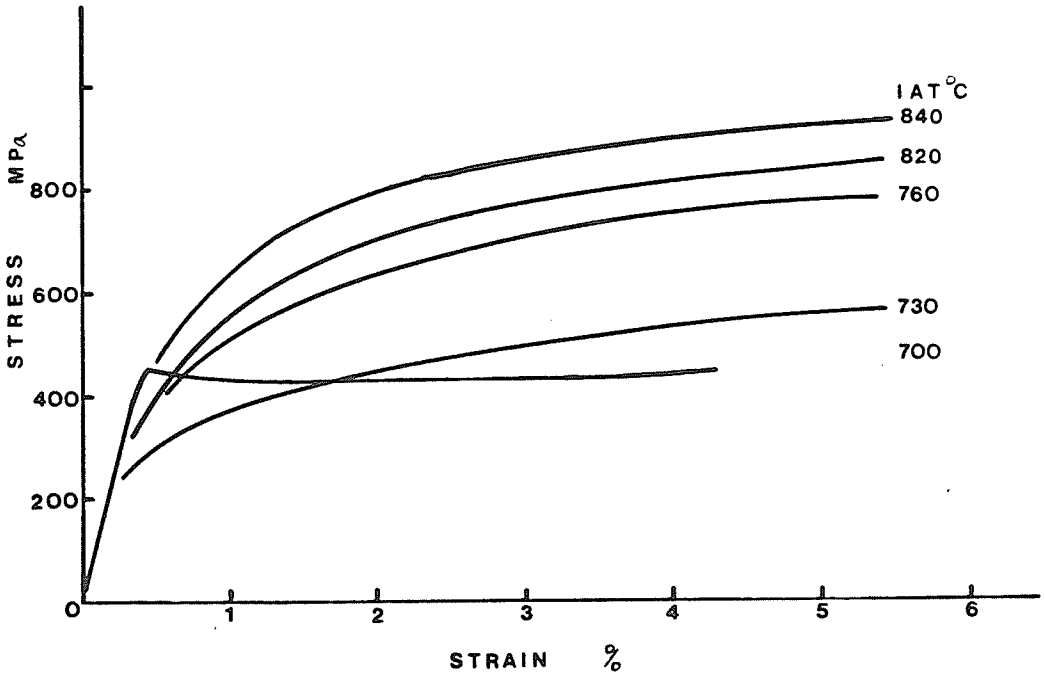

Fig.5 -4a σ-ϵ curves.

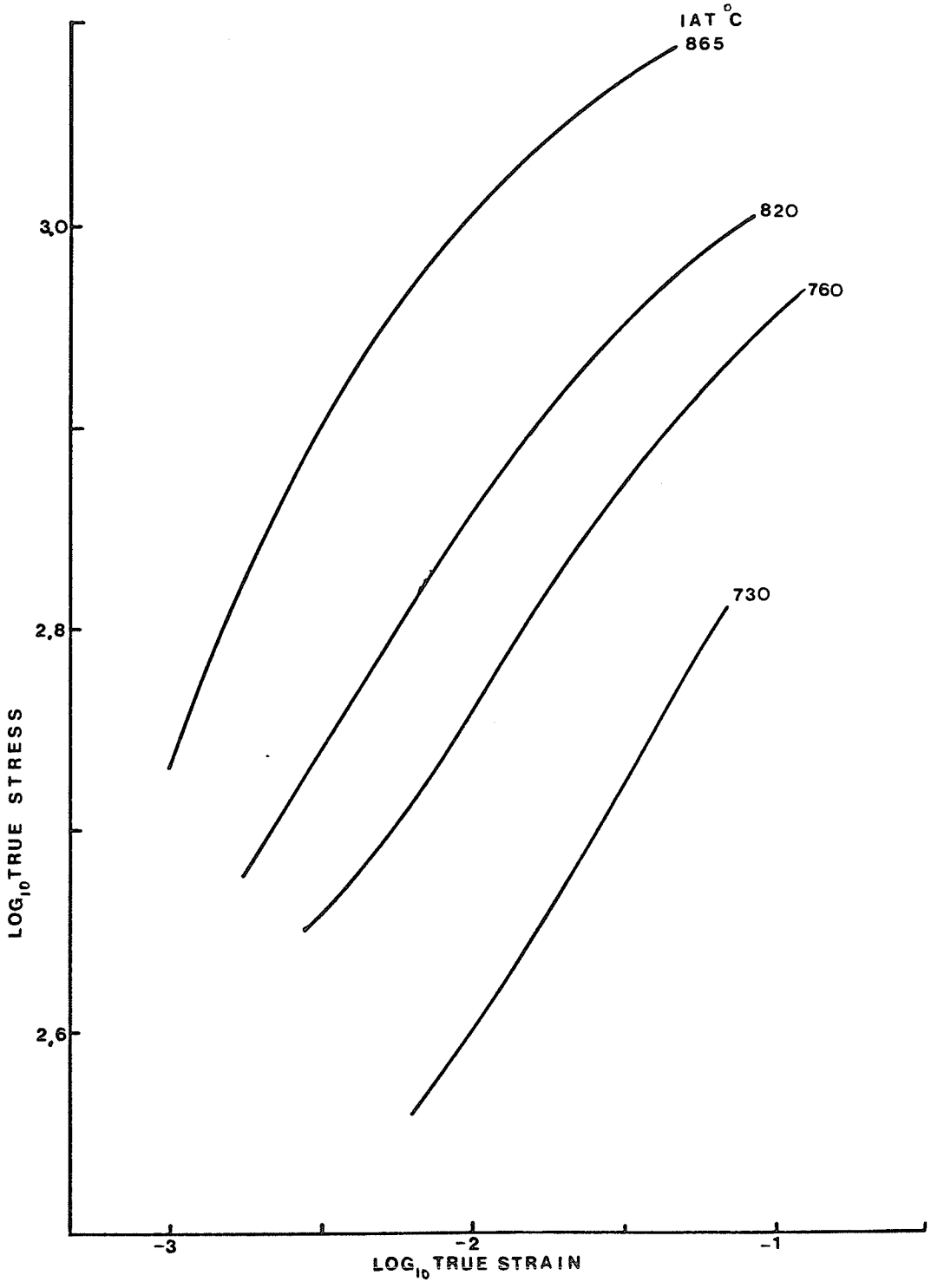

Fig. 5-4b $\log \sigma - \log \epsilon_p$ plots.

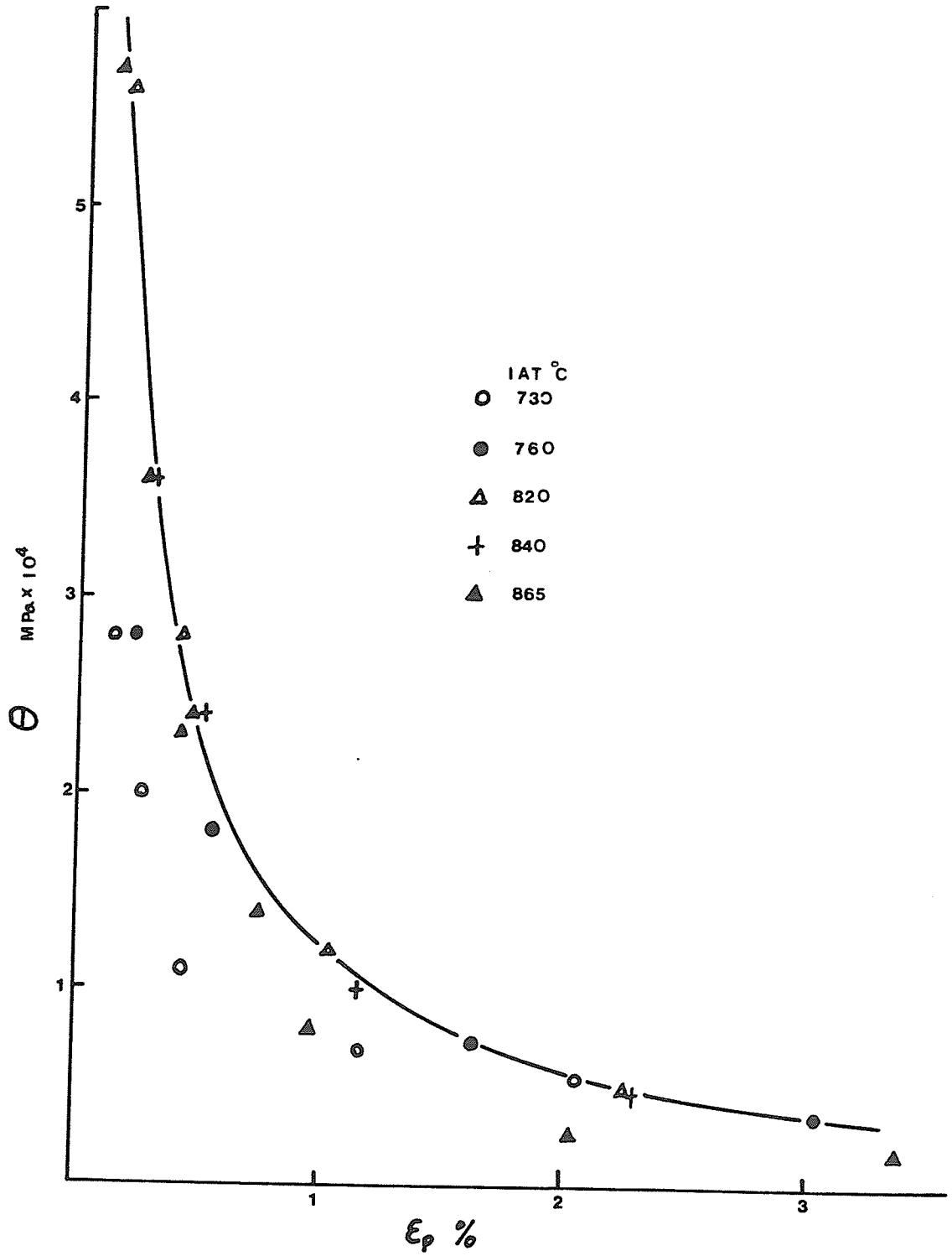

Fig.5 -5 Work hardening rate as a function of plastic strain.

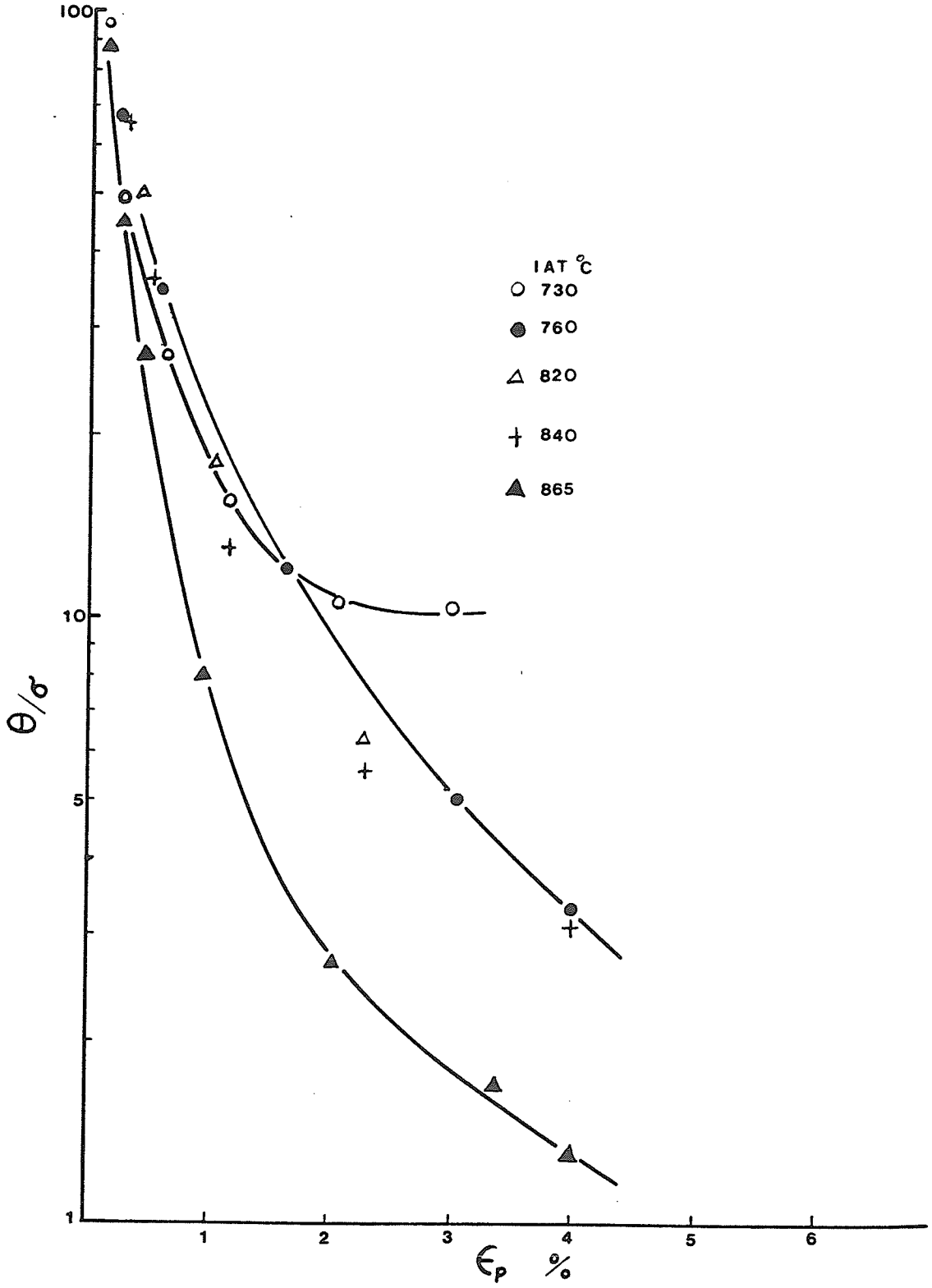

Fig.5 -6 Normalized work hardening rate.

Fig. (5-7) shows the flow stress as a function of martensite content at various plastic strains. The plots are essentially linear. Davies[80] also found similar results in other dual-phase steels. However, the linearity of the plots in Fig. (5-7) does not necessarily imply the applicability of the rule of mixtures, unless the strength of each phase is held constant. Another point of interest is that the strength of fully martensitic steel is much higher than that predicted by extrapolation of the plots in Fig. (5-7).

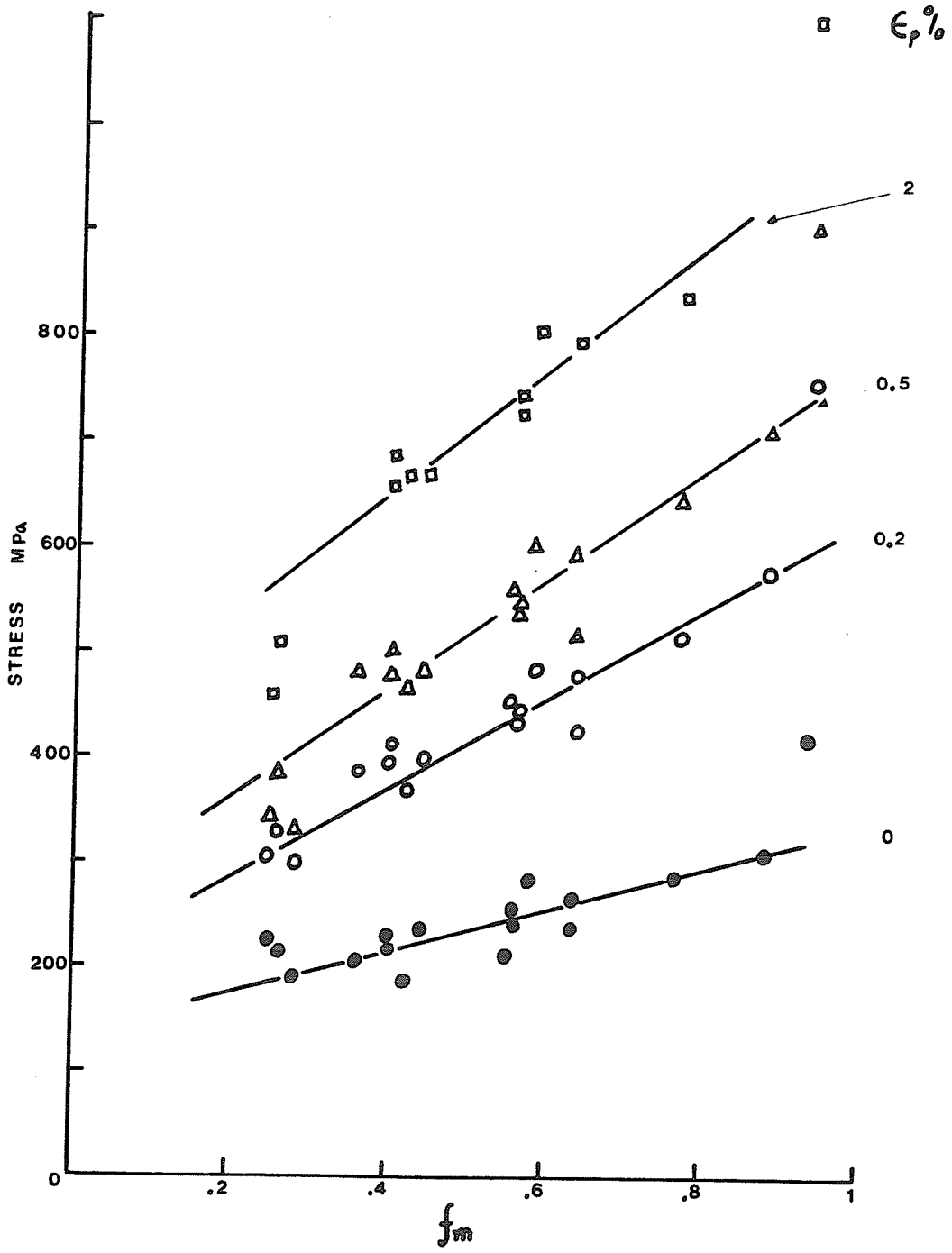

Fig.5 -7 Flow stress versus volume fraction of martensite.

3. Bauschinger Effect

To show the Bauschinger effect, the compression part of the stress-strain curve is plotted by inversion with respect to the point at which the unloading elastic line meets the strain-axis. The typical results are shown in Fig. (5-8). Since the work-hardening rate in the compression cycle is greater than that for the continued tensile deformation, the permanent softening effect[83] does not exist in this dual-phase steel. The decay of the stress difference, $\Delta\sigma = \sigma_F - \sigma_R$ follows approximately an exponential function of reverse strain ε_R,

$$\Delta\sigma/\sigma_u = A' \exp(-m\varepsilon_R) \qquad (5\text{-}2)$$

where σ_F and σ_R are forward and reverse flow stresses respectively at a given accumulated strain. σ_u is the forward stress at unloading. m and A' are evaluated from Fig. (5-9) as m = 23 and A' varies between 3 to 10. When the martensite content falls below 30%, such as in the dual-phase steel produced at IAT of 730° C and those containing ferrite and carbides, the decay of $\Delta\sigma$ does not follow equation (5-2).

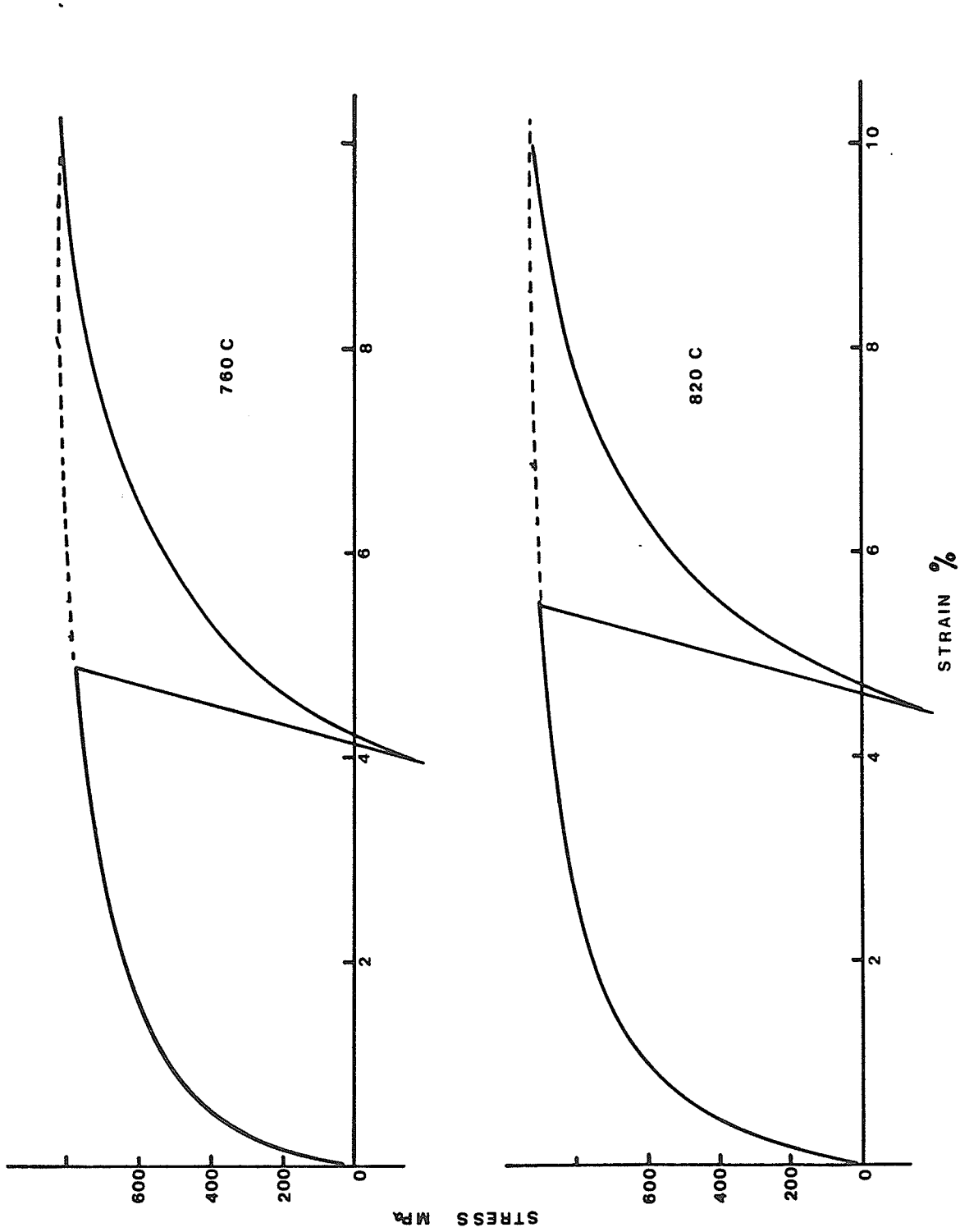

Fig. 5 -8 Stress-strain curves for tension-compression cycle.

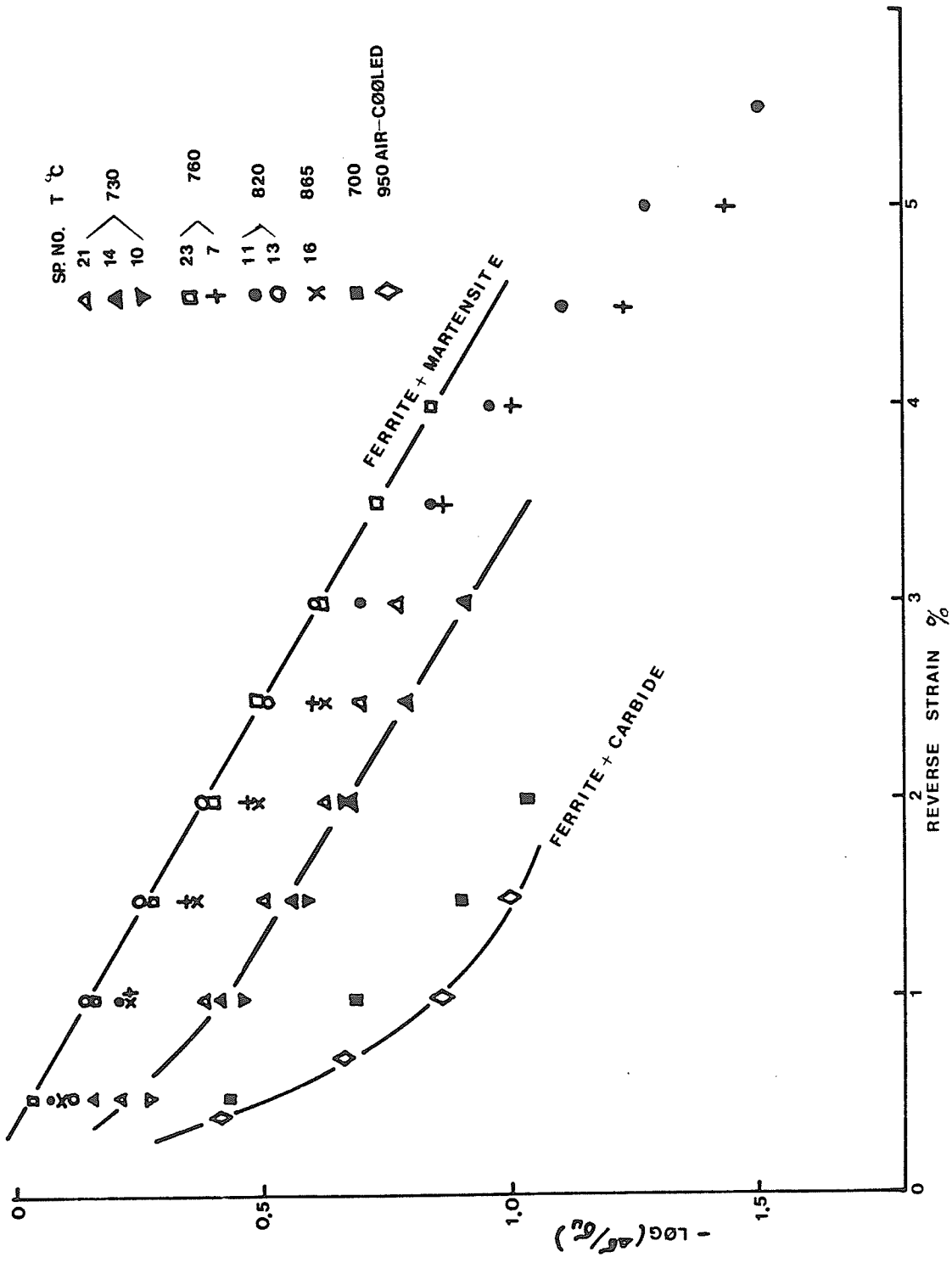

Fig. 5 -9 The deacy of the stress difference as a function of reverse strain.

Since the present system does not show permanent softening, the back stress, which is equal to one half of the permanent softening as has been suggested by Wilson[83], can not be determined here. However, to show the Bauschinger effect, $\Delta\sigma$ at a given reverse strain is plotted against the forward pre-strain ε_F. Fig. (5-10) shows $\Delta\sigma/2$ at $\varepsilon_R = 0.5\%$ for the four dual-phase steels. The back stress hardening for the steel produced at IAT = 730 and 865 C appears to saturate at about $\varepsilon_F = 10\%$. This is similar to the dispersion hardened alloys.[84] For IAT = 760° and 820° C, $\Delta\sigma$ increases with forward strain.

The area between the forward and reverse stress-strain curves, that is, the strain energy E_S, can also be used to characterize the Bauschinger effect, The average Bauschinger strain[85] is defined by

$$\varepsilon_{ABS} = E_S / \sigma_u \qquad (5\text{-}3)$$

The results are shown in Fig. (5-11). The average Bauschinger strain increases with increasing forward strain. In resemblance to Fig. (5-9), the datum points of ε_{ABS} fall in a scatter band, except for those steels produced at IAT = 730° C and below. Therefore, it can be concluded that a strong Bauschinger effect results when the martensite content is greater than 30%, above which the effect becomes less sensitive to the martensite content.[117]

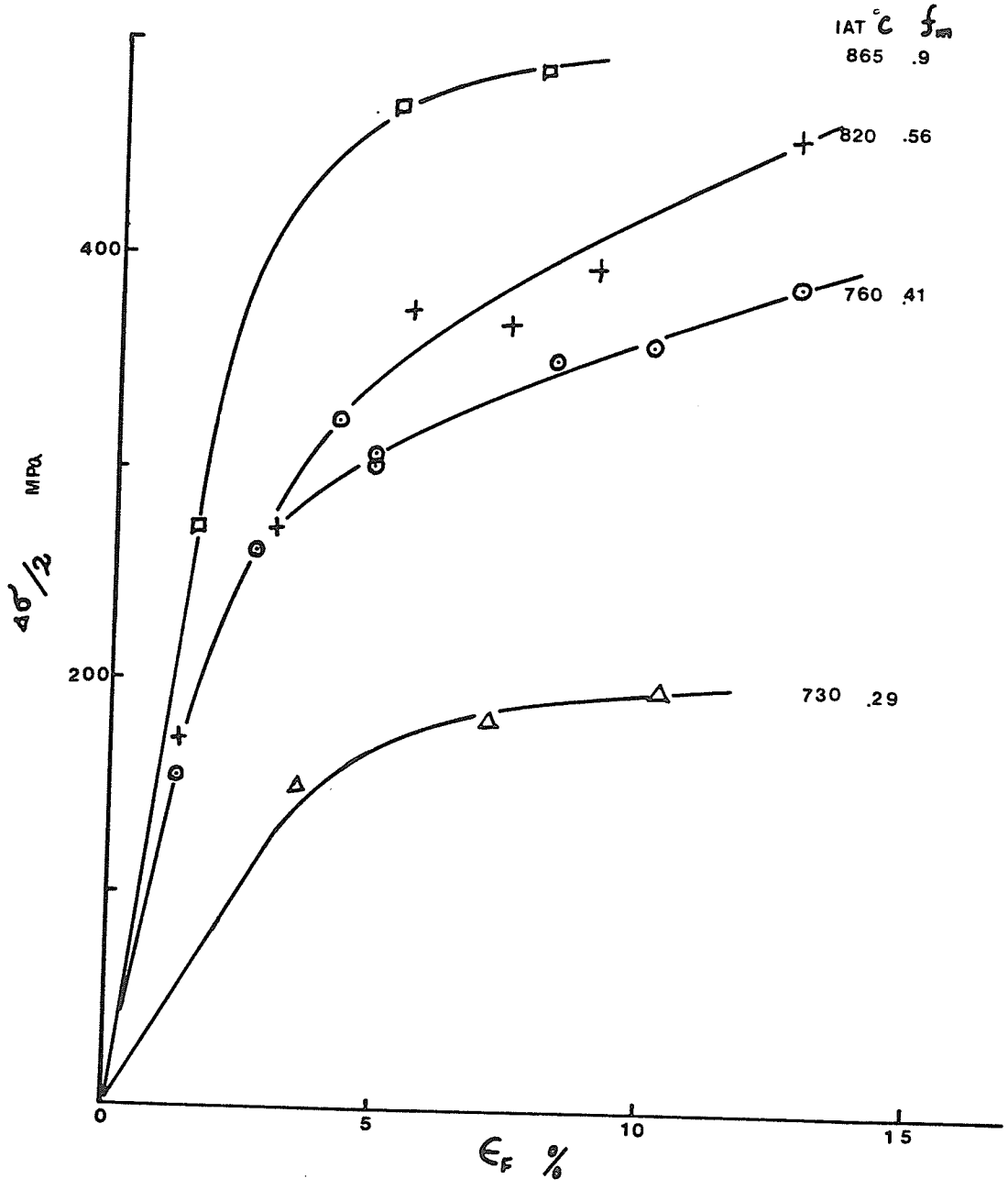

Fig. 5-10 $(\sigma_F - \sigma_R)/2$ measured at ϵ_R=0.5% as a function of ϵ_F

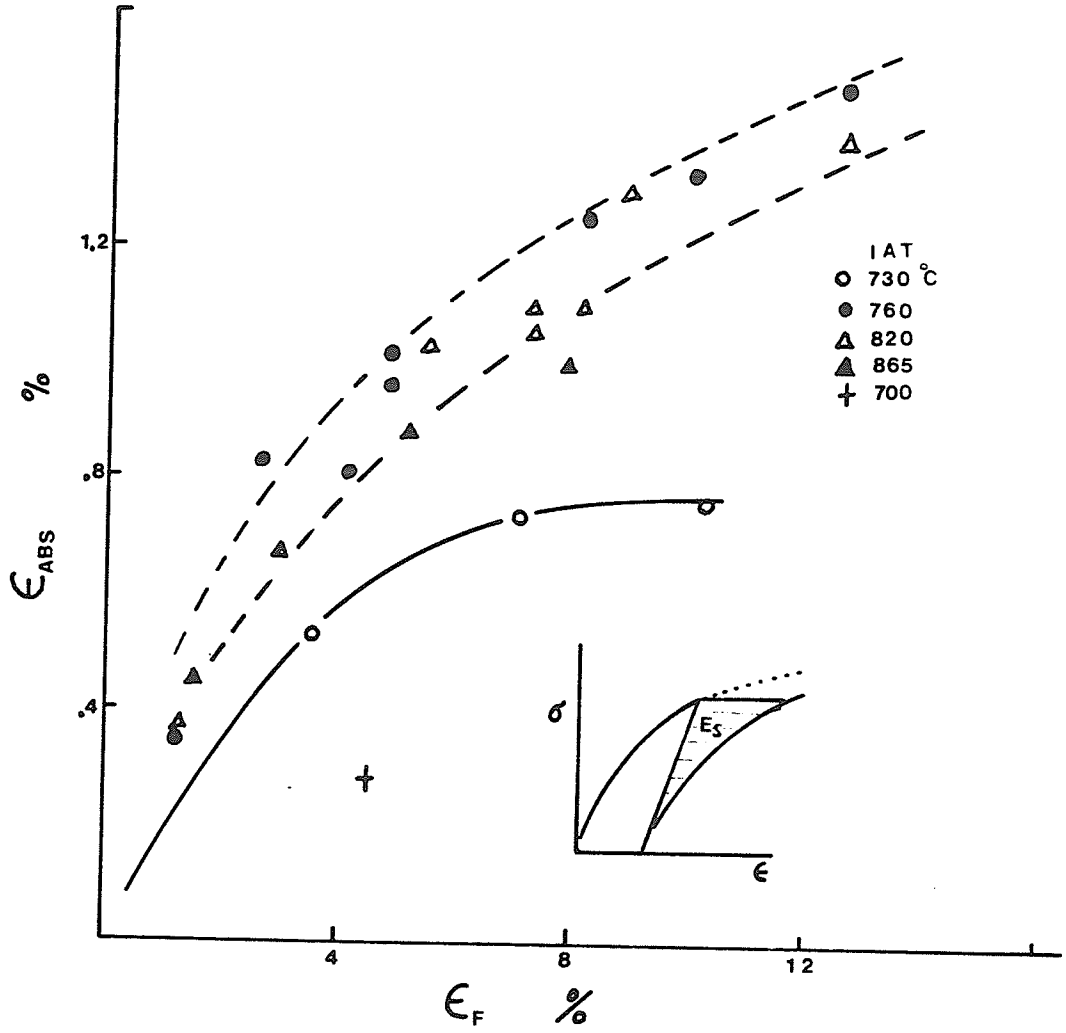

Fig. 5 -11 Average Bauschinger strain as a function of forward strain.

4. The effect of intercritical annealing temperature on hardness.

The microhardness of both martensite and ferrite in as-quenched dual-phase steels was measured with a 20 gram indenting load. The results are shown in Fig. (5-12). Since the carbon content of martensite decreases with increasing IAT, therefore its hardness decreases with increasing IAT. However the increase in hardness of ferrite with increasing IAT is unexpected. This might be due to alloys partitioning between ferrite and austenite or precipitation of NbC and VC in the ferrite. More work is required to clear this problem. The macrohardness is also shown in Fig. (5-12). The indentations were made with 40 Kg indenting load to give an average hardness of the composite. The average hardness evaluated from the rule of mixtures is also shown in this figure for comparison. It is clear that the macrohardness is much less than that predicted by the rule of mixtures.

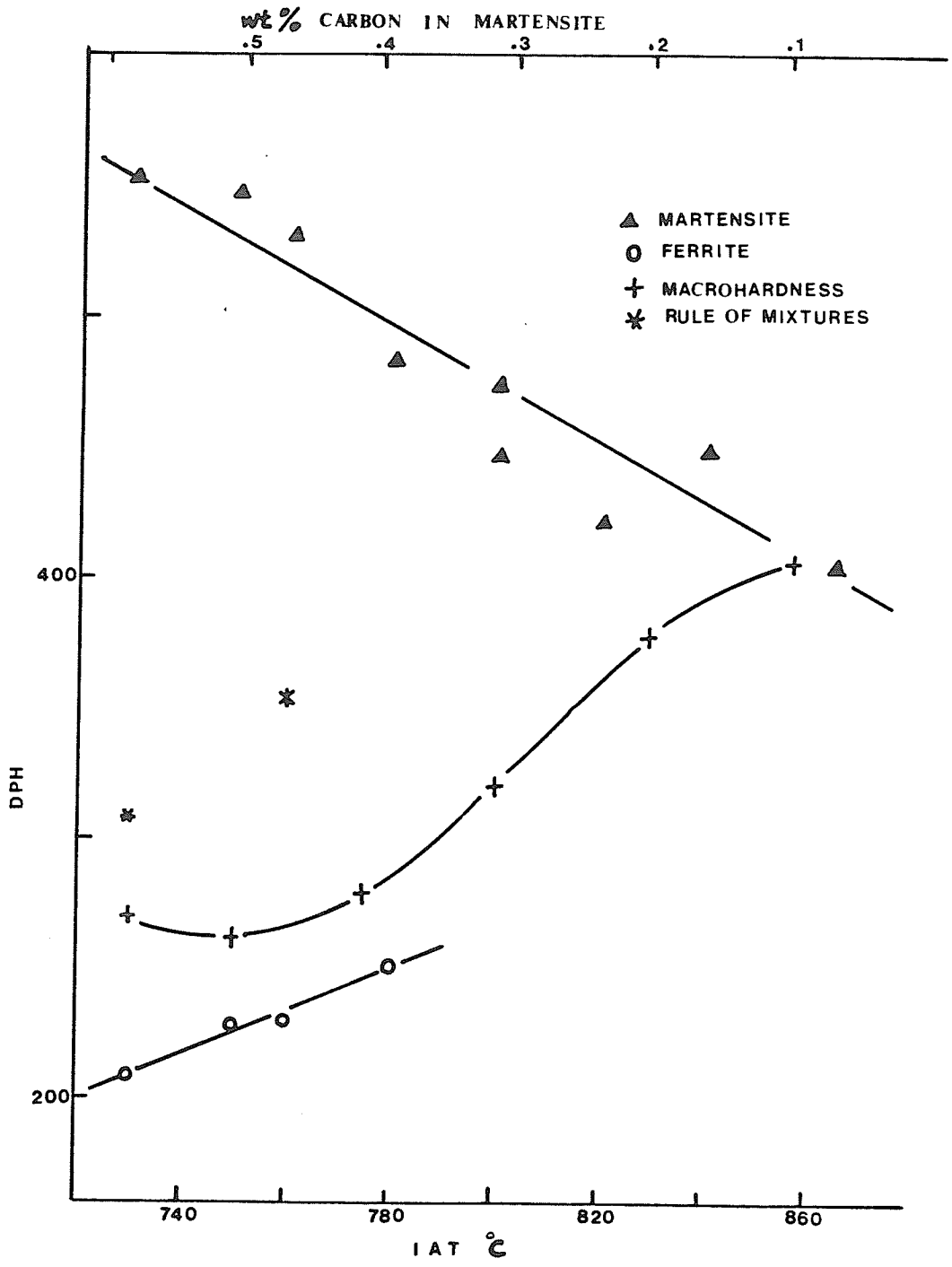

Fig. 5-12 The microhardness of martensite and ferrite versus the annealing temperature. The indentations are made with 20 gram. The macrohardness indentations are made with 40 Kg.

5. Deformation of martensite and ferrite regions in dual-phase steels.

The strains of martensite and ferrite regions in a fractured cylindrical specimen were estimated by measuring the average mean-free-path of each phase along the cylindrical axis. The strain at each point can be evaluated by comparing the mean-free-path at that position with that of the underformed shoulder section. Some void formation at the martensite-ferrite inteface is apparent near the fracture surface. The void was counted as part of martensite region by the image analyzer. This results in an overestimate of the strains of martensite region near the fracture surface. The results are shown in Fig. (5-13). With the reservation stated above, both martensite and ferrite deform by equal amount throughout the strain range of 33%. This is in good support of the isostrain hypothesis often used to analyze the deformation of dual-phase steels. These results are probably only valid in this dual-phase steel which is intercritically annealed at 760^{o} C containing 43% martensite. The general validity of the isostrain condition in other dual-phase steels is not observed.[93]

The strength and ductility of dual-phase steels are sensitive to cooling rate. A batch of flat tensile samples of 2 mm thickness were intercritically annealed at 760^{o} C for 30 minutes and then quenched into either water at 0^{o} C or oil at 22^{o} C. The total elongation for the oil-quenched samples varies between 25 and 30%, whereas that for the water-quenched samples is 10 - 15%. The water-quenched samples have higher strength at the expense of ductility. The higher strength

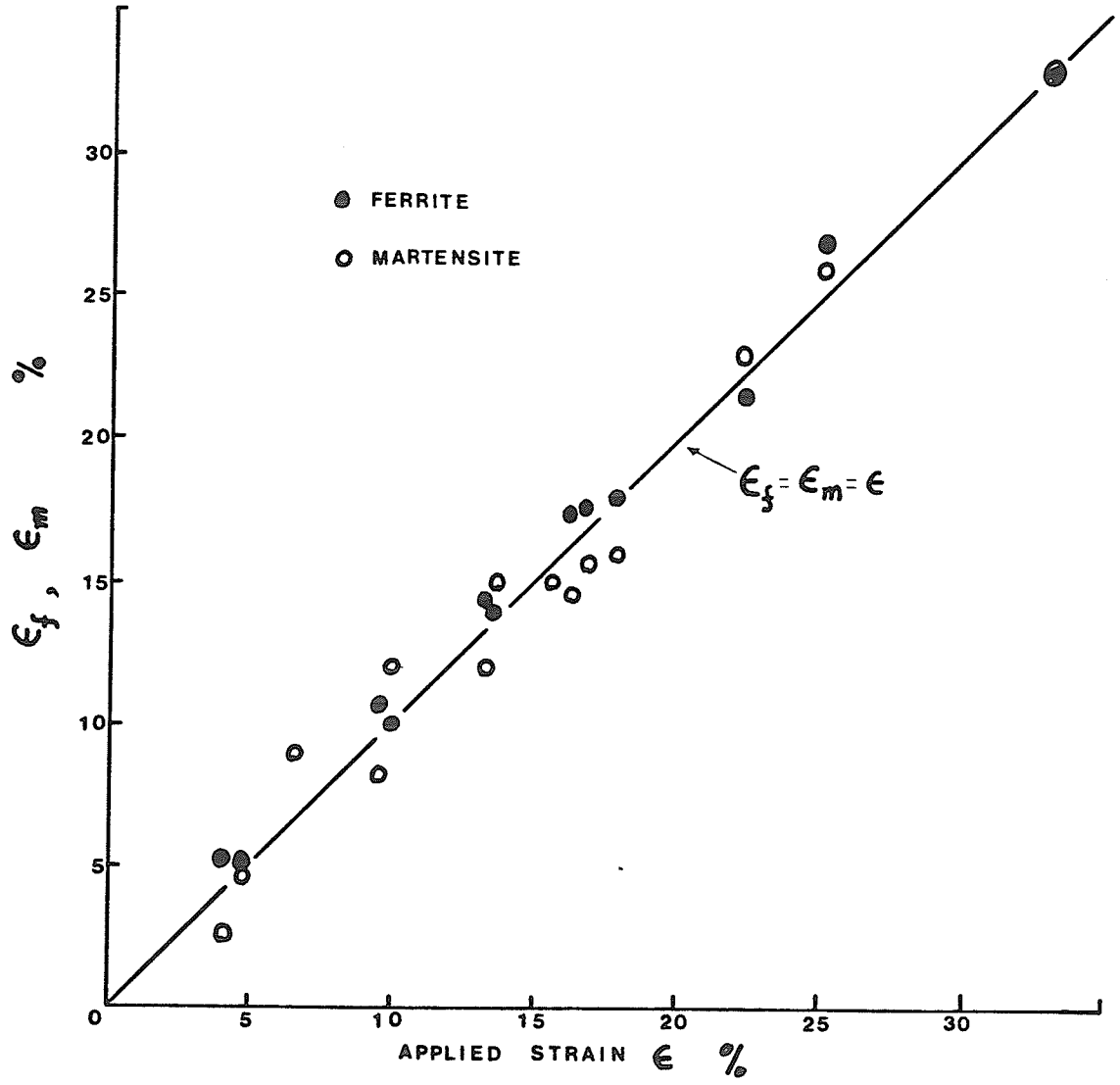

Fig. 5-13 The strains of ferrite and martensite in a fractured tensile specimen containing 43% martensite.

is due to the higher hardness of the martensite regions in water-quenched samples. Therefore some compromise between strength and ductility must be made to optimize the properties of a dual-phase steel for any specific application.

The fracture surfaces for the four dual-phase steels are of ductile nature. The fractographs are shown in Fig. (5-14). The larger dimples are formed in the ferrite regions because it is softer and more ductile than the martensite.

The initiation of voids at the martensite-ferrite interface was investigated using the energy dispersive X-ray analyzer. High sulfur content was found in the void area, indicating that the interface separation was caused by sulfide embrittlement. Therefore, to improve the ductility of dual-phase steels, the sulfur content and its segregation must be strictly controlled.

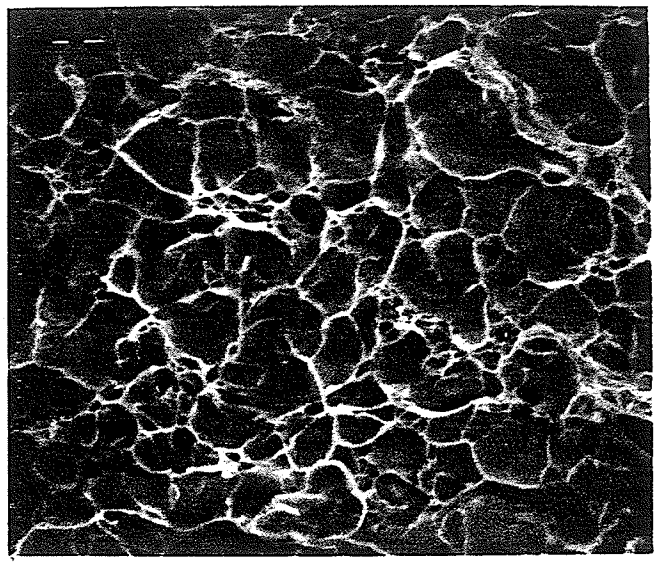

760

4μ

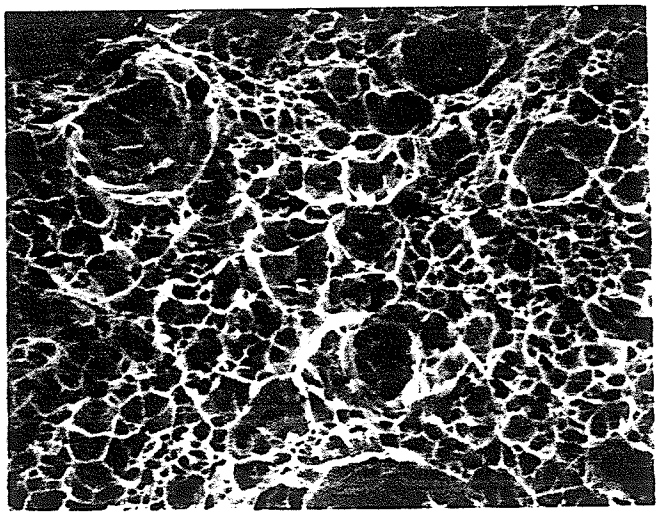

865

Fig. 5-14 Fractographs for specimens with IAT= 760 and 865C.

5.3 DISCUSSION

It has been shown in the previous section that a series of dual-phase steels having a spectrum of strength can be produced simply by intercritically annealing the steels at various temperatures. However, the as-quenched dual-phase steels have a very low yield strength. The strength is acquired after forming operation or cold-working. A question arises, that is, will the steel retain its strength in the cold-worked state under reverse loading? This may have a detrimental effect on the service strength of a cold-formed machine component. In this section we will discuss the microstructural implications of Bauschinger effect in these dual-phase steels.

In general, both isotropic and kinematic hardening occur simultaneously during plastic deformation. From a microscopic point of view, isotropic hardening is mainly due to forest dislocation hardening, that is the formation of attractive junctions as has been discussed in Section 4. The forest hardening is essentially non-directional. Kinematic hardening is due to long range back stress which, in turn, is caused by the plastic incompatibility inside the material. Ashby[88] viewed differently the plastic incompatibility by introducing the concept of geometrically necessary dislocations. Brown and Stobbs[78] have shown that the plastic incompatibility can be represented by the unrelaxed strain which is proportional to the number of Orowan loops around the particles in dispersion hardened alloys. Such calculations can not be readily done in dual-phase

steels which are composed of two coarse ductile phases. We will interpret first the experimental results in terms of the continuum mechanics approach.

The essentials of continuumm mechanics approach to plastic deformation have been reviewed recently by Sowerby, et al..[87] It has been used to explain the cyclic behavior of a two-phase alloy by Asaro.[89] If the work-hardening during uniaxial deformation is entirely due to long-range back stress, i.e., kinematical hardening, this can be described by the translation of the yield surface in the stress space in the direction of applied stress, Fig. (5-15).

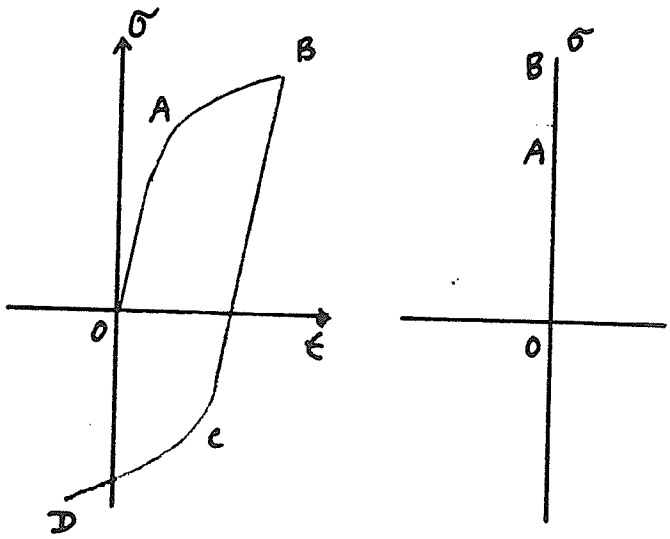

Fig. (5-15) Kinematical σ-ε curve and yield surface

The forward stress-strain curve is described by OAB or $\sigma = f(\varepsilon)$. Upon reverse loading, the stress-strain curve is given by BCD or $\sigma/2 = f(\varepsilon/2)$ using the unloading point B as the origin. Fig. (5-16) shows qualitatively the amount of back stress hardening in the four grades of dual-phase steels. One observes a systematic deviation of the reverse curves from the ideal kinematical hardening curves

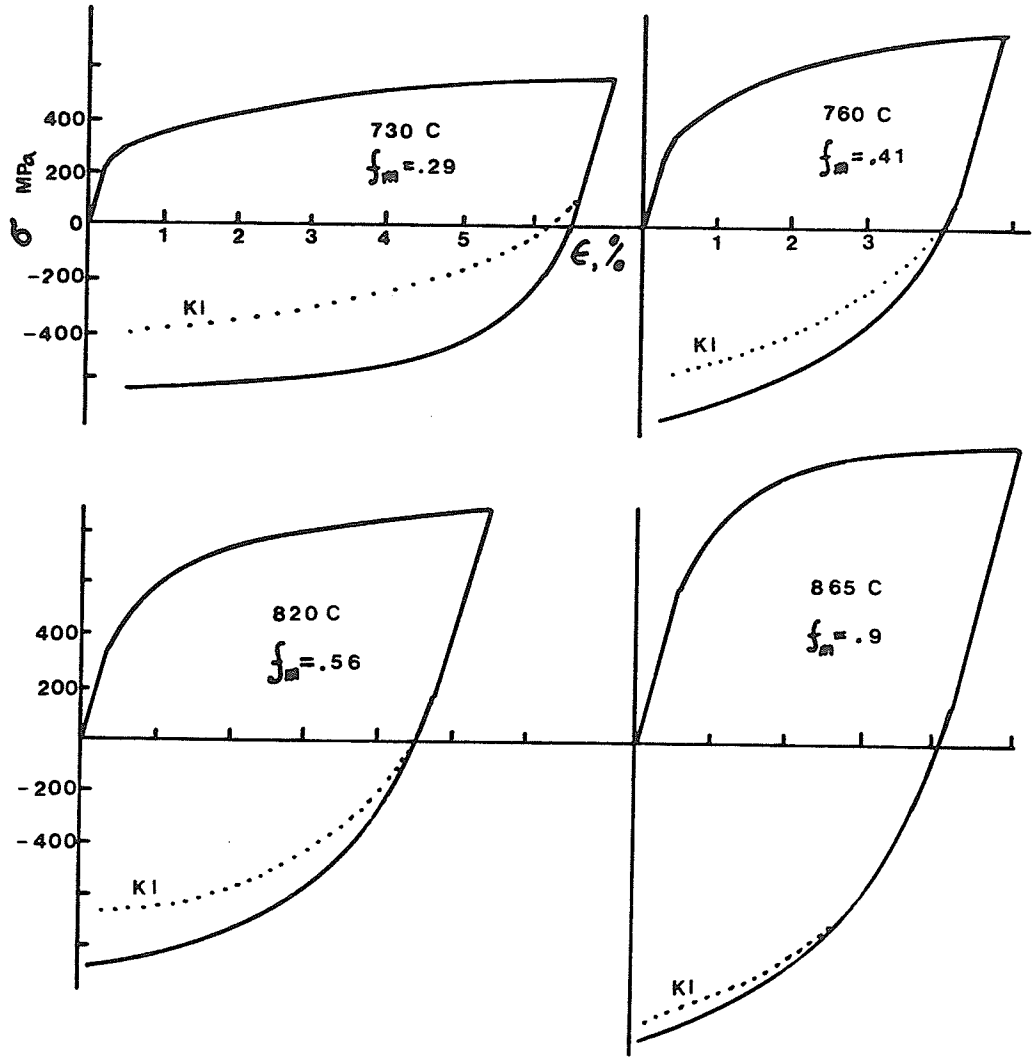

Fig. 5-16 Stress-strain curves and ideal kinematical hardening curves (KI).

with different IAT's. At high IAT where the microstructure almost entirely consists of low carbon martensite (see Fig. (5-2)), the reverse curve follows closely the kinematic one. As the volume fraction of martensite decreases, i.e., at lower IAT, the reverse curve deviates more from the kinematic one, indicating more contribution from the isotropic or forest hardening.

It has been mentioned earlier that the linear relationship between yield stress and volume fraction of martensite (Fig. (5-7)) does not indicate the applicability of the rule of mixtures. This is primarily due to the fact that the strength of martensite and ferrite varies with annealing temperature for dual-phase steels produced by varying IAT using the same starting material. At the lowest IAT (730° C), the high carbon martensite occurs in more or less equiaxed islands. Tseng and Tangri[90] have shown that the low aspect ratio does not allow efficient load transfer to the harder second phase. Therefore, the strengthening mechanism due to the martensite islands is essentially similar to that of particle hardening.[78] As the annealing temperature increases, the volume fraction of martensite also increases, but its strength decreases. For $f_m > 0.4$, the martensite phase nucleated on the ferrite grain boundaries is interconnected in the form of a network. The increase in aspect ratio (defined as the ratio of the mean-free-path in the direction of applied stress and that perpendicular to the stress) and the decrease in the yield strength render the martensite phase plastically deformable. The minimum aspect ratio for martensite to deform can be estimated, assuming that martensite phase is in a cylindrical form having length L and radius r with its length aligned with the stress axis. Then $\sigma_m / \sigma_f = 2\pi r \cdot L/2 / \pi r^2 = L/r$, where σ_f and σ_m are yield stresses of ferrite and martensite respectively.

For IAT = 760° C, $\sigma_m / \sigma_f \approx 2.3$ (see Fig (5-12).

$L / r > 2.3$ is apparently satisfied when IAT $\geq$ 760° C.

We will now discuss the origin of the long-range back stress when the isostrain condition is satisfied (IAT 760^{o} C). This condition can be approximated by Masing's model, which has been discussed in detail by Asaro[89] and Sowerby, et al..[87] This model assumes that the specimen is composed of n elastic-plastic but nonhardening elements of different yield strength. The elements are geometrically identical and the yield strength in tension and compression of an individual element is the same. Fig. (5-17) shows the two-element Masing model and the predicted composite stress-strain curve. We assume that the elements 1 and 2 represent ferrite and martensite, respectively. It is easier to work out the cyclic stress-strain curve using Mroz's[87] yield surface construction. The forward stress-strain curve is described by OAB. At point A, the weak element yields at σ_1. Between AB, element 1 deforms plastically while element 2 deforms elastically. AT point B, element 2 yields at σ_2, but the mean stress in the specimen is $(\sigma_1 + \sigma_2) / 2$. The reverse loading curve BCD is similar to OAB with a scaling factor of 2. The volume fraction of each phase can be incorporated into the Masing model by changing the relative cross-sectional areas of the elements, Fig. (5-17a). It can be shown that the Bauschinger stress, i.e., the stress difference between B and C' in Fig.(5-17c) is given by

$$\Delta\sigma = 2 f_m (\sigma_m - \sigma_f) \qquad (5\text{-}3)$$

That is, the Bauschinger stress predicted by Masing model is proportional to the volume fraction of the stronger phase and the difference in strength between the two phases. Direct comparison of equation (5-3) with present data is not possible because $(\sigma_m - \sigma_f)$

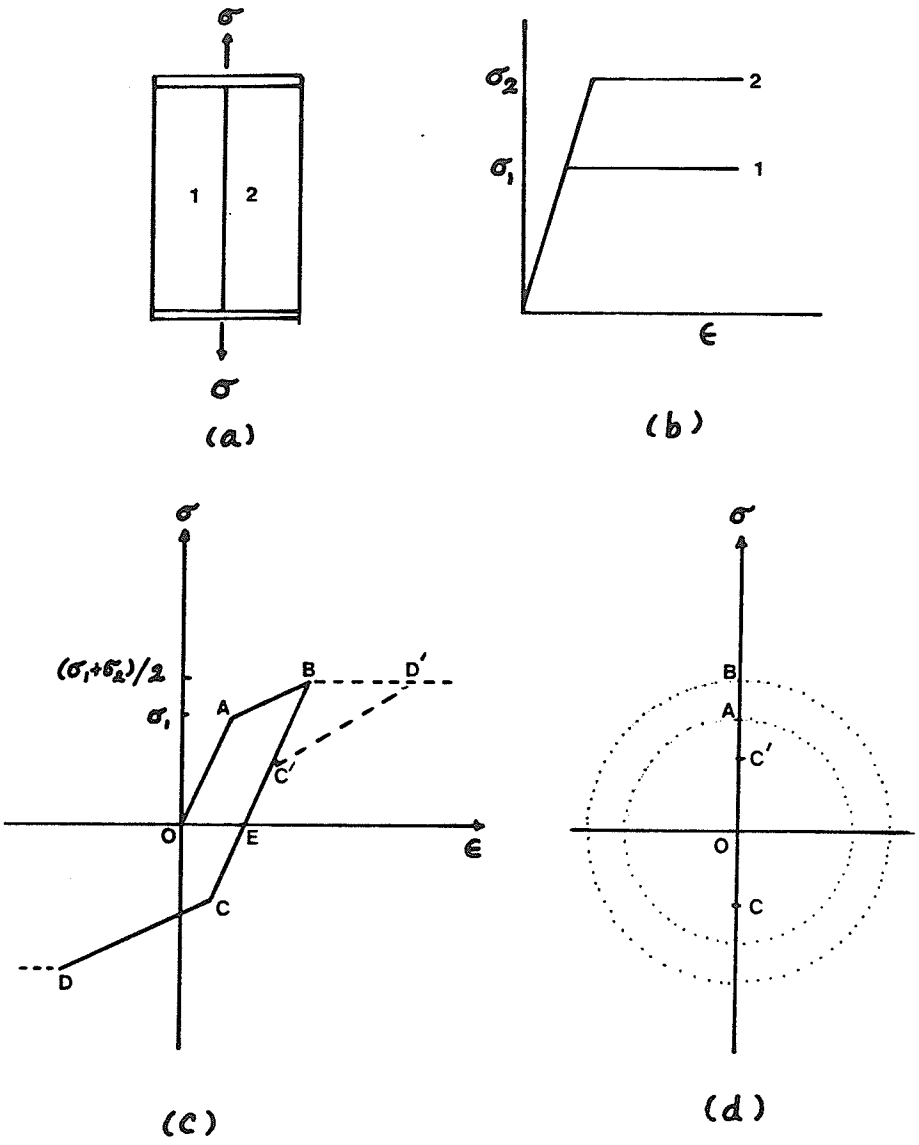

Fig. 5-17 Two-element Masing model.

decreases as f_m increases as shown in Fig. (5-12). However, Fig. (5-10) shows significant increase in $\Delta\sigma$ with increasing f_m. This suggests that Masing's model may underestimate $\Delta\sigma$. The physical basis for the occurrence of Bauschinger effect in the Masing model is the incompatibility due to the difference in yield strength. It is also interesting to note that, for two ductile phases, the permanent softening would not be exhibited when the two phases are deforming plastically. This is borne out by our experiment.

In dual-phase steels, the shear moduli are approximately equal in both phases. Therefore, the image force near the interphase boundaries can be neglected. It is of interest to calculate the number of dislocations, n_p, in a pile-up group which can be sustained at the interphase boundary. A pile-up group produces a stress concentration $n_p\sigma_f$. When the martensite yields, we have

$$n_p\sigma_f = \sigma_m, \quad or \quad n_p = \sigma_m/\sigma_f \tag{5-4}$$

That is, the number of dislocations in a pile-up is equal to the yield stress ratio of the two phases. For the present dual-phase steels, n_p is about 2 to 3. Such a small pile-up group would not be easily recognized in the micrographs. However, the long range back stress would also depend on the number of pile-up groups which is a function of strain. Therefore, the strength and ductility of martensite and the strength of ferrite-martensite interphase boundary determine, to a large extent, the overall mechanical behavior of a dual-phase steel.

5.4 SUMMARY AND CONCLUSIONS

1. It has been shown that iron-carbon alloy of a given composition can be used to produce a series of dual-phase steels with strength and ductility varying with martensite content. The partitioning of alloying elements during intercritical anneal results in a relatively clean ferrite and strong martensite. Several characteristic properties of ferrite-martensite mixtures are observed. They are : (1) relatively lower yield strength,(2) smooth yielding without Luder's band propagation, (3) increased ductility, (4) increased ultimate stress, and (5) strong Bauschinger effect.

2. For martensite volume fraction less than 0.3, the microstructure consists of isolated islands of high carbon martensite in a ferrite matrix. The hardening is due to forest hardening and the Orowan hardening caused by the strong martensite islands.

3. When martensite volume fraction exceeds 0.3 the martensite phase forms a nearly continuous or contiguous structure. It has been found that isostrain condition is vaid in such structures. They exhibit strong Bauschinger effect. The initial work-hardening is essentially due to back stress created by the incompatibility of the two phases. The Bauschinger stress may be estimated by Masing's model,

$$\Delta\sigma = 2 f_m (\sigma_m - \sigma_f)$$

where f_m is the volume fraction of martensite and σ_m and σ_f are

stresses in the martensite and ferrite respectively.

4. For applications which deserve stable strength under reversed loading condition, the martensite volume fraction should be less than 0.3, or the steel should be stabilized under cyclic loading condition.

5. The separation at the interphase boundaries is initiated by sulfide imbrittlement. Therefore, to improve the ductility of dual-phase steels, the sulfur content must be strictly controlled.

REFERENCES

1. J. Friedel, Dislocations, Addison-Wesley, Reading, 1964, p. 121.
2. Work-Hardening, ed. J.P. Hirth and J. Weertman, Gordon and Breach, New York, 1968, see for example page 65.
3. G. Saada, Acta Met. 8, 841, 1960
4. W. Carrington, K. E. Hale, and D. McLean, Proc. R. Soc. A, 259,203, 1960.
5. J. D. Baird and B. Gale, Phil. Trans. R. Soc. A, 257, 553, 1965
6. A. Seeger, Phil. Mag. 46, 1194, 1955.
7. Z. S. Basinski, Phil. Mag. 4, 393, 1959.
8. O. D. Sherby and P. M. Burke, Prog. Mater. Sci. 13, 325, 1968.
9. J. Cadek, M. Pahutova, K. Ciha, and T. Hotinsky, Acta Met. 17, 803, 1969.
10. J.P. Immarigeon and J.J. Jonas, Acta Met. 22, 1235, 1974.
11. D. H. Sastry and K. Tangri, Phil. Mag. 32, 513, 1975
12. D. H. Sastry, C. V. Shastry, and K. Tangri, Phil. Mag. 35, 1099, 1977.
13. D. Tseng, D. J. Lloyd, and K. Tangri, phys. stat. sol. 31(a), 685, 1975
14. J. P. Hirth and J. Lothe, Theory of Dislocations, McGraw-Hill, New York, 1968, p. 762.
15. C. N. Reid, Acta Met. 14, 13, 1966, and 15, 1899, 1967.
16. G. I. Taylor and C. F. Elam, Proc. Roy. Soc. A112, 337, 1926.
17. J. W. Christian, 2nd ICSMA, p. 31, 1970
18. R. A. Foxall and C. D. Statham, Acta Met. 18, 1147, 1970.

19. J. B. Cohen, R. Hinton, K. Lay, and S. Sass, Acta Met. 10, 894, 1962.

20. V. Vitek, Phil. Mag. 18, 773, 1968.

21. M. S. Duesbery and P. B. Hirsch, Dislocation Dynamics, ed. A. R. Rosenfield et al., McGraw-Hill, New York, 1968, p. 57.

22. M. Born and K. Huang, Dynamical Theory of Crystal Lattice, Clarendon Press, Oxford 1954, p. 140.

23. V. Vitek, Crystal Lattice Defects, 5, 1, 1974.

24. Z. S. Basinski, M. S. Duesbery and R. Taylor, Phil. Mag. 21, 1201, 1970.

25. D. F. Stein and J. R. Low, Acta Met. 14, 1183, 1966.

26. T. L. Altschuler and J. W. Christian, Phil. Trans. Roy. Soc. 261, 253, 1967.

27. K. V. Ravi and R. Gibala, Acta Met. 18, 623, 1970.

28. R. L. Fleischer, J. Appl. Phys. 33, 3504, 1962.

29. W. A. Spitzig, Acta Met. 18, 1275, 1970.

30. R. L. Fleischer, Acta Met. 15,1513, 1967.

31. R. Peierls, Proc. Phys. Soc. 52, 256, 1947.

32. F. R. N. Nabarro, Proc. Phys. Soc. 59, 256, 1947.

33. P. B. Hirsch, 5th Int. Congress of Crystallography, Cambridge, p. 140, 1967.

34. R. A. Foxall, M. S. Duesbery and P. B. Hirsch, Can. J. Phys. 45, 607, 1967.

35. Duesbery, Phil. Mag. 19, 501, 1969.

36. W.C. Leslie, Met. Trans. 3, 5, 1972.

37. D. J. Quesnel, A. Sato and M. Meshii, Mat. Sci. Eng. 18, 199, 1975.

38. B. W. Christ, R. P. Gamble and G. V. Smith, Scripta Met. 3, 521, 1969.

39. K. V. Ravi and R. Gibala, Acta Met. 18, 623, 1970.

40. A. Sato and M. Meshii, Acta Met. 21, 753, 1973.

41. C. Wuthrich and W. Frank, Defects in Refractory Metals, Eds., R. De Batis, J. Nichoul and L. Stals, S.C.K. / C.E.N. Mol/Belgium, P. 193, 1972.

42. O. D. Sherby and P. M. Burke, Prog. in Mat. Sci. 13, 325, 1967.

43. O. D. Sherby and A. K. Miller, ASME J. of Mat. and Tech. 1979.

44. A. K.Mukherjee, J. E. Bird and J. E. Dorn, ASM Trans. Quart. 62, 155, 1969.

45. J. P. Poirier, Acta Met. 26, 629, 1978.

46. O. D. Sherby and J. Weertman, Acta Met. 27, 387, 1979.

47. J. Weertman, Rate Processes in Plastic Deformation of Materials, ed. J. C. M. Li and A. A. Mukherjee, ASM, 1975, p. 315.

48. A. H. Cottrell and V. Aytekin, J. Inst. Metals,77, 1247, 1960.

49. W. D. Nix and C. R. Barrett, ASM Trans. Quarterly, 61, 695, 1968.

50. P. Guyot and J. Dorn, Canadian J. of Phys. 45, 983, 1967.

51. T. Surek, M. J. Luton and J. J. Jonas, Phil. Mag. 27, 425, 1973

52. T. Surek, L. G. Kuon, M. J. Luton and J. J. Jonas, Rate Processes in Plastic Deformation of Material, eds. J. C. M. Li and A. K. Mukherjee, ASM, p. 629, 1975.

53. F. A. Smidt, jr., Acta Met. 17, 381, 1969.

54. W. A. Spitzig and A. S. Keh, Acta Meta. 18, 1021, 1970.

55. Z. S. Basinski and J. W. Christian, Austral. J. Phys. 13, 299, 1960

56. J. E. Dorn and S. Rajnak, Trans. MS AIME 230, 1052, 1964.

57. D. M. Barnett and W. D. Nix, Acta Met. 21, 1157, 1973

58. R. M. Douthwaite and J. T. Evans, Scripta Met. 7, 1019, 1973.

59. C. W. Marschall, J. D. Myers, and G. W. P. Rengstorff, Metals Engineering Quarterly, 14, No. 1, 19, 1974.

60. D. F. Stein, J. R. Low, Jr., and A. U. Seybolt, Acta Met. 11, 1253, 1963.

61. P. Guyot and J. E. Dorn, Can. J. Phys. 45, 983, 1967.

62. A. W. Cochardt, G. Schoeck, and H. Wiendersick, Acta Met. 3, 533, 1955.

63. J. R. Spingarn, D. M. Barnett, and W. D. Nix, Acta Met. 27, 1549, 1979.

64. R. J. Arsenault, Acta Met. 15, 501, 1967.

65. S. L. Robinson and P. D. Sherby, Acta Met. 17, 109, 1969.

66. D. F. Stein and J. R. Low, J. Appl. Phys. 31, 362, 1960.

67. R. W. Guard, Acta Met. 9, 1963, 1961.

68. T. Hasegana, S. Karashima, Y. Ikeuchi, Acta Met. 21, 887, 1973.

69. Y. Ishida, C. Y. Cheng and J. E. Dorn, Trans. AIME, 236, 964, 1966.

70. J Diehl, M. Schreiner, S. Staiger and S. Zwiesele, Scripta Met. 10, 949, 1976.

71. J. Weertman, TRans. ASM 61, 681, 1968.

72. J. Weertman, J. Appl. Phys. 26, 1213, 1955 and 28, 362, 1957.

73. D. McLean, Trans. AIME 242, 1193, 1968.

74. F. Garofalo, L. Zwell, A. S. Keh and S. Weissman, Acta Met. 9, 721, 1961.

75. Same as Ref.1, p. 239

76. H. E. Evans and G. Knowles, Acta Met. 35, 963, 1977.

77. D. J. Denver, J. Appl. Phys. 43, 3293, 1972.

78. L. M. Brown and W. M. Stobbs, Phil. Mag. 23, 1185, 1971.

79. H. Fischmeister and B. Karlsson, Z. Metallkde., 68, 311, 1977.

80. R. G. Davies, Metall. Trans. 9A), 671, 1978.

81. F. S. LePera, J. Metals, 32(3), 38, 1980.

82. M. S. Rashid, Formable HSLA and Dual-Phase Steels, Proceedings of AIME Symposium, 1977, ed. A. T. Davenport, p. 1.

83. D. V. Wilson, Acta Met. 13, 807, 1965.

84. J. D. Atkinson, L. M. Brown and W. M. Stobbs, Phil. Mag. 30, 1247, 1974.

85. Y. Salek and H. Margolin, Acta Met. 27, 535, 1979.

86. E. Orowan, Internal Stresses and Fatigue in Metals, G. M. Rassweiler and W. L. Grube, Elsevier, New York, 1959.

87. R. Sowerby, D. K. Uko, and Y. Tomita, Mat. Sci. Eng. 41, 43, 1979.

88. M. F. Ashby, Phil. Mag. 21, 399, 1970.

89. R. J. Asaro, Acta Met. 23, 1255, 1975.

90. D. Tseng and K. Tangri, to be published in Met. Trans. 1982.

91. G. Masing, Lehrbuck der Allgemeinen Metallkunde, Springer Verlag, Berlin, 1950, p. 405.

92. D. Tseng and K. Tangri, Scripta Met. 11, 719, 1977.

93. D. A. Korzekwa, R.D. Lawson, D. K. Matlock and G. Krauss, Scripta Met. 14, 1023, 1980.

94. A. Seeger and C. Wuthrich, Nuovo Cimento 33, 38, 1976.

95. C. Wuthrich, Phil. Mag. 35, 325 and 337, 1977.

96. J. P. Hirth, Scripta Met. 16, 221, 1982.

97. T. S. Ke, Scripta Met. 16, 225, 91982.

98. G. Schoeck, Scripta Met. 16, 223, 1982.

99. A. Seeger, Scripta Met. 16, 241, 1982.

100. I. G. Ritchie, Scripta Met. 16, 249, 1982.

101. L. P. Kubin and F. Louchet, Acta Met. 27, 337, 1979.

102. L. P. Kubin, F. Louchet, J. P. Peyrade, P. Groh and J. P. Cottu, Acta Met. 27, 343, 1979.

103. A. Sato and M. Meshii, Scripta Met. 8, 851, 1974.

104. C. R. Barrett and W. D. Nix, Acta Met. 13, 1247, 1965.

105. G. B. Gibbs, Phil. Mag. 23, 771, 1971.

106. F. R. N. Nabarro, Phil. Mag. 16, 231, 1967.

107. J.H. Gittus, Acta Met. 22, 789, 1974.

108. R. Lagneborg, Metal Sci. J. 6, 127, 1972.

109. Z. S. Basinski, M. S. Duesbery and R. Taylor, Can. J. Phys. 49, 2160, 1971.

110. Z. S. Basinski, M. S. Duesbery and G. S. Murty, Acta Met. 29, 801, 1981.

111. H. Matsui, A. Kimura and H. Kimura, 5th ICSMA, p. 977, 1979.

112. E. Pink and R. Arsenault, Prog. Met. Sci. 24, 1, 1979.

113. M. S. Duesbery and R. A. Foxall, Phil. Mag. 20, 719, 1969.

114. C. J. Bolton and G. Taylor, Phil. Mag. 26, 1359, 1972.

115. R. G. Garlick and H. B. Probst, Trans. AIME, 230, 1120, 1964.

116. J. Richter and D. Schulze, Phys. Stat. Sol. 26, 485, 1968.

117. D. Tseng and F. H. Vitovec, Fundamental of Dual-Phase Steeels, AIME, page 399, 1981.

118. R. J. Borg and C. E. Birchenall Trans. AIME, 218, 980, 1960.

APPENDIX

(1) Results of Differential-Temperature Tests

(A) Ferrovac E Iron (Strain rate = 0.0025 $min.^{-1}$)

T(°K)	$\frac{\Delta\sigma^*}{\Delta T}$ $(\frac{Kg}{mm^2 \cdot deg})$	T(°K)	$\frac{\Delta\sigma^*}{\Delta T}$ $(\frac{Kg}{mm^2 \cdot deg})$
sp. no. 12		sp. no. 15	
270.1	0.079	17.8	0.624
251.9	0.114	12.4	0.921
240.5	0.143		
227.2	0.208	sp. no. 16	
210.6	0.210		
197.0	0.261	12.5	0.998
182.0	0.275		
173.7	0.276		
154.5	0.304	sp. no. 17	
144.3	0.333		
133.9	0.371	95.0	0.283
113.3	0.437	85.0	0.403
sp. no. 14		sp. no. 19	
44.5	0.688	95.0	0.436
34.5	0.673	85.0	0.480
27.5	0.724	70.0	0.356
22.5	0.788	56.5	0.563
17.5	0.844	47.9	0.579
		36.5	0.626
		25.0	0.851

T (°K)	$\frac{\Delta\sigma^*}{\Delta T}$ $\left(\frac{Kg}{mm^2 \cdot deg}\right)$
sp. no. 25	
286.2	0.062
269.8	0.053
257.9	0.085
244.0	0.094
228.0	0.153
215.7	0.169
202.7	0.191
185.8	0.189
174.0	0.382
162.7	0.302
148.5	0.297
135.2	0.313
122.0	0.404
105.7	0.390
88.4	0.449
sp. no. 20	
63.4	0.422
42.5	0.601
27.5	0.581
15.0	0.812

linear regression between 77 and 300 K gives

$$-\frac{\Delta\tau^*}{\Delta T} = -2AT + B, \quad 2\tau^* = \sigma^*$$

$A = 1.05 \times 10^{-3}$ Kg/mm^2 . deg^2)

$B = 0.631$ Kg/mm^2 . deg)

(B) Battelle Iron

T (°K)	$\frac{\Delta\tau^*}{\Delta T}$ $\frac{Kg}{mm^2 \cdot deg}$	T (°K)	$\frac{\Delta\tau^*}{\Delta T}$ $\frac{Kg}{mm^2 \cdot deg}$
sp. no. 1		sp. no. 2	
288.1	0.028	287.9	0.017
272.2	0.050	269.3	0.044
257.9	0.064	250.7	0.073
244.2	0.086	224.9	0.095
228.3	0.093	193.5	0.078
211.4	0.083	164.7	0.095
197.5	0.094	138.8	0.110
183.4	0.085	121.2	0.120
168.8	0.126	108.0	0.154
156.0	0.115	96.9	0.131
143.7	0.114		
130.0	0.134		

(2) Activation Volumes

(A) Ferrovac E Iron

τ^* Kg/mm^2	V_a^* b^3
1.0	64.2
2.8	34.2
4.8	26.1
7.2	20.4
9.7	19.2
12.7	17.9
16.3	16.1
26.1	13.3
31.3	7.23
36.3	6.95
39.5	5.50

(B) Battelle Iron

sp. no. 4

0	78.2
0.30	42.9
2.45	36.9
5.68	50.4
7.92	35.8
10.65	31.7
13.18	26.1
14.66	23.0

sp. no. 5

0.47	57.6
2.09	34.8
4.95	38.6
8.79	33.5
13.22	28.3

(3) Axial yield stress of Ferrovac E (Kg/mm^2)

$\dot{\varepsilon}$ sec^{-1} \ T °C	400	500	600	700	770	800
4.17×10^{-5}	4.9	3.8	2.4	1.8	1.3	1.0
8.33×10^{-5}	5.6	3.9	2.4	2.0	1.3	1.2
4.17×10^{-4}	6.9	5.1	3.1	2.0	1.6	1.4
8.33×10^{-4}	6.5	5.4	3.2	2.1	1.5	1.4
4.17×10^{-3}	6.6	6.3	4.6	2.2	1.7	1.5

(4) Steady-state flow stress of Ferrovac E (Kg/mm^2)

$\dot{\varepsilon}$ sec^{-1} \ T °C	400	500	550	600	650	700	735	770	800
4.17×10^{-5}			6.66		3.08		2.24	1.46	
8.33×10^{-5}		7.37	6.85	5.26	4.60	2.89	2.42		1.47
1.67×10^{-4}						3.21			
4.17×10^{-4}	15.27	8.54	7.95	6.32	3.90	3.58	2.93	2.09	1.85
8.33×10^{-4}	15.17	9.39	8.42	7.04	5.09	3.91	3.39	1.86	1.86
4.17×10^{-3}	19.54	11.47	10.17	8.67	5.99	4.59	4.17	2.62	2.39

(5) Activation enthalpy in region I.

(A) Ferrovac E Iron

τ^* Kg/mm^2	ΔH eV
1.0	0.66
2.8	0.55
4.8	0.50
7.2	0.43
9.7	0.42
12.7	0.39
16.3	0.35

(B) Battelle Iron

2.5	0.85
5.7	0.53
7.9	0.47
10.7	0.42
13.2	0.35
14.7	0.30

(6) Average Volume Fraction and Mean-Free-Path of Ferrite

Annealing temp. (^{o}C)	Mean-free-path(μm)	Vol. fraction
730	4.8	0.29
760	4.4	0.41
820	2.6	0.56
865	1.5	0.90

(7) Average Bauschinger Strain

T	ϵ_{ABS} (%)	ϵ_{F} (%)
730	0.53	3.6
	0.74	7.1
	0.76	10.3
760	0.81	4.2
	0.83	2.7
	0.35	1.2
	1.48	13.9
	1.13	4.9
	1.25	8.2
	1.33	10.0
	0.96	4.9
820	1.06	7.3
	1.03	5.5
	1.39	12.7
	1.10	8.2
	0.37	1.3
	1.30	8.9
	0.67	3.0
865	0.88	5.2
	0.45	1.6
	1.00	7.9